AD-A185 959 TECHNICAL REPORT FOR THE PERIOD 1 APRIL-30 JUN 1987(U) 1/2
SCIENCE APPLICATIONS INTERNATIONAL CORP ARLINGTON VA
CENTER F.. R BAUMSTARK ET AL. AUG 87 SAIC-87/1131
UNCLASSIFIED MDA903-84-C-0021 F/G 8/11 NL

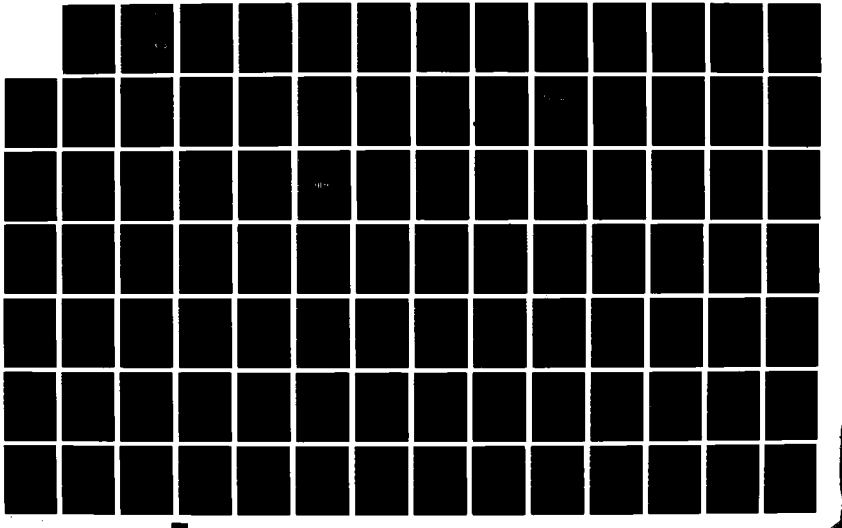

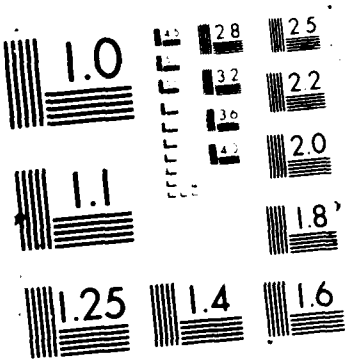
1.0
1.1
1.25
1.4
1.6
1.8
2.0
2.2
2.5
2.8
3.2
3.6

Technical Report C87-03
August 1987

TECHNICAL REPORT FOR THE PERIOD 1 APRIL - 30 JUNE 1987

Center Staff

SPONSORED BY:
DEFENSE ADVANCED RESEARCH PROJECTS AGENCY

Technical Report C87-03
August 1987

TECHNICAL REPORT FOR THE PERIOD 1 APRIL - 30 JUNE 1987

Center Staff

Sponsored by:
DEFENSE ADVANCED RESEARCH PROJECTS AGENCY
Monitored by:
Defense Supply Service - Washington
Under Contract No. MDA 903-84-C-0020

Science Applications International Corp.
1735 Jefferson Davis Highway, Suite 907
Arlington, VA 22202

UNCLASSIFIED
SECURITY CLASSIFICATION OF THIS PAGE

REPORT DOCUMENTATION PAGE

Form Approved
OMB No. 0704-0188
Exp. Date: Jun 30, 1986

1a REPORT SECURITY CLASSIFICATION Unclassified	1b RESTRICTIVE MARKINGS
2a SECURITY CLASSIFICATION AUTHORITY	3 DISTRIBUTION/AVAILABILITY OF REPORT Unlimited
2b DECLASSIFICATION/DOWNGRADING SCHEDULE	
4 PERFORMING ORGANIZATION REPORT NUMBER(S) SAIC-87/1131 Technical Report C87-03	5 MONITORING ORGANIZATION REPORT NUMBER(S)
6a NAME OF PERFORMING ORGANIZATION Science Applications International Corporation 6b OFFICE SYMBOL (If applicable)	7a NAME OF MONITORING ORGANIZATION Defense Supply Service - Washington
6c ADDRESS (City, State, and ZIP Code) Center for Seismic Studies/SAIC 1300 N. 17th Street, Suite 1450 Arlington, Virginia 22209-3871	7b ADDRESS (City, State, and ZIP Code) Room 1D245, The Pentagon Washington, D.C. 20310
8a NAME OF FUNDING/SPONSORING ORGANIZATION Defense Advanced Research Projects Agency 8b OFFICE SYMBOL (If applicable) STO/GSD	9 PROCUREMENT INSTRUMENT IDENTIFICATION NUMBER 903 MDA-84-C-0020
8c ADDRESS (City, State, and ZIP Code) 1400 Wilson Boulevard Arlington, Virginia 22209	10 SOURCE OF FUNDING NUMBERS PROGRAM ELEMENT NO: PROJECT NO.: A04882 TASK NO: WORK UNIT ACCESSION NO:

11 TITLE (Include Security Classification)

Technical Report for the Period 1 April - 30 June 1987 (Unclassified)

12 PERSONAL AUTHOR(S) R. Baumstark, A. Campanella, P. Dysart, H. Israelsson, A. Jurkevics, J. Pulli, A. Ryall

13a TYPE OF REPORT	13b TIME COVERED	14 DATE OF REPORT (Year, Month, Day)	15 PAGE COUNT
Technical Report	FROM 4-1 TO 6-30-87	1987 August	97

16 SUPPLEMENTARY NOTATION

17 COSATI CODES		
FIELD	GROUP	SUB-GROUP

18 SUBJECT TERMS (Continue on reverse if necessary and identify by block number)

Seismology, Attenuation, m_b bias, Nuclear Monitoring, GSE, Azimuth, Seismic Networks, Regional Propagation, NRDC

19 ABSTRACT (Continue on reverse if necessary and identify by block number)

This report summarizes work during 1 April - 30 June 1987, on topics described in the Center R&D Plan of October 1985, and subsequent guidance from DARPA. In research related to network capability and design, Section 2 contains two technical notes. One compares mean values of short-period seismic noise measured during the GSE Technical Test with published values of Ringdal (1977, 1986), for stable and tectonically active regions. A second compares depth determinations during the 1980 Common Data Base Experiment with theoretical detection thresholds. The third considers the significance of local and regional data in a global monitoring system.

(Continued on attached sheet)

20 DISTRIBUTION/AVAILABILITY OF ABSTRACT	21 ABSTRACT SECURITY CLASSIFICATION
☒ UNCLASSIFIED/UNLIMITED ☐ SAME AS RPT ☐ DTIC USERS	Unclassified
22a NAME OF RESPONSIBLE INDIVIDUAL Ann U. Kerr	22b TELEPHONE (Include Area Code) (202) 697-7523 22c OFFICE SYMBOL STO/GSD

DD FORM 1473, 84 MAR 83 APR edition may be used until exhausted
All other editions are obsolete

SECURITY CLASSIFICATION OF THIS PAGE
UNCLASSIFIED

19. Abstract - *(Continued)*

Section 3 includes two reports on research to improve analysis of regional seismic data. One is based on a consideration of particle motion of regional phases, and recommends ways to implement automated or interactive particle-motion analysis of regional seismic waveforms. The other focuses on event characterization of 95 earthquakes, mine blasts and offshore events recorded at NORESS.

Section 4 contains miscellaneous topics. One deals with azimuth determination using polarization parameters of *P* and LR waves. A second discusses reanalysis of m_b bias between a recording site in eastern Kazakh and a station on the granitic stock in which the PILEDRIVER explosion was detonated at the Nevada Test Site. A final note summarizes the status of database administration at the Center, and describes a new database containing waveforms from stations being operated in eastern Kazakh under an agreement between the Soviet Academy of Sciences and the Natural Resources Defense Council.

Table of Contents

1. FOREWORD

Work continued during this reporting period on the topics described in the Center R&D Plan of October 1985, and subsequent guidance from DARPA. In research related to network capability and design, Section 2 contains three technical notes. The first compares mean values of short-period seismic noise measured during the GSE Technical Test with published values for shields, platforms, tectonic regions, and oceanic regions of various ages. The second note compares depth determinations during the 1980 Common Data Base Experiment with theoretical detection thresholds, and concludes that depths could be determined, using a multi-method approach, for almost 90% of events at the 90% detection threshold. The third note illustrates the significance of local and regional data in a global monitoring system, and concludes that a limited number of NORESS-type arrays could be a powerful alternative to auxiliary station networks.

Section 3 includes two reports on research to improve analysis of regional seismic data. One considers the type of information available in analysis of particle motion of regional phases, and the sensitivity of particle-motion parameters to signal-to-noise ratio. The study leads to recommendations for implementation of automated or interactive particle-motion analysis of regional seismic waveforms. A second report covers analysis of 95 small earthquakes, mine blasts, and offshore events recorded at NORESS. Source-receiver distances was less than 1,000 km for most of these events. The study focuses on event characterization, and concludes that a technique involving amplitude ratios and cepstral variance provides moderately good separation of earthquakes and mine explosions.

The first note in Section 4 deals with azimuth determined from the polarization of *P* and LR waves. The results indicate that accurate backazimuth estimates can be obtained from *P*-waves recorded at transparent station sites. The analysis method is simple and can be developed as an interactive analysis tool. Backazimuth estimates from LR waves are more scattered, but appear to be less sensitive to local geologic variations. A second note discusses reanalysis of the m_b bias between a recording site in eastern Kazakh and a station on the granitic stock in which the PILEDRIVER explosion was detonated at the Nevada Test Site. The reanalysis, based on revised magnitudes for the NTS station, leads to a propagation bias of 0.12-0.15 m_b between the two sites. A final note summarizes the status of database administration at the Center, and describes a new database containing waveforms from stations being operated in eastern Kazakh under an agreement between the Soviet Academy of Sciences and the Natural Resources Defense Council.

In other activities, preparations for participating in international seismic data exchange experiments continued throughout this quarter. Two aspects were stressed. The first focused on defining the seismological processes that would be conducted at International Data Centers, and in particular how these centers would use seismic waveform segments to improve the quality of their analyses. The second focused on the mechanics of waveform data exchange, including the definition of new database relations that will be required to handle the data.

The Center has also been heavily involved in updating and extending its database design, in order to handle new types of data -- principally data from seismic arrays. Working jointly with Science Horizons, Inc., and the SAIC seismology group in La Jolla, the Center is preparing a revised database structure, and has begun to work on software modifications that make the data more accessible to users.

2. NETWORK CAPABILITY AND DESIGN

2.1. A NOTE ON NETWORK DESIGN: DETECTION THRESHOLD AND TECTONIC REGION

The detection threshold of seismological stations is determined by several factors including local seismic noise, station installation, equipment and processing, as well as tectonic structure. In this brief note we consider the effect of tectonic structure.

For the tectonic regionalization we use a characterization introduced by Jordan (1980). This regionalization divides the earth's surface into 2592 (36 by 72) segments which are 5 by 5 degrees in latitude and longitude. Each segment is classified into one of six possible tectonic types: young, intermediate, old ocean, orogenic, platform, and shield. The extent of the shield and platform areas are shown in *Figure 1*. In all there are 510 such shield or platform segments, which corresponds to about 20% of the total number of segments.

The following table summarizes mean values of short-period noise amplitudes by tectonic region for three global networks consisting of 60 (GSETT), 115 (Ringdal, 1986), and 500 (Ringdal *et al.*, 1977) stations, respectively.

TABLE I.

Tectonic Region	Ringdal (1977) No	Mean (nm)	SD (log)	Ringdal (1986) No	Mean (nm)	SD (log)	GSETT No	Mean (nm)	SD (log)
Young Ocean	3	69.7	0.25						
Intermediate Ocean	49	46.6	0.40	4	23.7	0.25	3	21.5	0.46
Old Ocean	10	46.6	0.42	2	23.7				
Orogenic	345	32.6	0.39	66	12.7	0.23	37	10.4	0.43
Platform	49	15.0	0.42	19	7.7	0.19	5	9.6	0.29
Shield	45	10.5	0.58	24	10.1	0.23	15	6.6	0.48

The noise amplitudes have been derived from amplitude (Ringdal, 1986) and magnitude (Ringdal *et al.*, 1977) thresholds as well as a combination of amplitude thresholds and noise data (GSETT). The mean values in the table were obtained from the mean of the logarithms of the noise or amplitude threshold. The magnitude thresholds of Ringdal *et al.* (1977) were converted with an amplitude-distance correction corresponding to a mean value in the distance interval 30 to 90 degrees, and assuming a signal-to-noise ratio of 1.5 for detection. It should be noted that the noise values in Table I are largely derived from reported amplitude detection thresholds, and that these values need not necessarily agree with actual measurements of ground noise at the stations. The noise amplitudes in the table represent "operational" values including other factors (e.g., local signal attenuation) but are relevant as indicators of the detection capabilities of the stations.

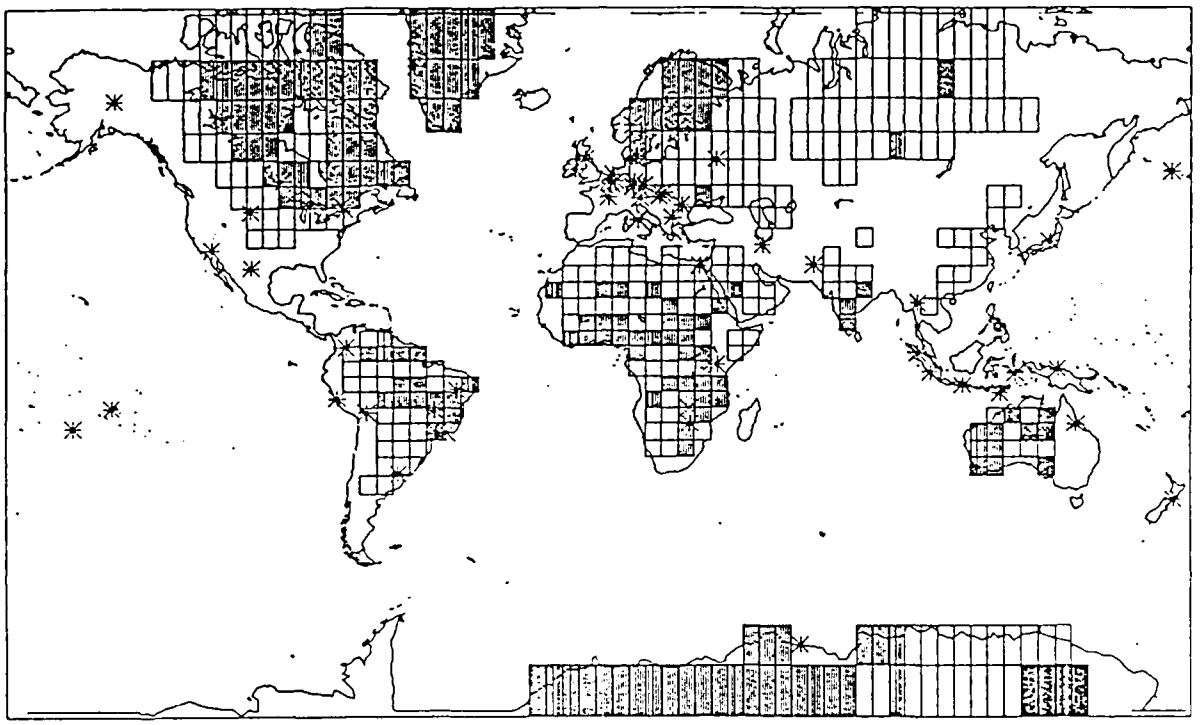

Figure 1. The shield (in black) and platform segments (open rectangles) as defined in the tectonic regionalization by Jordan (1981). The GSETT stations are indicated by asterisks.

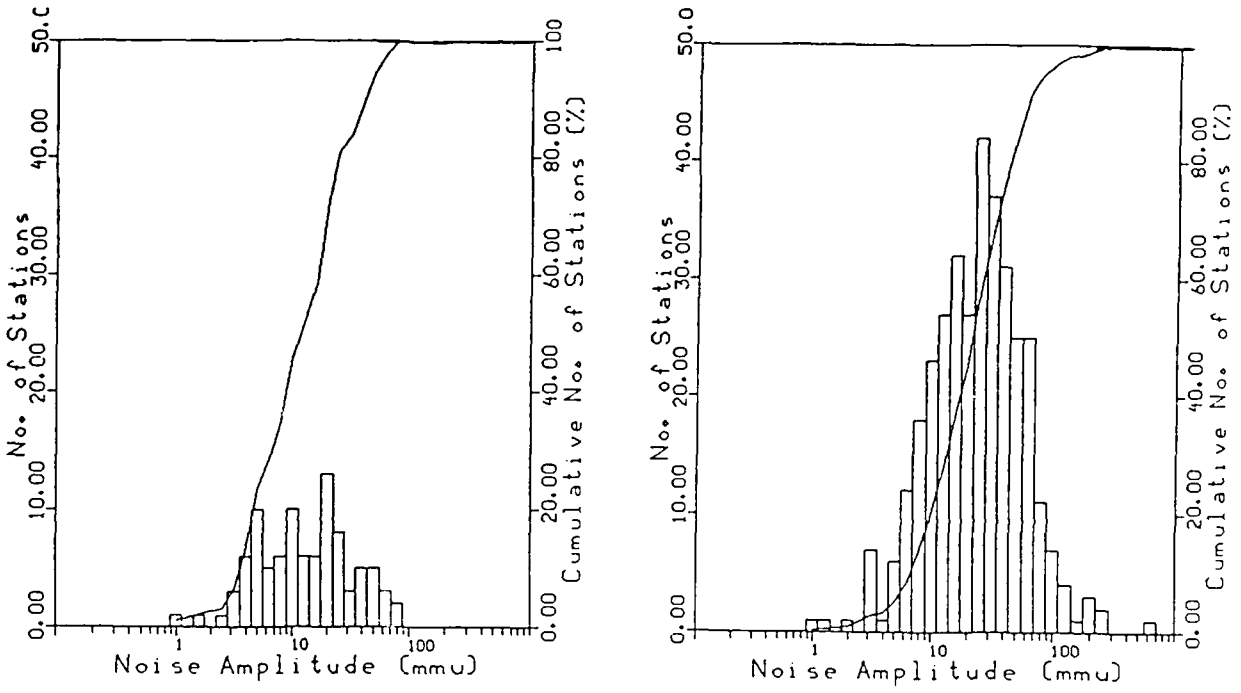

Figure 2. Histograms for short-period noise amplitudes at stations located on shield/platform (left) and orogenic (right) tectonic structures. The super-imposed curves represent the cumulative frequency distribution.

Since the "operational" noise amplitudes have been obtained in somewhat different manners for the three networks, direct comparisons between station averages of regions that belong to *different* studies have to made with some care, whereas comparisons between region averages *within* a study can be made more easily. The mean values are, as expected, consistently lowest for shield and platform stations within each study. There is, however, a considerable scatter in the data. *Figure 2* compares the distributions of noise amplitudes for shield/platform and orogenic stations of the study by Ringdal *et al.* (1977). The networks in Table I have between 10 and 30% of stations on shields, whereas the largest percentage of stations (between 40 and 60) are located in orogenic areas.

In summary, Table I suggests that it is reasonable to assume 10, 15, 25, and 50 nm as typical values for the average station located in shield, platform, orogenic, and oceanic areas, respectively.

Hans Israelsson

REFERENCES

Jordan, T. H., 1981. "Global Tectonic Regionalization for Seismological Data Analysis," *Bull. Seism. Soc. Am.*, 71: 1131-1141.

Ringdal, F., Husebye, E. S., Fyen, J., 1977. "Earthquake Detectability Estimates for 478 Globally Distributed Seismograph Stations," *Phys. Earth. Planet. Interiors*, 15: 24-32.

Ringdal, F., 1986. "Study of Magnitudes, Seismicity, and Earthquake Detectability Using a Global Network," *Bull. Seism. Soc. Am.*, 76: 1641-1659.

2.2. A NOTE ON WAVEFORM PROCESSING: DEPTH ESTIMATES AND DETECTION THRESHOLDS

Regular reporting and analysis of waveform data will be one of the most important new features of the global seismic system being discussed by the Group of Scientific Experts (GSE), U.N. Conference on Disarmament. Although global network waveform data have long been used for depth determination there is comparatively little experience reported in the literature on their use for analysis of small magnitude events (m_b<5.5).

Promising results with analysis of multi-station waveforms were obtained in an early data exchange experiment carried out in 1980 within the framework of the GSE. This experiment, usually referred to as the Common Data Base Experiment (CDBE), resulted in the compilation of digital recordings from some 30 globally distributed stations. The data for the CDBE cover a time period of two weeks. In one of the studies on waveform analysis carried out on this data base, a procedure for depth determination was defined and applied with encouraging results (Roy, 1984).

This procedure involves several waveform processing steps, including identification of depth phases, stacking of multi-station records, and deconvolution.

In this note we compare the applicability of this depth determination procedure with calculated network detection thresholds. The stations of the CDBE network *(Figure 1)* included 59 stations, thirty-one of which provided digital waveform data. The magnitude detection threshold was computed for a network consisting of those stations with digital recordings using the SNAP/D program. Station noise values reported in the literature in detectability studies were used in the calculations, which resulted in an average threshold for the world of about m_b=4.5 (90% probability).

The calculated threshold is compared in *Figure 2* with the percentage of events for which depth could be determined from waveform data. The percentages are shown as a function of magnitude.

Figure 2 shows that the applicability of the depth estimation procedure is quite high. In fact depths could be determined for almost 90% of the events at the calculated 90% m_b- detection threshold.

The applicability of the procedure virtually closes the gap between detection and depth estimation and is high compared with depth estimation based on routinely reported depth phases. For example, about 10% and 22% of the depth determinations by NEIS for events during the GSETT were made on the basis, respectively, of surface reflections and other geophysical evidence (i.e., not first arrival times). It should be noted, however, that the high applicability of depth calculation based on the waveform procedure does not necessarily mean small error estimates.

Hans Israelsson

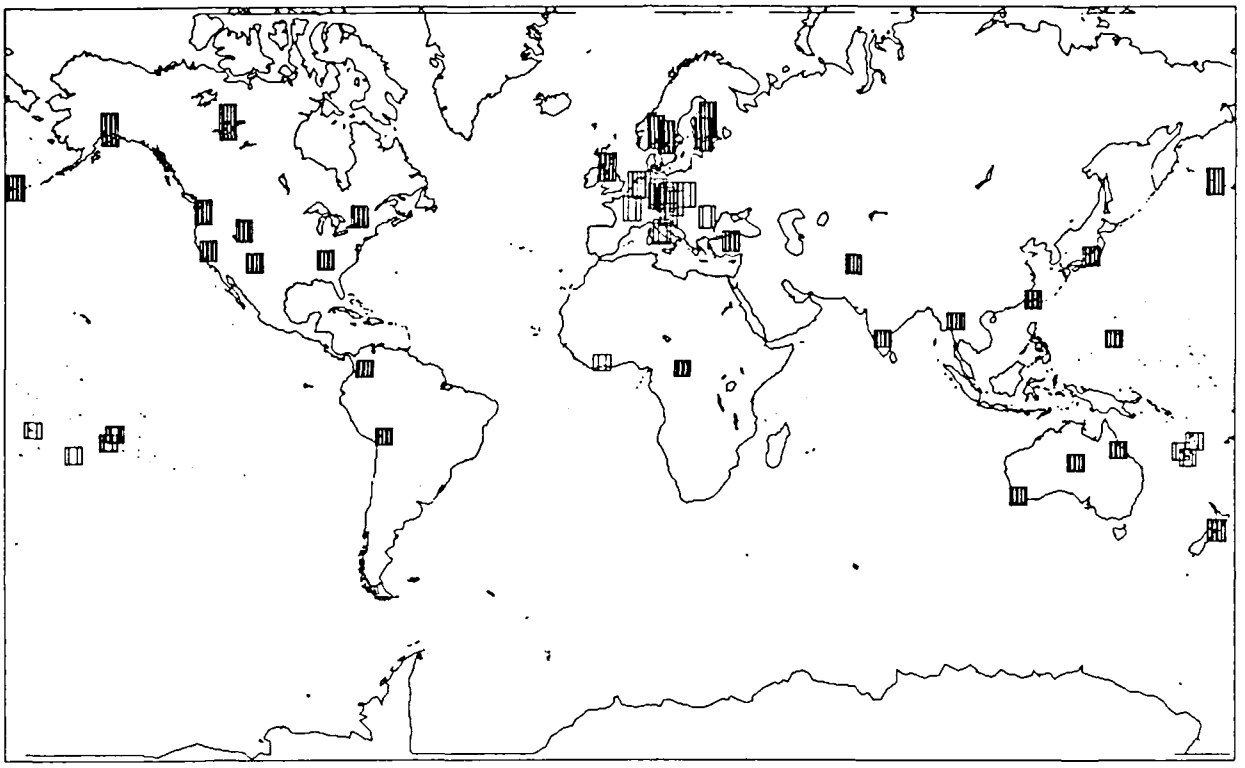

Figure 1. Locations of stations participating in the Common Data Base Experiment (CDBE). Stations contributing with digital data are marked with filled symbols.

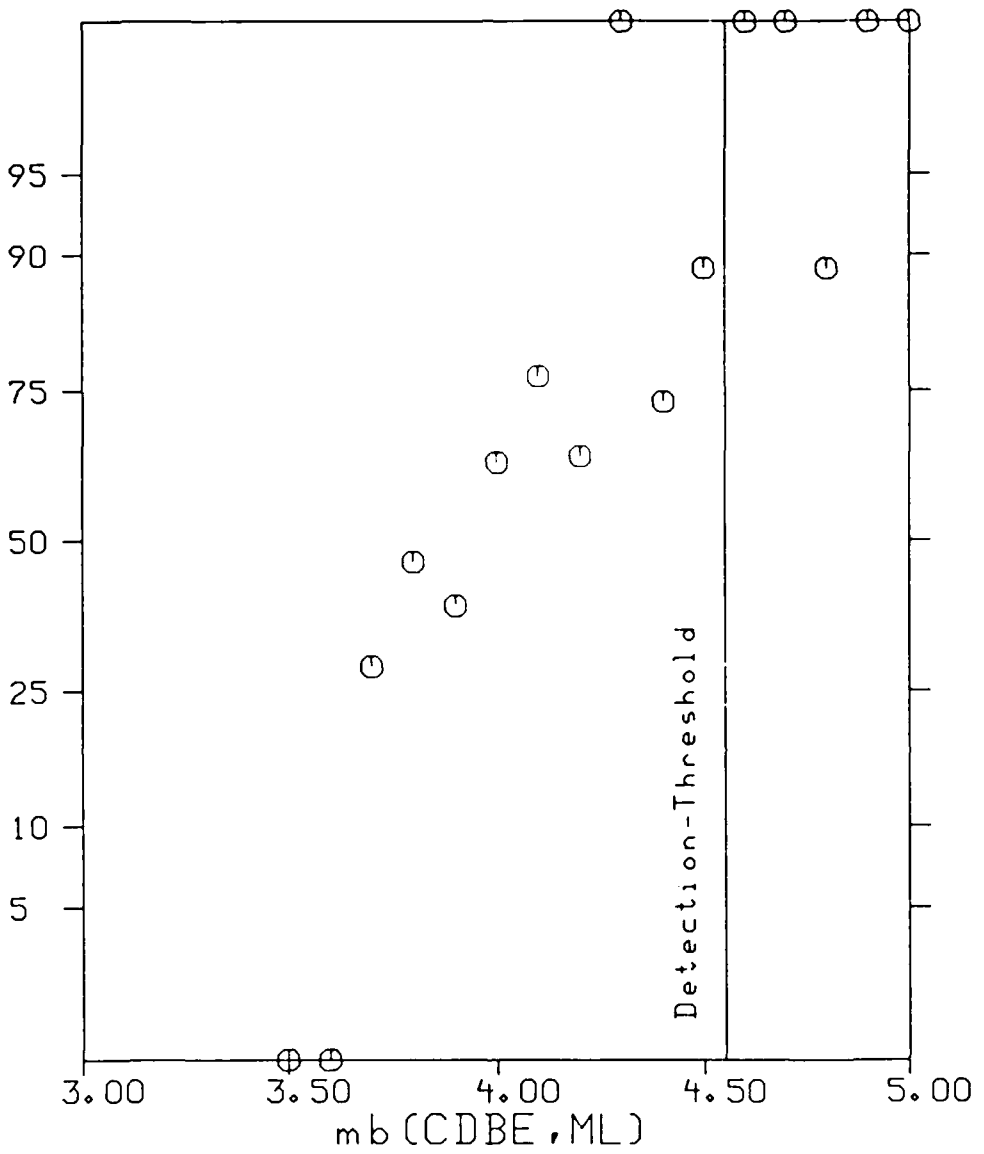

Figure 2. The diagram shows the percentages of CDBE events, for which depth could be determined from analysis of waveform data according to procedure by Roy (1984) as a function of magnitude, m_b (open circles). The vertical scaling is transformed so that data following a normal distribution will be on a straight line. The calculated average 90% m_b detection threshold is included in the diagram for comparison.

REFERENCE

Roy, F., 1984. "Source Depth Estimation Using Multi-Station Waveform Data," *Bull. Seism. Soc. Am.*, 74: 1623-1644.

2.3. A NOTE ON NETWORK DESIGN: REGIONAL DETECTIONS BY A GLOBAL NETWORK

2.3.1. Introduction

Global station networks of the GSE type are primarily based on signal detections in the *teleseismic* distance range. However, there are also a large number of signals detected from local ($\Delta<1.5$ degrees) and regional distances ($1.5<\Delta<25$) reported by such a station network. Detections of events at local and regional distances by "teleseismic"-oriented stations of a global network have so far received little attention, since many of these detections remain unassociated with seismic events located by the network.

It is widely recognized that local and regional phases may significantly improve the performance of global network. In order to draw upon local and regional phases it has been proposed that the GSE global network of some 50 core stations (teleseismic) should be supplemented by so called auxiliary stations (GSE/US/44, 1987). These auxiliary stations do not belong to the group of regularly reporting core stations of the global network and need not fully comply with the standard specifications of such stations. Data from auxiliary stations would be useful in analyzing, for example, local seismicity, mining blasts, and earthquake swarms.

Another suggestion, which is somewhat similar to the auxiliary stations has also been put forward (GSE/Canada, Sweden/1, 1987). Data recorded at so called "second tier" stations, which might be stations of national seismograph networks primarily set up to monitor local seismicity, are supposed to be made available to the global system on an *Ad Hoc* basis.

In this note we illustrate improvements based on the use of local and regional phases with regard to event detection and depth estimation with calculations for some hypothetical station networks.

First, however, we can get some idea of the number of local events that might be reported by stations of a global network of "teleseismic" stations by examining some data from the GSETT in 1984.

2.3.2. Local Detections by GSETT Stations

The number of reported detections per day by the GSETT stations are listed in Table I GSE/SW, 1985). The table gives for each station the *total* number of detections together with the number and percentages of *local* detections (GSE/SW, 1985; local is defined as P_g, P_b, P_n or LA, LB, QB, RB). Although the GSETT stations were supposed to report *all* signals, i.e., including *all local* signals, there were instances when this was not done. In other words the statistics for *reported* arrivals does not necessarily reflect the number of *detected* locals. The uncertainty about reporting policies of the GSETT stations makes it difficult to draw any firm conclusions about

TABLE I
DETECTIONS AT GSETT STATIONS

Station	Detection (per day) Total	Local	Percent Local	Station	Detections (per day) Total	Local	Percent Local
AAI	1.6	0.0	0.0	MAT	11.0	3.3	30.3
APO	10.2	0.8	7.4	MAW	7.9	0.0	0.0
ASPA	21.0	0.9	4.3	MBC	8.5	0.0	0.2
BAA	0.0	0.0	0.0	MLR	1.6	0.2	14.5
BDF	0.8	0.1	7.9	MNS	1.5	0.7	46.7
BUD	1.3	0.1	4.5	MOX	3.5	0.7	18.8
BUL	2.0	0.0	0.0	NB2	10.4	0.6	5.7
COP	0.4	0.0	0.0	NNA	1.0	0.1	8.2
CTAO	15.5	2.8	17.9	NUR	5.6	0.0	0.0
DAG	4.0	0.0	0.0	NWAO	4.1	0.4	10.5
DKM	0.7	0.4	63.6	OBN	1.9	0.0	0.0
DBN	0.7	0.1	15.2	PMO	0.2	0.0	0.0
DOU	4.3	2.0	46.4	PRU	6.1	0.4	6.6
EKA	13.4	9.3	69.3	PSI	1.8	0.0	0.0
ENN	3.4	1.2	34.3	PSZ	1.8	0.5	27.0
FBAS	21.2	5.8	27.4	PPT	0.1	0.0	0.0
GAC	2.9	0.4	13.5	RDJ	0.1	0.0	0.0
GBA	6.7	0.0	0.0	RMP	0.4	0.0	0.0
GDH	0.4	0.0	0.0	RSNY	6.8	3.2	47.3
GRA1	10.0	5.8	57.8	RSON	9.3	4.2	44.8
HFS	12.3	1.2	9.6	RSSD	13.3	4.3	32.8
IR4	0.2	0.0	0.0	SLL	11.1	0.8	7.4
JAY	0.3	0.0	0.0	SMY	0.4	0.0	0.0
JOS	2.4	0.4	17.9	SPA	5.8	0.0	0.0
KBA	6.5	2.9	44.1	SUF	7.1	0.0	0.0
KHC	9.0	0.4	4.5	TBY	4.8	0.8	17.0
KSI	0.2	0.0	0.0	TRT	0.9	0.0	0.0
KUG	0.8	0.0	0.0	UCC	1.8	0.3	15.9
LAC	7.6	1.2	16.5	VAO	0.1	0.0	0.0
LOR	3.6	0.6	17.1	VTS	2.8	0.1	2.2
LPB	8.6	0.0	0.0	WEL	0.1	0.0	66.7
LSZ	2.4	0.0	0.8	YKA	9.4	0.2	2.2
LTX	17.1	5.9	34.6	Tot	332.8	63.1	19.0

detection of locals. The numbers in Table I, however, represent lower limits, which for some stations may well be equal to the actual number of detected signals. Table I shows that about 20% of all reported detections were local. There is, however, large variation for the number of locals among the stations. And between 0 and almost 70 % of the total number of detections were reported as locals for stations that reported more than five detections a day. The largest average number per day of *reported locals* for all the GSETT stations was about 10 (EKA). The largest *total* number of detections per day (i.e., including locals) was about 25 (ASPA). Table I also shows that most of the locals (almost 80%) were reported by only 11 (or about 15 %) of the stations.

The number of detected locals depends largely on the artificial and natural seismic activity in the vicinity and neighboring area of the station, whereas the number of teleseismic detections should be less regionally dependent. This is illustrated by *Figure 1*, which shows the number of reported local detections per day plotted as a functions of the number of teleseismic detections. Only stations with at least five detections (teleseismic and locals) are included in the scatter diagram. Stations that reported no local have arbitrarily been assigned 0.1 local detection per day. There is much larger scatter (about two orders of magnitude) in the number of locals than in the number of teleseisms (less than one order of magnitude), and the empirical distribution of the number of locals is reasonably well approximated by a normal distribution as illustrated by *Figure 2.*

2.3.3. Hypothetical Networks

A series of examples of calculated capabilities are given for the following three hypothetical networks:

(i) A GSE global network represented by the example concept network (GSE/US/44, 1987);

(ii) A network of *auxiliary* stations with continental coverage drawn from a set of globally distributed stations reporting to existing international seismological services;

(iii) A *specialized* network of local and regional stations in Eurasia (Evernden *et al.* 1986).

The example concept network consists of 42 single element stations (assumed noise 5 nm) and eight array stations (assumed noise 1 nm) with a fairly uniform geographical distribution *(Figure 3).* Five of the stations (one of which has an array) are assumed to be on the territory of the U.S.S.R. For the sake of comparison we use in some of the calculated examples noise values according to tectonic region (shield = 10, platform = 15, tectonic = 25, oceanic = 50 nm, respectively, see note on Tectonic Region and Detection Thresholds in this report).

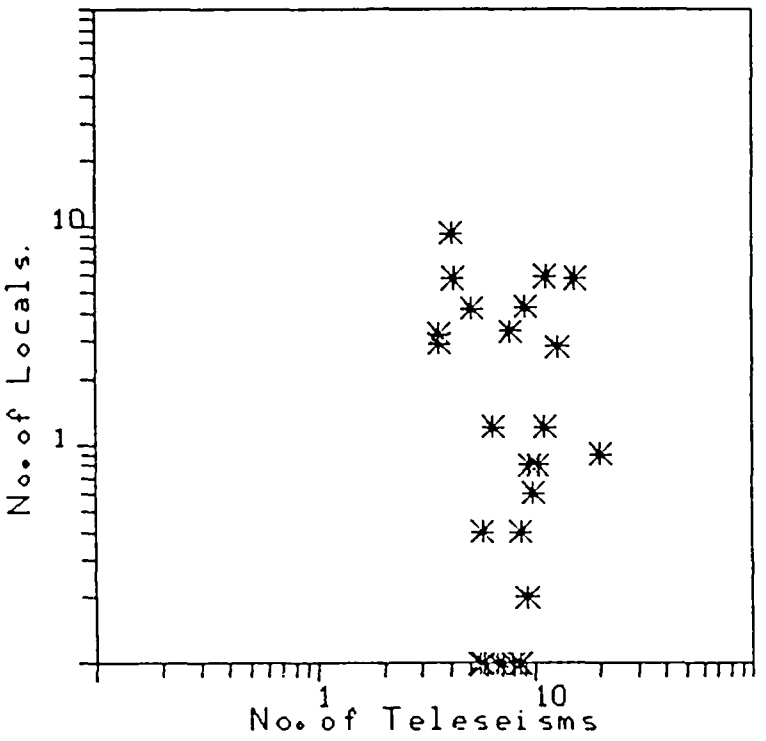

Figure 1. The scatter diagram shows the daily number of locals plotted as against the daily number of teleseisms reported by GSETT stations. Only stations with five or more detections (local or teleseisms) per day are included in the diagram. Stations with 0.1 or less locals reported per day have been assigned 0.1 locals per day in the diagram.

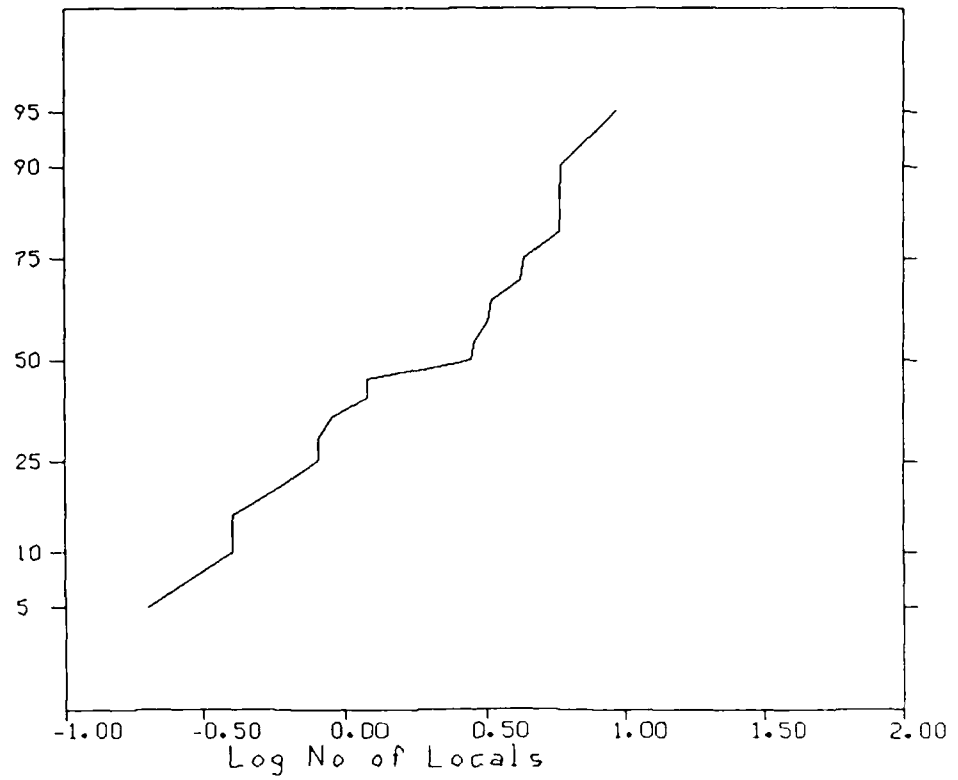

Figure 2. The diagram shows the empirical distribution of the number of locals reported per day (on a logarithmic scale and excluding stations with 0.1 or less reported locals per day). The vertical scaling of the diagram is such that a normal distribution appears as a straight line.

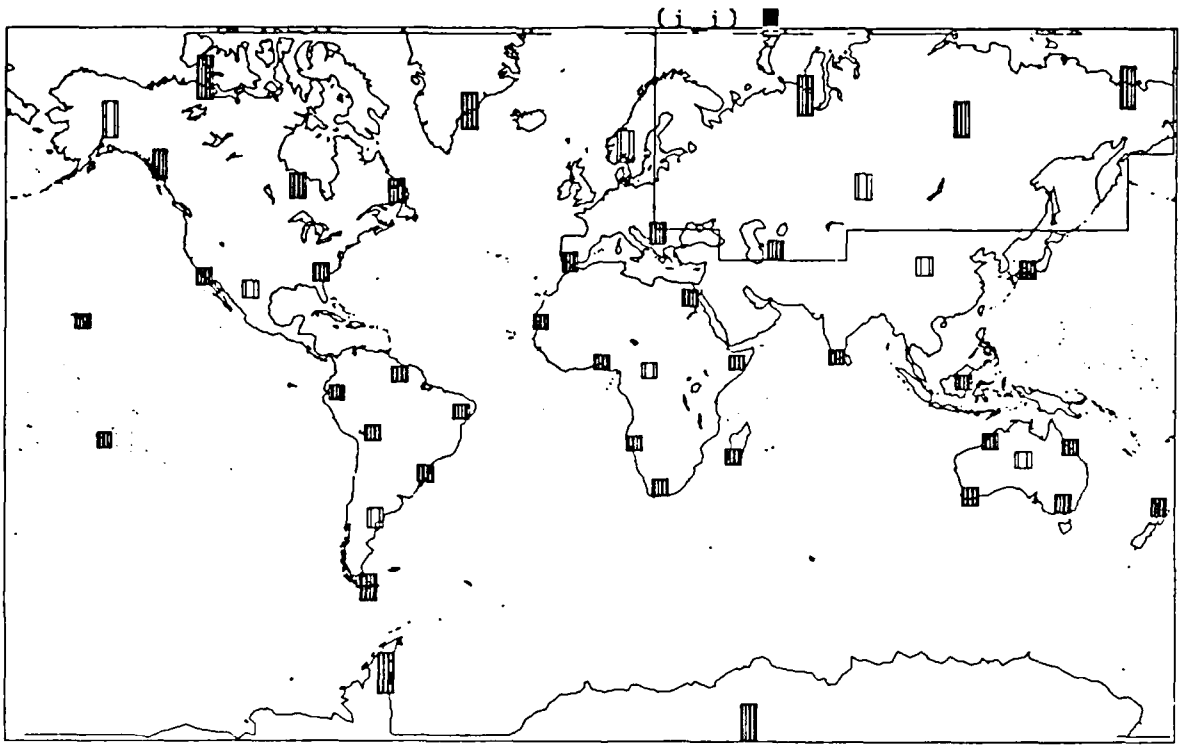

Figure 3. Stations of the example GSE concept network. Arrays (in all eight) are indicated by symbols with less shading. The region of Eurasia as defined in the text is also marked on the map.

The hypothetical network of *auxiliary* stations have been selected from existing stations as listed in the station table (including some 5000 stations) at the Center for Seismic Studies, which in turn is based on the NEIS station list. This hypothetical network includes 528 stations (Cf. *Figure 4*) with a station spacing of about 500 km. Station noise is assumed to be according to tectonic region as given above, since these stations do not usually have very low detection thresholds. The stations of the GSE conceptual network are assumed to have been carefully sited and to be equipped with modern instrumentation.

The *specialized* network of 40 stations covering large parts of Eurasia has been defined by Evernden *et al.* (1985) *(Figure 5).* Twenty-five of these stations are inside the territory of the U.S.S.R. We use a standard noise amplitude value of 5 nm since these stations are assumed to be equipped with modern three-component instrumentation. None of these specialized stations is, however, assumed to be an array station.

Notice that the coverage of the auxiliary network virtually coincides with that of the concept network. This means that it appears possible to select a network with fairly uniform geographical distribution from existing stations. The stations of such a selected network may, however, not have noise amplitudes as low as 5 nm.

In conclusion, the most optimistic assumptions about noise amplitudes have been made for the GSE concept stations, which represent a future network. The difference in assumptions about station noise values corresponds to a difference in detection threshold of about 0.3 - 0.5 magnitude units.

2.3.4. Parameter Values

The calculations were carried out with the SNAP/D program. For this purpose the computational parameters of the SNAP/D data base (Rivers *et al.* 1985) were used with some exceptions.

Amplitude distance curves for *explosions* (i.e., surface focus) were used in all examples of event detection and calculation of depth errors. The curves were extended beyond 100 degrees using the empirical amplitude distance curves for P-waves compiled by Lilwall (1987).

The amplitude attenuation was also a function of tectonic region (stable or tectonic), and so called squelching of L_g phases was used in accordance with the regionalization of the SNAP/D data base.

Amplitudes of "noise" for local phases (P_g, S, and L_g) were defined from the station noise for P-waves multiplied by a factor of 2.5, a procedure suggested in the SNAP/D data base.

Calculations were made for various detection criteria ("at least four P," "at least two P or P_g and two S or L_g," and "at least four P or PKP, not all $PKPs$"). For the GSE concept network these criteria are on the conservative side with regard to arrays, since only two array detections may define and locate an event according to GSE specifications.

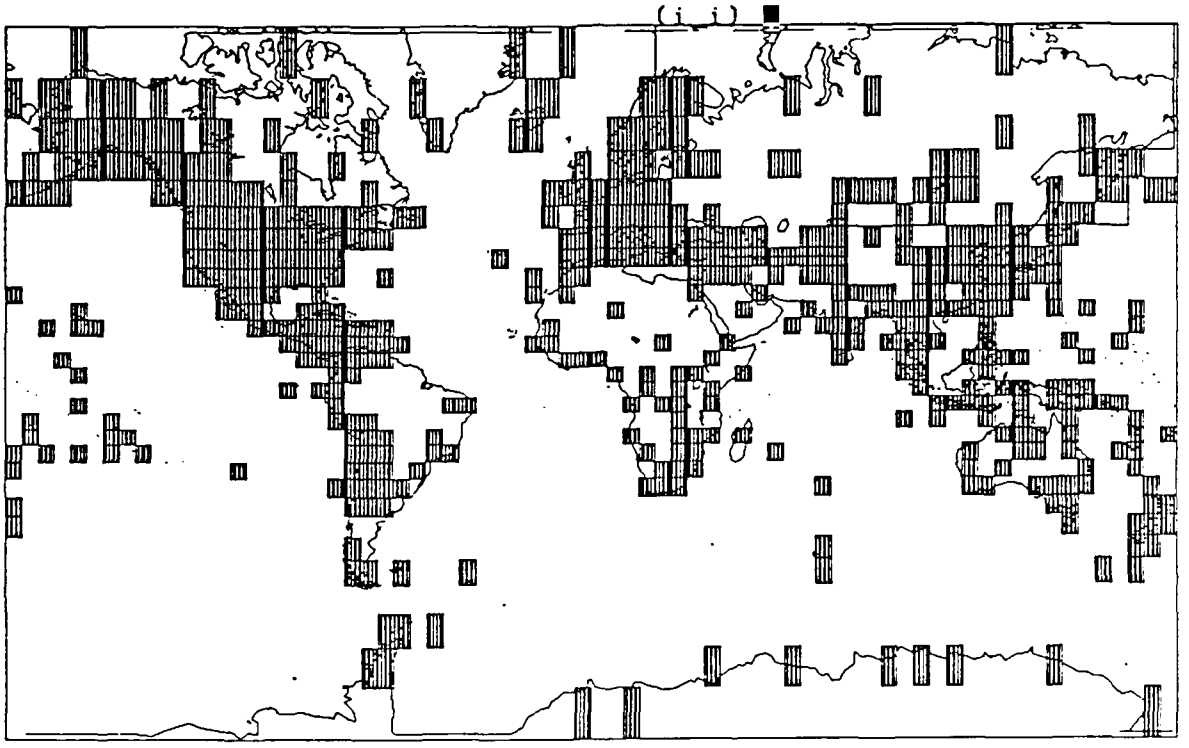

Figure 4. Stations of the auxiliary network. Each symbol covers an area of 5 by 5 degrees in latitude and longitude and the station is assumed to be located at center of this area.

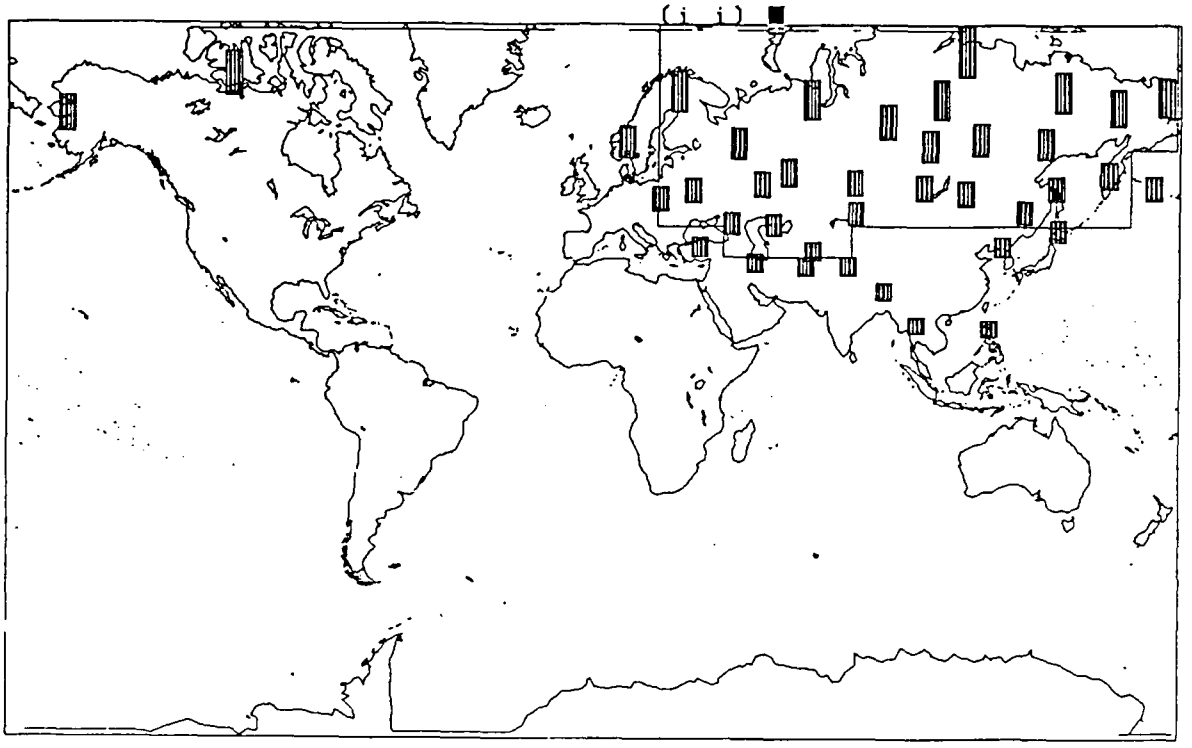

Figure 5. Stations of the specialized network defined by Evernden *et al.* (1985). The region of Eurasia as defined in the text is also marked on the map.

In the calculations for the network of auxiliary stations (528) only stations within 25 degrees were used from each grid epicenter in order to emphasis detection of local and regional phases. This means that in this case the detection thresholds and depth errors have been calculated for a "local" networks consisting of stations within 25 degrees (always less than 100 stations).

The depth error calculations were made based only on arrival times (no depth phases or master events) for explosions (i.e., surface focus). Surface focus was chosen since the depth errors are usually larger than for a focus at some depth.

2.3.4. Detection Thresholds

Calculated detection thresholds are summarized in Table II. The thresholds in the table represent average values either for the whole world or for Eurasia, as defined by the area marked in *Figures 3-5* (Latitudes 45-75N, longitudes 20-165E; 37-45N, 40-80E; 60-75N, 165-180E). The values in the table should only be used for relative comparisons between networks. The absolute threshold values depend critically on the assumptions of the computational parameters and should be interpreted with some care.

The worldwide average thresholds for the 50-stations GSE concept network illustrate several important points. Inclusions of local and regional detections at these stations does not significantly improve the detection capability. Use of *PKP* phases, however, lowers the threshold significantly (about 0.4 magnitude units). The difference between the thresholds of a network with low (5 nm) and high (10 nm or more according to tectonic region) noise amplitudes illustrates the importance of improving the performance of the network by improving its stations (lowering their thresholds) rather than adding new stations (the threshold decreases roughly as the logarithm of the square root of number of stations). Finally, the worldwide thresholds for the concept network also illustrates the significance of array stations. The dramatic lowering of the threshold due to use of PKP is partly owing to the eight array stations. If all stations had the same effective noise value one should expect a lowering of less than 0.3 (corresponds to almost doubling the stations on an hemisphere).

If we turn to the examples in Table II, it can be seen that the average threshold of the GSE concept network for Eurasia, is about the same as for the world. This is to be expected from this fairly uniformly distributed network. Moreover, the threshold for Eurasia of the GSE concept network is somewhat lower than that of the auxiliary network, which includes a much larger number of stations but with fairly high noise amplitudes. This again illustrates the importance of station quality in relation to station quantity.

The GSE concept threshold is also comparable to that of the specialized Eurasian network with same station noise assumptions (for single stations). The larger number of stations (40 as compared to 12) of the specialized Eurasian network is compensated for by the array stations of the GSE concept network.

TABLE II
DETECTION THRESHOLDS FOR SOME HYPOTHETICAL NETWORKS

Network	No. of Stations	Noise	Detection Criterion*	m_b-Threshold World	m_b-Threshold Eurasia
GSE Concept	50	5 and 1 nm	*P*	4.18	4.09
GSE Concept	50	5 and 1 nm	*P*+Loc	4.16	4.06
GSE Concept	50	5 and 1 nm	*P*+Loc+*PKP*	3.73	3.58
GSE Concept	50	5 nm	*P*+Loc+*PKP*	3.96	3.94
GSE Concept	50	Tectonic	*P*+Loc+*PKP*	4.51	4.49
GSE Concept	8	1 nm	*P*+Loc+*PKP*	4.05	4.08
Auxiliary	528	Tectonic	*P*+Loc		3.98
Specialized	40	5 nm	*P*+Loc		3.62
Specialized	40	Tectonic	*P*+Loc		4.18

* Detection Criteria:
P = four or more *P* detections
Loc = at least two *P* or P_g and two or more S or L_g
PKP = four or more *P* or *PKP*, not all of which are *PKP*

2.3.5. Depth Errors

The depth estimation capability is studied here for explosions (i.e., surface focus) and it is assumed to be based on arrival times only (*P*, P_g, *S*, and L_g). As a measure of depth estimation capability we use the length of the 90% confidence interval for events at given magnitudes.

Average depth errors for various networks and cases are summarized by Table III. The errors have been computed for events with magnitudes m_b=4.0 and 4.5. As the case for the detection thresholds, the relative values of the average errors can be interpreted more readily than the absolute values.

The data for the GSE concept network shows that use of local and regional phases indeed reduces the depth error significantly (between a factor of two and three). Although the detection capability of the auxiliary station network is much lower than that of the concept network, the depth errors are smaller. Moreover there is a significant difference in depth errors between the specialized and the concept network (more than a factor of two), even if the two networks have similar detection capability.

Assumptions about the parameter values in the depth error calculations are not as well supported by empirical data as for the detection thresholds. Calculations like this are also more difficult to compare with empirical data and assessments. Therefore, the average values in Table III are only qualitative indicators of the depth determination capabilities rather than precise estimates.

TABLE III
DEPTHS ERRORS FOR SOME HYPOTHETICAL NETWORKS

Network	No. of Stations	Noise	Detection Criterion*	m_b	Depth Error(km)
GSE Concept	50	5 and 1 nm	*P*	4.5	146
GSE Concept	50	5 and 1 nm	*P*+Loc	4.0	84
GSE Concept	50	5 and 1 nm	*P*+Loc	4.5	62
Auxiliary	528	Tectonic	*P*+Loc	4.0	77
Auxiliary	528	Tectonic	*P*+Loc	4.5	42
Specialized	40	Tectonic	*P*+Loc	4.5	44
Specialized	40	5 nm	*P*+Loc	4.5	27

* Detection Criteria:
P = four or more *P* detections
Loc = at least two *P* or P_g and two or more S or L_g
PKP = four or more *P* or *PKP*, not all of which [illegible] *PKP*

2.3.6. Auxiliary Stations and Mini-Arrays

The hypothetical network of auxiliary stations used in the examples here has a spacing of about 500 km with a fairly uniform coverage of the continent. Existing local and regional networks are, however, much less homogeneous. They often have a denser station spacing and the networks are also more clustered. The Canadian and Swedish networks can be used to illustrate characteristics and detection capabilities of existing networks set up to monitor local seismic activity (GSE/Canada, Sweden/1, 1987). The Canadian network, which includes more than 100 stations with a spacing of between 30 to 400 km covering the Canadian territory (about 9 million square km), can detect and locate earthquakes down to magnitude 3.5 (unspecified scale) or less anywhere in Canada (in some areas down to 2.5). The Swedish network includes some 20 stations with an average spacing of about 100 km (covering an area of about 0.15 million square km) has a detection threshold in the magnitude range 1.5 to 2.0 (Slunga *et al.* 1984).

Although there may be operational difficulties with auxiliary stations due to a variety of recording formats and inconsistencies in reporting of data, local and regional detections are significant for the overall performance of a global system. With these aspects in mind, the recently developed mini-arrays present an alternative that warrant further study. Arrays lend themselves easily to consistency in recording and operation. Moreover, they also have comparatively low detection thresholds. The 90% magnitude detection threshold at NORESS for *P*-waves from events in Finland and Western Russia within 500-1500 km (1500 km radius corresponds to an area of about 7 million square km) has been estimated at 2.7 (local Scandinavian magnitude scale; Ringdal, 1986). Assuming that S or L_g also is detected at this threshold, a rough location may be obtained. Assuming that the two magnitude scales (Canadian and Scandinavian) are comparable it thus appears that the detection capability of the entire Canadian network and of NORESS are not significantly different. The location accuracy of the Canadian network is probably much higher than that of NORESS, but $S-P$ times for calculating origin time may be sufficient to determine focal depth adequately.

2.3.7. Concluding Remarks

In this note we have looked at some aspects of the reporting of local and regional detections by stations of a global network and the significance of such detections for the overall performance.

The data reported for the GSETT illustrate that consistent reporting may be difficult to obtain in practice from a large network of auxiliary stations. Although instructions for reporting of station detections were developed and adopted before the GSETT, uncertainties about the actual reporting during the test remain, and differences in reporting policies can be noted.

On the other hand, the calculated examples for some hypothetical networks also illustrate the significance of local and regional data for a global monitoring system. Results from operation of the NORESS mini-array suggest that a fairly small number of such arrays could be a powerful alternative to a network of auxiliary stations. This suggestion has, however, to be substantiated by a more detailed study, which is beyond the scope of this note.

Hans Israelsson

REFERENCES

GSE/Canada, Sweden/1, 1987. *Working Document Submitted by the Canadian and Swedish Delegations to the Committee on Disarmament.*

GSE/SW, 1985. "Description and Evaluation of Procedures Employed at the Experimental Data Center in Stockholm," *Working Document Submitted by the Swedish Delegation to the Committee on Disarmament/f1.*

GSE/US/44, 1987. "Technical Concepts for a Global System for Seismic Data Exchange," *Working Paper Submitted by the U.S. Delegation to the Committee on Disarmament.*

Lilwall, R. C., 1987. "Empirical Amplitude-Distance/Depth Curves for Short-Period *P*-waves in the Distance Range 20 to 180 Degrees," *Atomic Weapons Research Establishment*, AWRE Report O 30/86.

Ringdal, F., 1986. "Regional Event Detection Using the NORESS Array," *Semiannual Technical Summary, 1 October 1985 - 31 March 1986*, Kjeller, Norway.

Rivers, W., Watson, A. B., and Ciervo, A.P., 1985. "Database for SNAP/D: Seismic Network Assessment Program for Detection," *Pacific-Sierra Research Corp.*, PSR Report 1551.

Slunga, R., Norrman, P., and Glans, A. C., 1984. "Seismicity of Southern Sweden," *National Defense Research Institute, Stockholm*, Report C2 C 20543-T1.

3. RESEARCH TO IMPROVE ANALYSIS OF REGIONAL SEISMIC DATA

3.1. PARTICLE-MOTION CHARACTERISTICS OF REGIONAL SEISMOGRAMS RECORDED AT NORESS

3.1.1. Introduction

Particle-motion characteristics of regional phases P_n, P_g, S_n and L_g are investigated using three-component seismograms recorded at NORESS. The dataset consists of 93 events, a mixture of earthquakes and mining explosions located within 20° of the array. Ground motions are characterized using a series of polarization "attributes" computed in short sliding time windows and in several frequency bands. Particle-motion information is extracted interactively by an analyst using displays of the three-component seismograms and polarization characteristics as a function of time to identify phases and select time segments.

There are two main objectives in this study. First, the analysis yields an understanding of the type of information available in the particle motions of regional phases, the sensitivity to factors such as noise, and how this information can be utilized in the context of monitoring at regional distances. The second objective is to implement and evaluate a procedure for extracting polarization information both interactively using a workstation and automatically using an on-line processor. The analysis procedure needs to be fast, robust, versatile and should require only a few input parameters. It also needs to be tested using an extensive dataset to determine sensitivity to noise and the optimum frequency bands and time window lengths for extracting the most useful polarization information for different phase types.

Several previous workers have investigated particle-motion information using regional seismograms. Flinn (1965) proposed a method for extracting the polarization ellipse in sliding time windows using the covariance matrix of the three components. His application involved displaying particle-motion parameters such as rectilinearity as a function of time and filtering the traces on the basis of polarization content. Smart (1977) developed a processor in which a least-squares fit of a polarization model is made to three-component data in the frequency domain. Smart and Sproules (1981) applied this method to short-period regional recordings from station RKON to estimate backazimuths from P_n and L_g waves. Von Seggern and Marshall (1982) also tested the Smart (1977) approach for estimating backazimuths and regional phase types. These studies showed that regional P_n as well as L_g phases give good backazimuth estimates and appear promising for identifying phase types. Samson and Olson (1980,1981) designed a technique for estimating the polarization state from the spectral matrix in the frequency domain. The analysis was carried out in sliding time windows and polarization filtering could be performed by applying the degree of desired polarization as a time-dependent gain function on the input data. Suteau-Henson *et al.* (1985) applied the polarization filtering method of Samson and Olson (1980, 1981) to RSTN recordings of regional earthquakes to enhance polarized arrivals within the *P*-wave coda. Magotra *et al.* (1987) recently described a method for automatically detecting and locating regional events using single-station three-component data. Their detector

computes the eigenproblem for the covariance matrix as a function of time and uses the maximum eigenvalue as a detection parameter. The source azimuth is computed using the eigenvector orientations. Magotra *et al.* conclude that using the three-component polarized power for detection at regional distances gives better performance than detectors which scan only the vertical component. Kvaerna and Doornbos (1986a,b) applied three-component analysis to regional seismograms at NORESS. Their approach uses multiple three-component sensors in an array with a frequency-domain covariance algorithm. They have also extended this algorithm using a Maximum-Likelihood principle. Besides successfully estimating backazimuths, Kvaerna and Doornbos (1986a,b) found that three-component information is very useful for detecting the secondary signals S_n and L_g and shows promise for distinguishing between them.

The outline of this report is as follows. First, the algorithm and the analysis procedure used to extract the polarization information is outlined. Then, results are presented of particle-motion characteristics for the different regional phases. Finally, a summary is given which draws conclusions from the results and makes recommendations about implementing a particle-motion analysis either automatically or interactively. The dataset of 93 events used in the analysis is listed and briefly described in Appendix I.

3.1.2. Analysis Procedure

The NORESS array contains several three-component sensors. Jurkevics (1986a,b) developed a technique for estimating polarization information which uses either single stations or multiple three-component sensors in an array. This approach, which involves averaging the covariance matrices between sensors in an array, yields a 1/N reduction in estimation variance when the noise and scattering effects are uncorrelated between sensors. (Here N is the number of three-component sensors in the array.) The analysis is carried out entirely in the time domain. Frequency dependence is introduced by bandpassing the data into several frequency bands and performing a separate analysis in each band. Identical short overlapping time windows are applied to all three components of motion. The 3x3 covariance matrices are computed at each sensor within the short computation windows. Then the covariance matrices are averaged together for all the sensors. This approach is general in that a single-station analysis is similar without the covariance-matrix averaging. Solving the eigenproblem of the covariance matrix yields a least-squares estimate of the polarization ellipsoid. The three principle axes of the polarization ellipsoid are given by the eigenvalues (amplitudes) and eigenvectors (orientations). A series of attributes describing the ground motion is computed from the eigenvectors and eigenvalues. The computation windows are moved along in time and the entire process is repeated for each frequency band. During most of the events used in this analysis the NORESS array contained four three-component sensors; three on the "C" ring and one at the center.

The analysis was of the regional seismograms was performed interactively using a Sun workstation. Three frequency bands were used, centered at 4 Hz (2.7-5.3 Hz), 6 Hz (4-8 Hz) and 10 Hz (6.7-13.3 Hz). The time resolution (i.e., short computation window length) was set to five cycles of each passband center frequency. No time shifting was used to align the time windows between the sensors to compensate for the time lags of the wavefronts across the array. Tests using NORESS

data have shown that a simple zero-lag summation without time alignment works as well as using shifts based on the horizontal phase velocities from a frequency-wavenumber analysis. This is because the combination of window length, horizontal phase velocity, signal stationarity and frequency bandwidth is such that distortions due to window mis-alignment between sensors are negligible in most cases.

Particle-motion attributes were extracted from the signals at time picks selected by the analyst. The program displayed several polarization attributes as a function of time to assist the analyst in identifying the phase types and recognizing the onset and end times of pure particle motion. The sliding computation windows were made quite short in order to give a high resolution display of the time-varying polarization content. The attributes were extracted over time windows of varying length depending on the phase type; these extraction windows were at least 2 seconds long and always included several of the short computation windows used to compute the covariance matrices. The polarization attributes from neighboring computation windows were simply averaged together and output to a file. The averaging over several computation windows resulted in more stable parameters than if a single short computation window of about 5 cycles time duration was used.

Figure 1 shows a composite of several of the steps during the analysis of a typical event. This example is an earthquake (m_b = 2.8) on Oct 27, 1985 located 3.3° due west of NORESS near the coast of Norway. The three components of motion are shown in two frequency bands in the lower part of *Figure 1*. First, the pointing device is used to select a time segment for P and one for S, each about 40 - 50 seconds long. The P segment is chosen to include the ambient noise, P_n, P_g and the early *P*-wave coda. The S segment includes the late *P*-wave coda, S_n and L_g phases. Several polarization attributes are then displayed (top of *Figure 1*) for each of these segments in two frequency bands. The attributes displayed here are the three-component amplitude, the rectilinearity for the P segment and the horizontal-to-vertical ratio for the S segment. A menu selection is used to identify each phase type before it is picked. In the P segment, picks are made for noise, P_n and P_g (early P coda). In the S segment, late P coda, S_n and L_g picks are made. Two extraction window lengths are used for S_n and L_g. The window lengths over which the attributes are averaged vary for the different phases and are listed in Table I.

Table I

PHASE	EXTRACTION WINDOW
noise	± 3 sec
P_n	± 1 sec
early *P* coda	selected by analyst
late *P* coda	± 3 sec
S_n	± 1 sec
S_n	selected by analyst
L_g	± 1 sec
L_g	selected by analyst

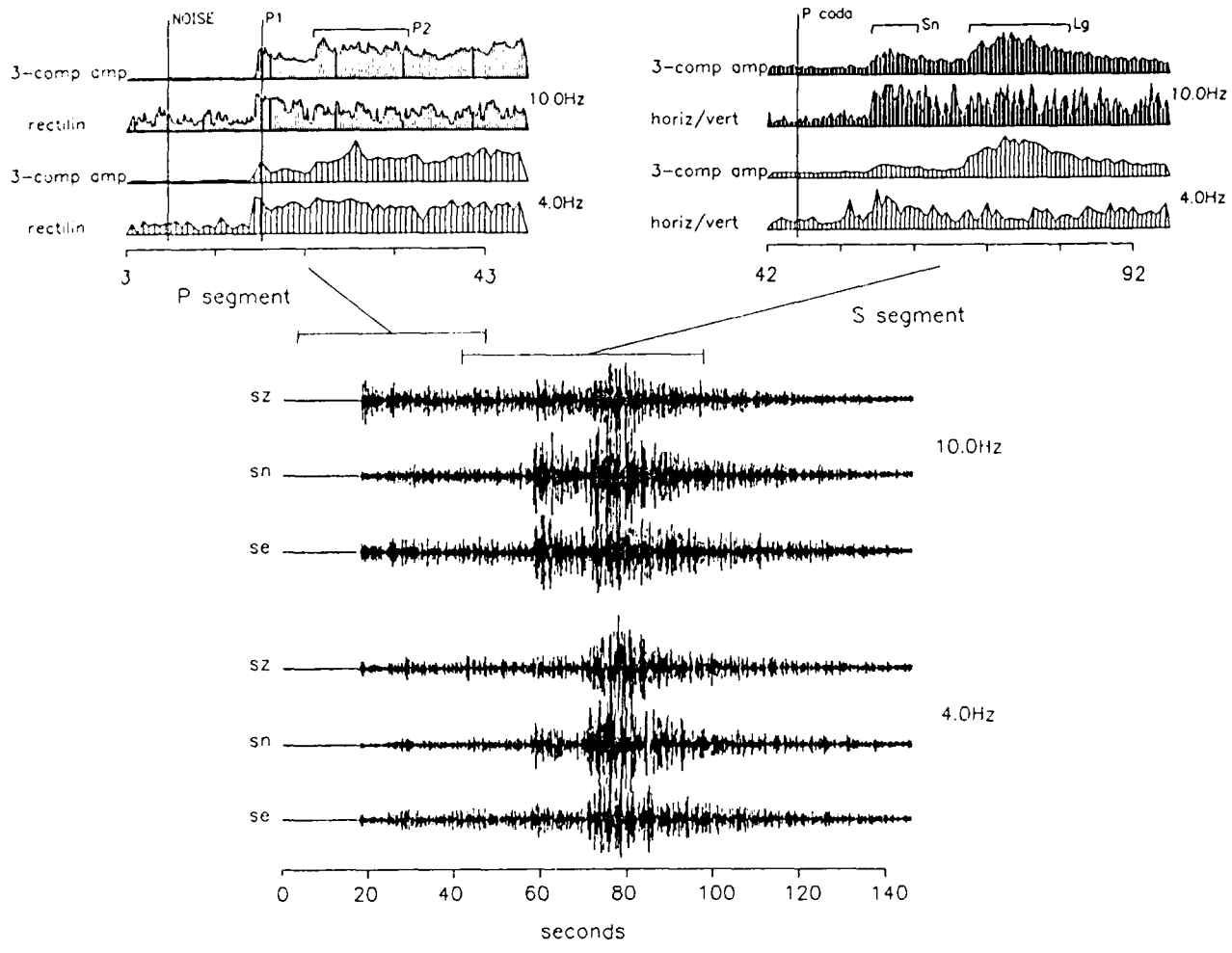

Figure 1. A composite of screen images during the analysis of a typical regional event. Below are shown bandpassed three-component seismograms recorded at NORESS from an earthquake 3.3° west of the array near the coast of Norway. First, the analyst selects a *P*-wave segment including some noise, P_n and early *P* coda signals. Two polarization attributes are displayed as a function of time in two frequency bands at the top of the screen. This display allows the analyst to pick the extraction windows for each phase from which the particle-motion information is output to a file. After the *P*-waves are processed, a second segment is chosen which includes some late *P* coda, S_n and L_g signals. The picks made by the analyst for each of these phases are shown at the top.

The noise sample is taken just prior to the P_n arrival. The P_n phase (labelled P1 in *Figure 1*) is picked at the time the P_n amplitude and rectilinearity are largest. The early P coda (P2 in *Figure 1*) window is variable length and includes the P_g arrival if it is present. This window is generally about 5-15 seconds long. If P_g is not visible, this window is situated in the early P-wave coda between about 5 and 25 seconds following the P_n arrival. The late P coda is picked just prior to S_n. Two picks are made for each of S_n and L_g; a short window $\pm$ 1 sec long and a longer variable-length one. The short windows are situated at the time of the peak signal amplitude. The variable-length windows are based on the shapes of the three-component envelopes and include the time durations over which the three-component amplitudes are above about 40% of their peak values. The variable-length windows were typically 3-8 seconds for S_n and 10-20 seconds for L_g.

These choices for window lengths and frequency bands were made after an initial trial-and-error analysis of about 30 recorded events. Choosing a time window to encompass the duration of pure particle motion and exclude the adjacent randomly-polarized noise, coda waves or overlapping phases is an important factor affecting the quality of estimated particle motions. One of the objectives in this study is to determine how to select optimum frequency bands and time windows for extracting the most useful polarization information for all the phases under a variety of signal-to-noise conditions. Ideally, these settings should be independent of the source type, distance and signal-to-noise level, so that the analysis can be more easily automated or used interactively by an inexperienced analyst. The best particle-motion information for any arrival is generally between the phase onset time and shortly after the peak amplitude.

In this study fixed frequency bands, as opposed to variable frequency intervals based on the S/N as a function of frequency, were used. With the fixed bands the quality of particle-motions can be evaluated as a function of frequency. Results of this study indicate that P_n and S_n have well-defined polarization across the entire short-period band whenever the signal is above the noise. However, even though the signal-to-noise ratio of L_g may be quite large, the polarization information may be poor at the higher frequencies. This is because the L_g waves may be present at low frequencies, but at higher frequencies the L_g waves have been attenuated and the signals on the seismograms at the L_g times are actually late S_n coda waves. S_n coda waves following the arrival time by more than a few seconds are not well polarized.

3.1.3. Results

In this section, various particle-motion attributes for the regional phases are examined. Plots are presented of the attributes as a function of noise level in the three frequency bands. Not all phases for all events are included in the plots; when the amplitude of a phase did not stand out clearly above the noise, the phase was not picked. The signal and noise values used are the three-component amplitudes averaged over the extraction windows. The noise level for P_n and early P coda waves is taken as the noise amplitude prior to the onset of the P_n phase. The noise level for the S_n and L_g waves is taken as the late P coda amplitude just prior to the onset of the S_n phase. The late P coda serves as the "effective" noise level for S_n and L_g because it tends to be randomly polarized and underlies both the S_n and L_g phases.

A common application of three-component analysis is to estimate source azimuth using the orientation of rectilinear *P*-wave motion. *Figure 2* shows the error in estimated source azimuth using *P* particle motion as determined in this study. The azimuth was computed as simply the horizontal orientation of the eigenvector corresponding to the largest eigenvalue of the covariance matrix. (The sign of this eigenvector is taken with a positive vertical component, so there is no 180° ambiguity for *P*-waves.) The values plotted in *Figure 2* are the true azimuth from the known source locations minus the backazimuth estimated from the particle motions. There is a decrease in the error as the signal-to-noise level increases. Taking the data for all noise levels, one standard deviation in the azimuth error for P_n is 10°, 12° and 14° for the 4, 6 and 10 Hz bands, respectively. For the early *P* coda one standard deviation is 12°, 16° and 17° for the same bands. These azimuth estimates are better than would be obtained using a single three-component station because of the 1/N reduction in estimation variance using the four sensors in the NORESS array. The variance can be further reduced by combining the estimated azimuths from the frequency bands for which S/N > 1.0 into a single "wide-band" estimate.

Source azimuth estimates can also be made from L_g waves. Von Seggern and Marshall (1982) used the orientation of the minimum horizontal motion of L_g wavetrains from single stations to obtain source azimuths which were comparable or even better than those obtained from rectilinear *P* motion. The L_g motions for their dataset were found to have consistently smaller radial than transverse components. *Figure 3* shows the errors in source azimuth using the minimum horizontal motion of L_g. This value was computed as the orientation of the eigenvector corresponding to the smallest eigenvalue computed using the horizontal components of motion. There is a 180° ambiguity in this azimuth. The values plotted in Figure 3 were computed using the sign which gave the smallest error. The upper set of plots are for an extraction window of ± 1 sec centered at the time of the peak L_g envelope. The lower plots are for a variable-length window which depended on the shape of the L_g wavetrain and generally lasted 10 to 20 seconds. The L_g azimuth errors are a strong function of frequency and are considerably smaller for the longer windows than for the shorter ones. One standard deviation for the variable-length windows is 16°, 27° and 36 ° for the 4, 6 and 10 Hz bands, respectively. For the ± 1 second windows one standard deviation is 26°, 32° and 41° for the 4 Hz, 6 Hz and 10 Hz bands respectively. Thus, the L_g azimuths are not as accurate as those estimated from P_n motions. The skewed distribution of points in *Figure 3* particularly visible at 10 Hz are associated with source location. The cluster of points at 10 Hz with low S/N values and positive errors are all from mining explosions 800-900 km east of NORESS. These waves appear to be arriving at the array from a more southerly direction than the true azimuth. This is likely due to geologic inhomogeneities along the propagation paths.

Figure 4 shows the rectilinearity of the noise, P_n and early *P* coda waves. Rectilinearity is computed from the eigenvalues of the covariance matrix as $1 - (\lambda_2 + \lambda_3)/(2\lambda_1)$, where the eigenvalues are ordered with λ_1 the largest. The values for noise are plotted at S/N = 1.0. The *P*-wave rectilinearity is about equal to the noise rectilinearity when S/N = 1 and increases with signal-to-noise level at all frequencies. The rectilinearity is larger for P_n than for the early *P* coda. This is because the P_n extraction window was situated at the time of the first arrival where the motion is most purely polarized. The early *P* coda window contains more scattered energy arriving from random directions and so these particle motions appear more like noise.

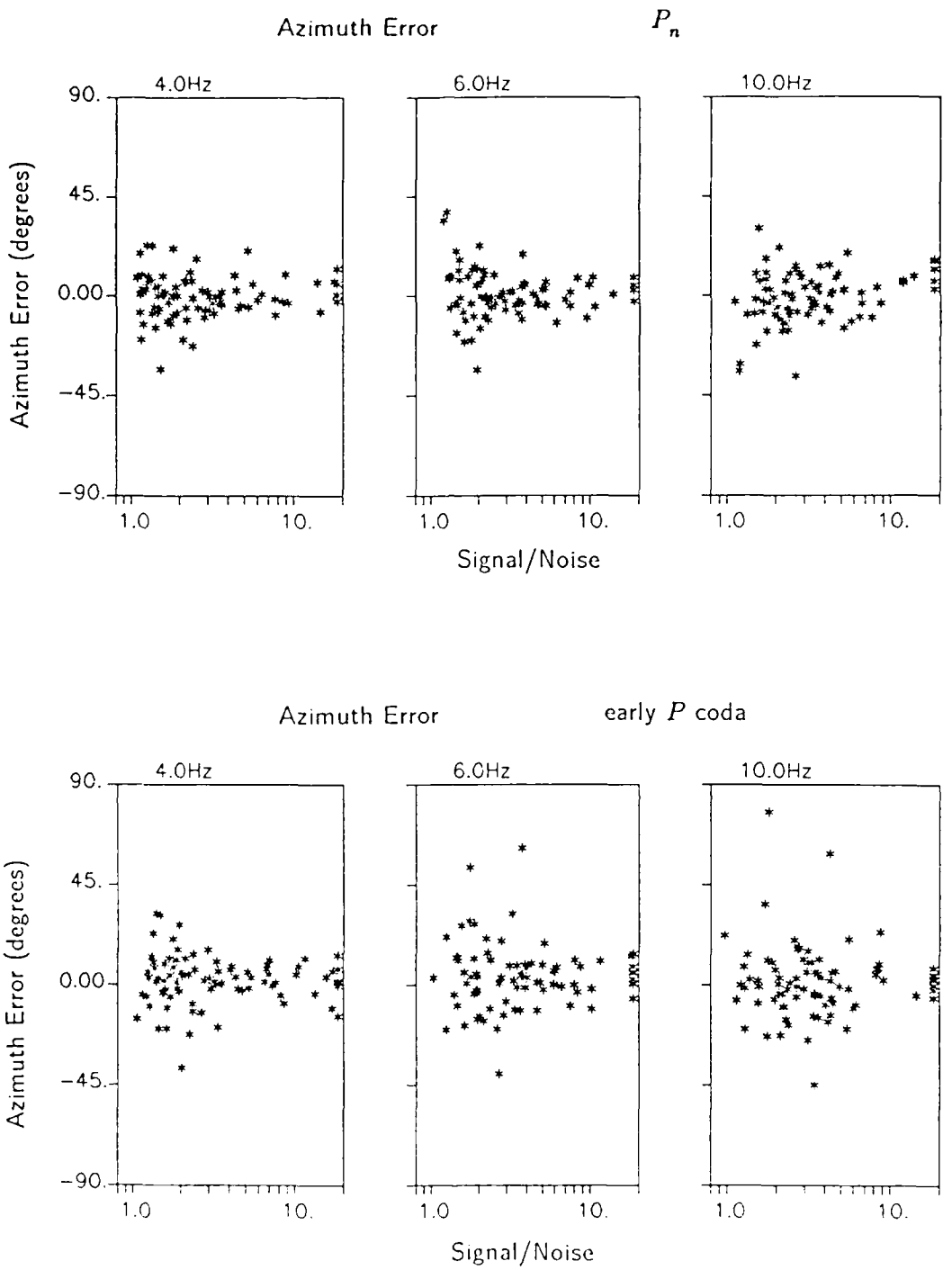

Figure 2. Azimuth errors for P_n waves and early P coda waves computed in three frequency bands. The values are plotted as a function of the three-component P amplitudes relative to three-component amplitudes of noise prior to P_n.

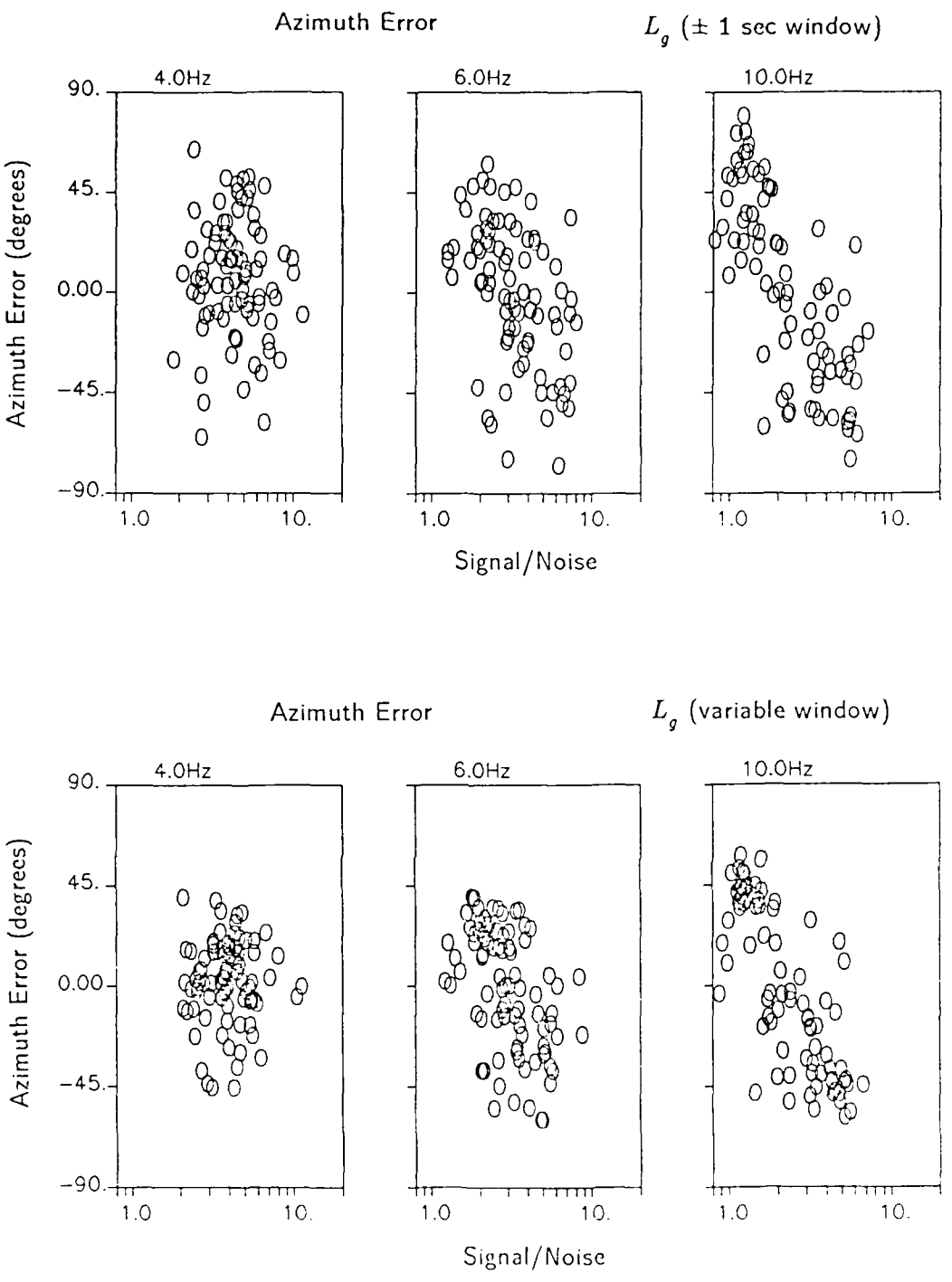

Figure 3. Azimuth errors for L_g waves using the fixed-length ±1 second extraction windows as well as variable-length windows. Results are plotted as a function of the signal-to-noise level. In this case the noise was taken as the late *P*-wave coda just prior to the onset of S_n. The longer variable-length windows give somewhat more accurate azimuths.

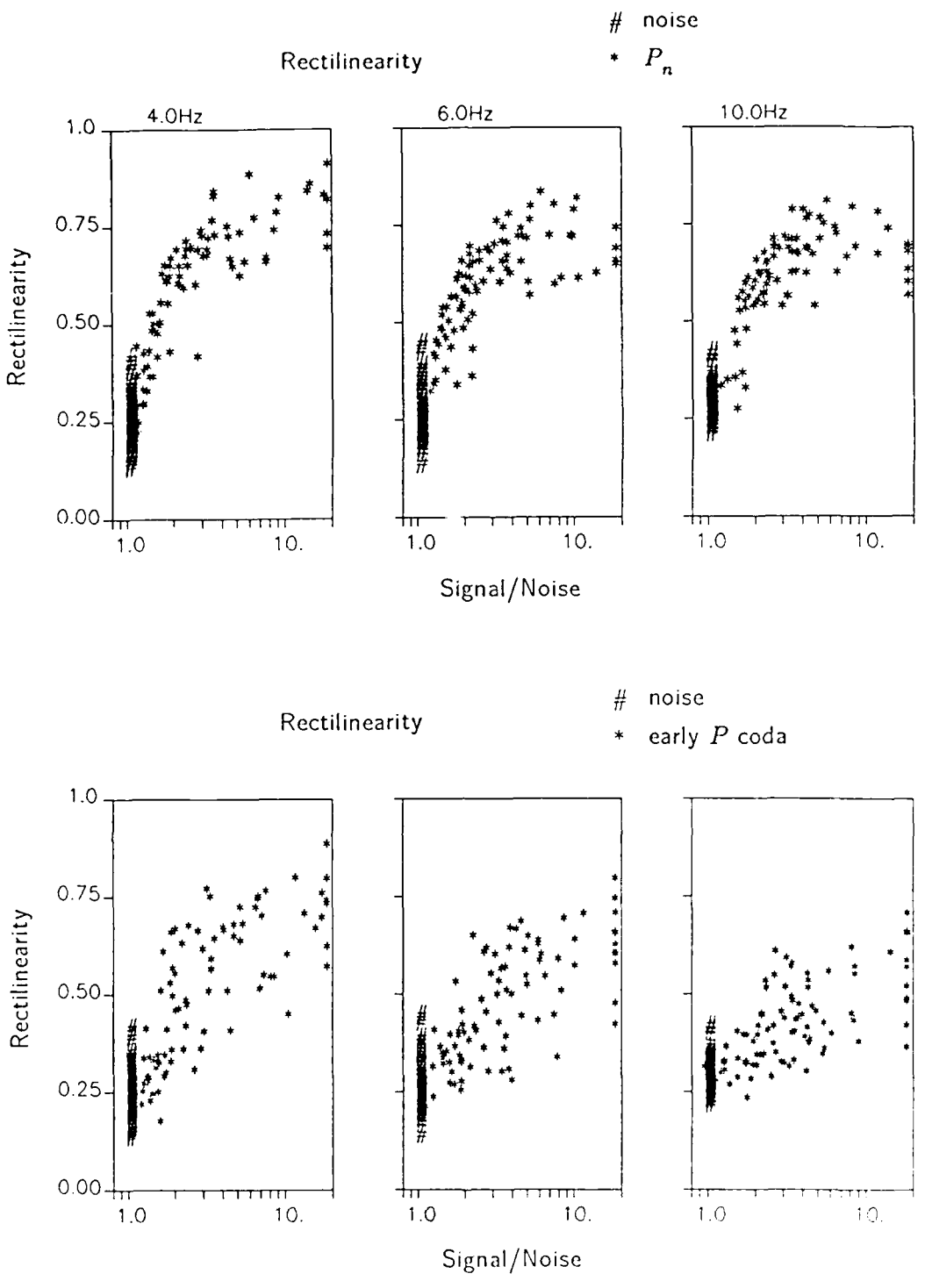

Figure 4. Rectilinearity of P_n and early P coda waves plotted as a function of the signal-to-noise level. The rectilinearity of the noise prior to P_n is also shown at S/N = 1.0. The P rectilinearity increases with signal-to-noise level. The values for the early P coda are lower at the higher frequencies due to the randomizing effects of local earth scattering. The P_n extraction windows were situated at the onset of this phase where the rectilinearity tends to be highest.

Figure 5 shows the angle of incidence of rectilinear motion of the *P*-waves. This is simply the orientation, measured from vertical, of the eigenvector corresponding to the largest eigenvalue. The P_n values are shown above and the early *P* coda below. The scatter for P_n tends to decrease with increasing signal-to-noise level. Purely random noise should have incidence angles with a large scatter and a mean of about 45°. The P_n waves with signal-to-noise levels above about 3.0 in *Figure 5* show a decrease in incidence angle with increasing frequency. The angles vary from about 45° at 4 Hz to about 30° at 10 Hz. There does not appear to be any correlation between the rectilinear incidence angle and source distance for the P_n waves. The incidence angles at 4 Hz for the early *P* coda waves are generally larger than 40°, which means that the radial components of motion are generally larger than the verticals. The trend of decreasing incidence angle with frequency is less defined for the early *P* coda than for P_n. The incidence angles for the early *P* coda do show a dependence on source location. Most of the values greater than 57° are from the mining explosions 8° - 9° east of the array.

Figure 6 shows the vertical-to-horizontal amplitude ratios of the noise, P_n, S_n and L_g. The values plotted for S_n and L_g are for variable-length extraction windows. The vertical-to-horizontal ratio is computed as $2Z/(E+N)$, with the factor of 2 introduced simply to normalize the values to 1.0 when all components are equal. The noise, which is plotted at S/N = 1, has average V/H values somewhat less than 1.0. P_n waves are clearly distinct from the other phases. Their V/H values increase with increasing signal-to-noise level. The fact that the vertical-to-horizontal ratios for P_n increase with frequency is consistent with the P_n incidence angles in *Figure 5*. Note that an incidence angle of 45° in *Figure 5* corresponds to a V/H value of 2.0 instead of 1.0 in *Figure 6*. This is due to the factor of two introduced in the equation for V/H to yield a value of 1.0 when the three components are equal. S_n waves have considerably smaller vertical motions compared with horizontals. The V/H values for S_n tend to decrease with increasing S/N, and are very well separated from the noise at 10 Hz. The L_g waves have vertical-to-horizontal ratios which cluster tightly at 4 and 6 Hz and are similar to the values for noise. At 10 Hz the average L_g signal-to-noise level is smaller than it is at lower frequencies. Some of the larger-amplitude L_g waves overlap with S_n in *Figure 6*. This is because many of the 10 Hz signals at the time of L_g actually consist of higher-amplitude S_n coda waves, as the L_g signals have been strongly attenuated above about 7 Hz.

Figure 7 shows the relative amplitudes of the radial, vertical and transverse motions for noise, S_n and L_g. These results are for the variable-length windows. The top diagrams show the ratios of radial-to-transverse (R/T) motions. The noise values, plotted at S/N = 1, have a mean of about 1.0 and a considerable scatter. The S_n waves have R/T values very similar to those of noise. The L_g waves have radial motions which are consistently smaller than the transverse motions at lower frequencies. This property was previously used to obtain the source azimuths from L_g waves. The lower diagram in *Figure 7* shows the radial-to-vertical (R/V) ratios. The S_n waves have radial motions considerably larger than verticals at all frequencies. L_g motions, on the other hand, have radials smaller than verticals at 4 and 6 Hz. At 10 Hz the L_g motions are quite similar to the noise.

Another parameter computed (but not shown here) was the planarity of the S_n and L_g motion. Planarity is simply a measure of the relative size of the shortest axis of the polarization ellipsoid. Both S_n and L_g motions tend to be more planar

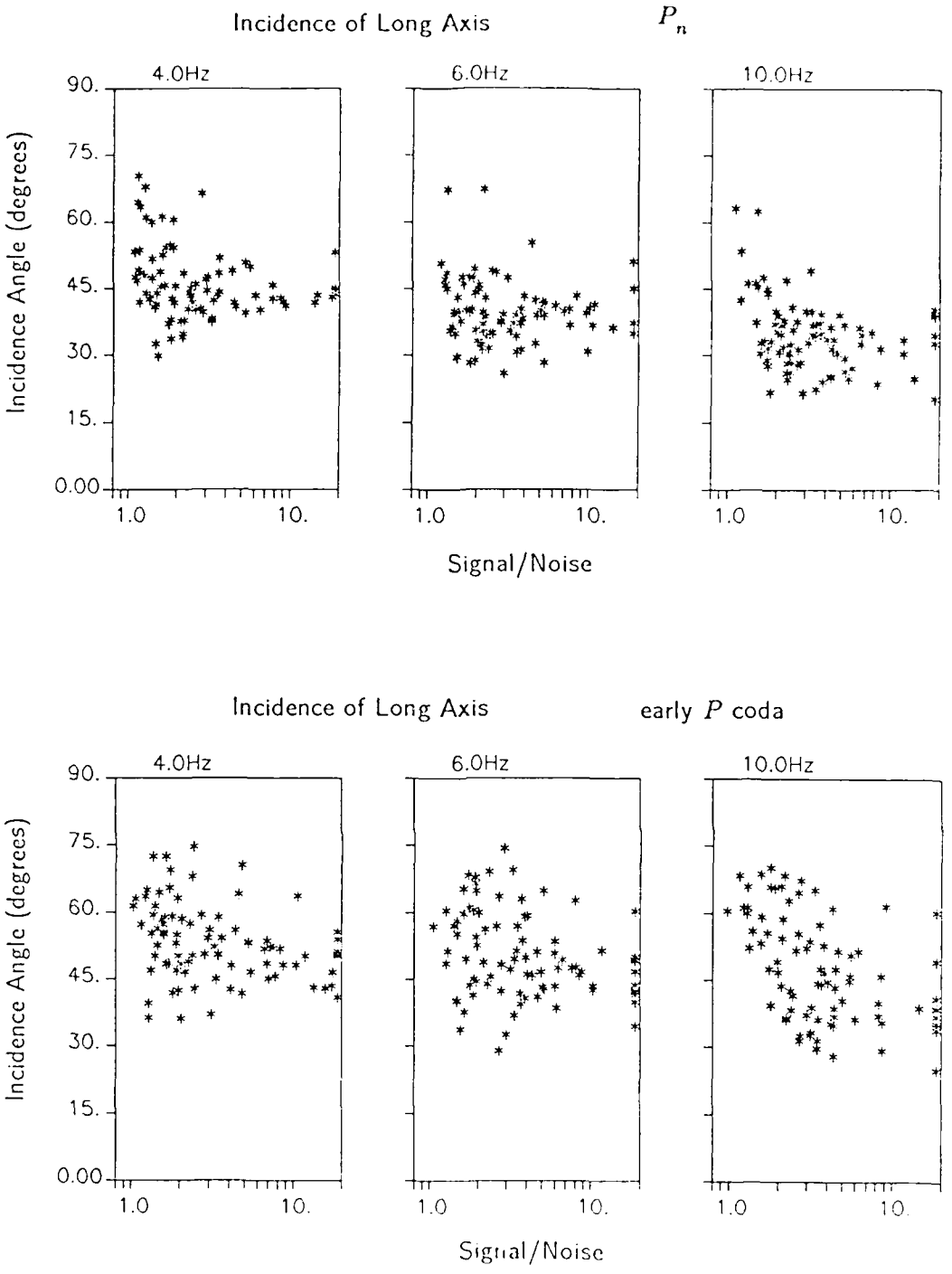

Figure 5. Incidence angles of the longest axis of the polarization ellipsoid, measured from vertical. This corresponds to the incidence angle of the rectilinear *P*-wave motion. The values for P_n are shown above and for early *P* coda below. The incidence angles for P_n tend to decrease with increasing frequency, and the P_n values are generally smaller (steeper) than those of the early coda arrivals (which usually contained P_g).

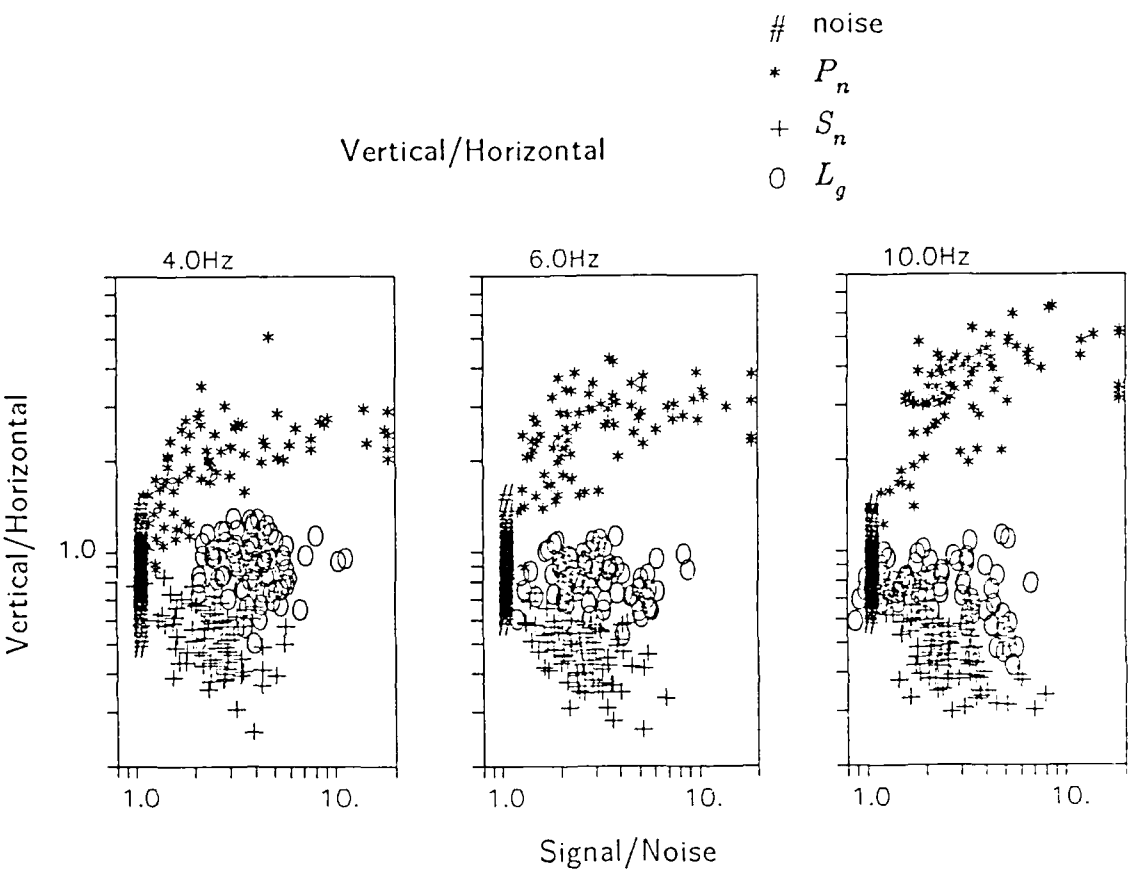

Figure 6. Vertical-to-horizontal amplitude ratios of the regional phases as well as noise. The values plot at 1.0 when all three components have the same amplitude. There is a distinct separation between these phases using this attribute. *P*-waves have larger vertical motions, S_n waves have larger horizontal motions and L_g tends to have about equal horizontals and vertical, similar to the noise. The ratios for both P_n and S_n tend to increase with signal-to-noise level.

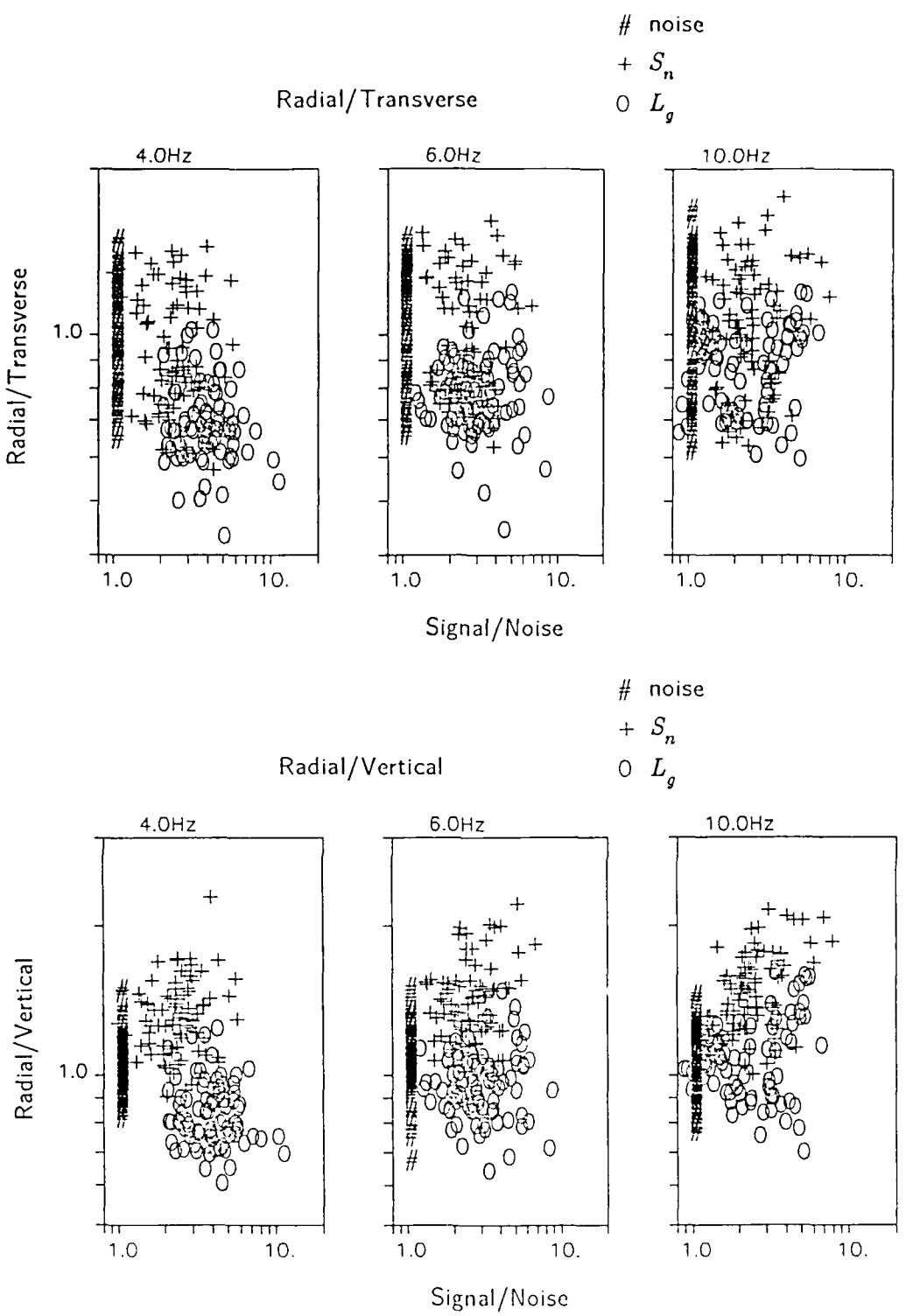

Figure 7. Ratios of radial, transverse and vertical components for S_n, L_g and noise plotted as a function of the signal-to-noise level in three bands. The upper diagrams show that S_n has about equal radial and transverse motions at all frequencies, much like the noise. L_g waves have smaller radial motions than transverse, particularly at the lower frequencies. The lower diagrams show that S_n waves have smaller verticals than radials at all frequencies and that the radial motions of L_g are smaller than the verticals at lower frequencies.

than the ambient noise, although there is a considerable scatter. The average planarity of S_n is similar to that of L_g at 4 Hz, and higher than L_g at 10 Hz. *Figure 7* suggests that the orientations of the planes of motion are different for S_n and L_g. The S_n motions are dominantly horizontal, with radial amplitudes equal to transverse on the average. L_g motions are dominant in a plane perpendicular to the source direction, with transverse and verticals about equal and radials smaller. *Figure 8* shows one parameter which characterizes the orientation of the plane of dominant motion for S_n and L_g. This parameter is is the incidence angle, measured from vertical, of the eigenvector with the smallest eigenvalue. This eigenvector is the perpendicular to the dominant plane of motion. An incidence angle close to 0° indicates the plane of motion is dominantly horizontal. A value close to 90° means the plane of motion is nearly vertical. There is a good separation between S_n and L_g using this one parameter. It reflects what was seen in *Figure 7*, namely that the S_n motions are dominantly horizontal at all frequencies and that the L_g plane of motion at lower frequencies tends to be closer to vertical. At 10 Hz, many of the L_g waves begin to behave more like S_n and so there is an overlap in the two populations.

3.1.4. Conclusions

Particle-motion characteristics of 93 regional events recorded at the NORESS array have been analyzed. The polarization attributes were extracted from time windows picked interactively by an analyst. These extraction windows were carefully selected to include phases associated with the same event and with signal-to-noise ratios greater than 1.0. The events were selected to have a range of signal-to-noise levels in order to determine the effects of noise. The use of all of the three-component elements in the NORESS array in this analysis gave better polarization estimates than could be obtained using a single three-component station.

The analysis results suggest the following conclusions:

(1) S_n signals have a distinctive polarization allowing them to be distinguished from the other regional phases in most cases. The radial and transverse components of S_n tend to be about equal and greater than the vertical components.

(2) L_g waves have a distinct polarization (at lower frequencies) by which they can be distinguished from the other phases in most cases. L_g motions tend to have smaller radial components and about equal vertical and transverse motions. The polarization of L_g at higher frequencies tends to be less reliable.

(3) P_n and S_n phases have well-defined polarization up to at least 13 Hz (the upper frequency used in this analysis) whenever there is signal above noise at these frequencies.

(4) The quality of polarization information deteriorates with increasing noise level. However, when multiple three-component elements are used in an array (four in this analysis), then the polarization attributes are informative for signal-to-noise levels down to 1.0.

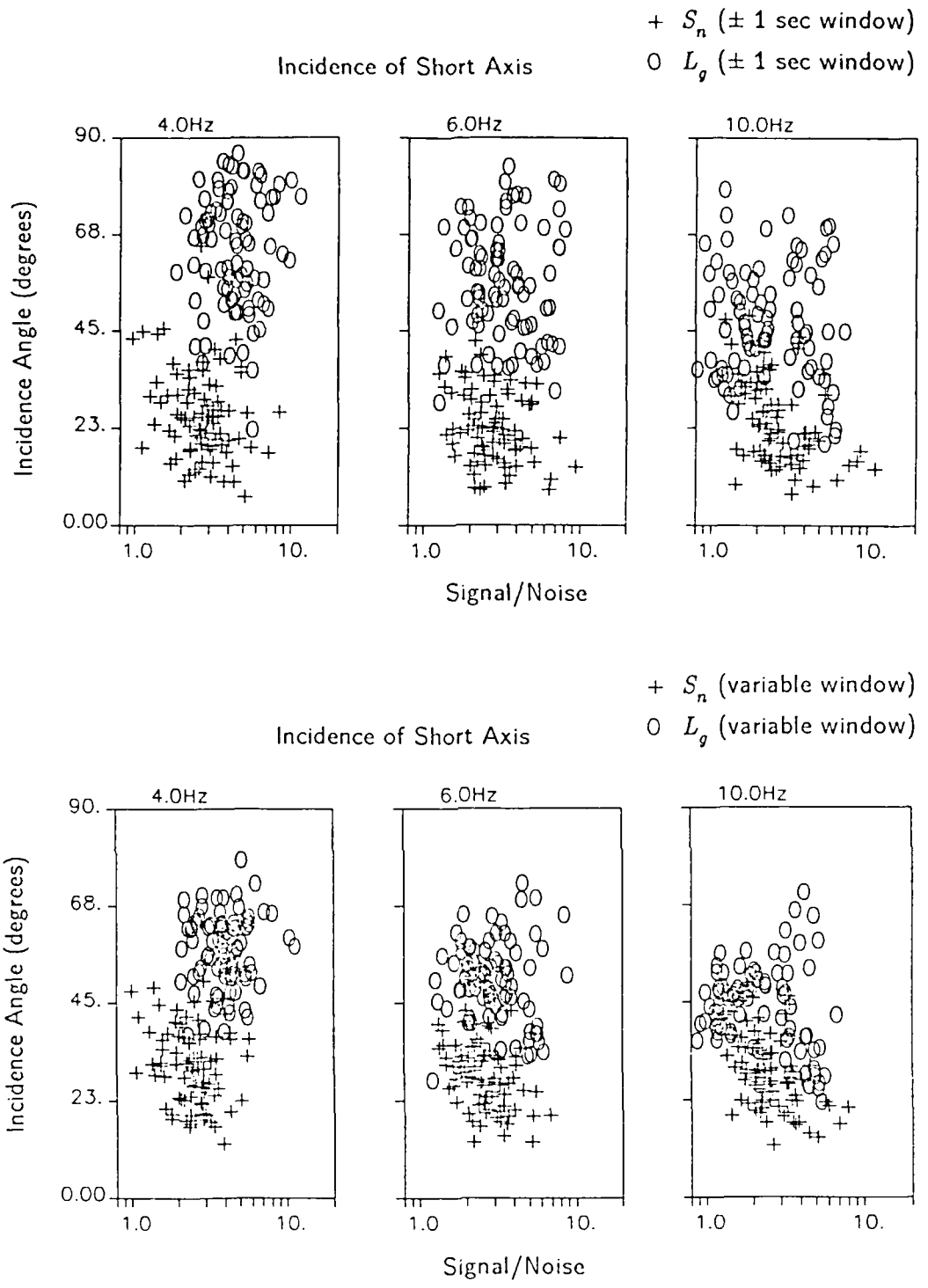

Figure 8. The incidence angle of the short axis of the polarization ellipsoid describes the orientation of the plane of dominant motion as measured from vertical. These results show that S_n motions are dominantly in a plane close to horizontal and L_g motions are dominantly in a plane closer to vertical. This attribute allows a good degree of separation between these two phases.

(5) At the NORESS array, azimuths from P_n motions can be estimated with a standard deviation of about 10-12°. L_g azimuths can be estimated from the minimum horizontal motions and are not as accurate as P_n azimuths.

The analysis method used in this study can be implemented in either interactive workstation or automatic on-line modes. The procedure works in the time domain and is very fast, so polarization characteristics may be computed continuously. This means the choice of time windows and frequency intervals for extracting polarization information can be made on the basis of the attributes themselves. This is important because the quality of the extracted information depends on situating the time windows on the purest particle motions, which are generally short duration. In an interactive mode, the analyst simply examines time histories of polarization attributes in several frequency bands and selects the bands and windows with the best motions. In automatic mode, the amplitudes in several bands can be compared with the ambient noise levels in these bands. The bands are then chosen for which the signal-to-noise levels are above some threshold. The covariance matrices for the selected bands may be normalized and averaged together to give a single wide-band covariance estimate as a function of time. The P-wave windows can be chosen on the basis of the amplitude, rectilinearity and large vertical-to-horizontal ratio. The S_n and L_g windows can be selected on the basis of the amplitude, small vertical-to-horizontal ratio and the orientation of the dominant plane of particle motion. In identifying phase types, the attributes extracted for a phase can be compared with typical values obtained from a controlled study such as this one. During analysis of the 93 events in this dataset, several cases of overlapping arrivals from different events were encountered. For example, P-waves from one event may have been superposed on S_n or L_g waves from another event. Plots of the attributes as a function of time and frequency were very useful for identifying and separating the overlapping phases.

Andy Jurkevics

REFERENCES

Flinn, E. A., 1965. "Signal Analysis Using Rectilinearity and Direction of Particle Motion," *Proc. IEEE*, Vol. 53, No. 12, p.1874.

Jurkevics, A., 1986a. "Polarization Analysis Using an Array of Three-Component Sensors: Part I -- Theory," *SAIC Technical Report for July-September 1986, Center for Seismic Studies Technical Report*, C86-07, November 1986.

Jurkevics, A., 1986b. "Polarization Analysis Using an Array of Three-Component Sensors: Part II -- Application to NORESS," "SAIC Technical Report for July-September 1986, Center for Seismic Studies Technical Report, C86-07, November 1986.

Kvaerna, T. and Doornbos, D. J., 1986a. "An Integrated Approach to Slowness Analysis with Arrays and Three-Component Stations," *Semiannual Technical Summary, October 1985 - March 1986, NORSAR Scientific Report*, 2-85/86.

Kvaerna, T. and Doornbos, D. J., 1986b. "On Three-Component Analysis of Secondary Phases," *Semiannual Technical Summary, April-September 1986, NORSAR Scientific Report*, 1-86/87.

Magotra, N., Ahmed, N., and Chael, E., 1987. "Seismic Event Detection and Source Location Using Single-Station (Three-Component) Data," *Bull. Seism. Soc. Am.*, Vol. 77, No. 3, pp. 958.

Samson, J. C. and Olson, J. V., 1980. "Some Comments on the Descriptions of the Polarization States of Waves," *Geophys. Jour R.A.S.*, Vol. 61, No. 1, p.115.

Samson, J. C. and Olson, J. V., 1981. "Data-adaptive Polarization Filters for Multichannel Geophysical Data," *Geophysics*, Vol. 46, No. 10, p. 1423.

Smart, E., 1977. "A Three-Component Single-Station Maximum-Likelihood Surface Wave Processor," *SDAC-TR-77-14, Teledyne Geotech*, Alexandria, VA.

Smart, E. and Sproules, H., 1981. "Regional Phase Processors," *SDAC-TR-81-1, Teledyne Geotech*, Alexandria, VA.

Suteau-Henson, A., Sutton, G. H., and Carter, J. A., 1985. "Polarization State Analysis of Three-Component and Array Seismograms," *Roundout Associates Incorporated.*

von Seggern, D. and Marshall, M., 1982. "Definition of Seismic Signal Parameters by Particle-Motion Processing," *SDAC-TR-81-19, Teledyne Geotech*, Alexandria, VA.

APPENDIX I

EVENTS USED IN THE ANALYSIS

A total of 93 regional events recorded at the NORESS array are contained in this dataset. Of these events, 41 are earthquakes, 40 are mining explosions and the remainder are unknown source types. All of the events occurred within a distance of 20° of NORESS and had m_b magnitudes of less than 5.0. A majority of the events fall into three clusters -- a series of mining explosions and presumed earthquakes near the south coast of Norway southwest of the array and at a distance of about 3.5° - 4.0°, a series of mining explosions to the east at a distance of about 8.0° - 9.0°, and a series of earthquakes west of the array at a distance of about 3.0° - 5.0°. The locations, magnitudes and source types were obtained from local bulletins. *Figure 1* of the technical note "Spectral Study of Regional Earthquakes and Chemical Explosions Recorded at the NORESS Array" in this report contains a map of the Scandinavia region showing these events.

Yr/DoY	Mo-Dy-Time	Lat (deg)	Lon (deg)	Dist (deg)	Azim (deg)	m_b	Type*
85/213	08-01 11:17:35	45.82	26.65	17.35	142.46	4.7	E
85/298	10-25 12:03:47	59.30	28.10	8.38	92.62	2.3	X
85/300	10-27 04:36:43	61.12	4.92	3.24	279.62	2.8	E
85/312	11-08 14:18:54	58.34	6.43	3.53	229.41	2.4	X
85/313	11-09 14:42:46	57.80	7.20	3.68	218.91	2.1	X
85/313	11-09 18:20:48	62.00	7.70	2.23	306.08	2.0	?
85/317	11-13 16:32:10	58.30	6.40	3.57	229.13	1.8	X
85/317	11-13 12:07:48	59.30	28.10	8.38	92.62	2.3	X
85/324	11-20 22:10:44	57.61	5.67	4.34	226.41	2.3	u
85/324	11-20 22:24:38	57.66	5.72	4.28	226.58	2.2	u
85/324	11-20 22:57:10	57.64	5.62	4.33	226.94	2.3	u
85/324	11-20 23:10:47	57.66	5.35	4.42	228.51	2.3	u
85/324	11-20 23:17:28	57.69	5.49	4.34	228.06	2.3	u
85/324	11-20 23:23:10	57.50	5.62	4.44	225.73	2.2	u
85/324	11-20 23:28:23	57.58	5.49	4.42	227.09	2.2	u
85/325	11-21 14:18:13	59.80	8.20	1.90	241.88	1.4	x
85/325	11-21 14:48:07	54.80	6.50	6.52	206.51	2.8	x
85/325	11-21 09:16:30	58.37	12.36	2.41	169.70	-	?
85/327	11-23 13:06:18	59.50	25.00	6.81	94.59	2.1	X
85/331	11-27 04:53:32	59.73	5.71	3.06	253.31	2.8	E
85/344	12-10 12:05:39	59.40	28.50	8.54	91.57	2.2	X
85/357	12-23 02:35:08	60.38	1.90	4.75	269.87	2.3	E
85/358	12-24 12:37:57	59.80	22.50	5.51	95.02	1.9	?
85/359	12-25 13:19:01	58.70	26.00	7.55	99.30	2.6	?
85/361	12-27 12:16:08	59.40	28.50	8.54	91.57	2.4	X
85/365	12-31 06:57:17	73.31	6.62	12.71	353.57	4.8	E

Yr/DoY	Mo-Dy-Time	Lat (deg)	Lon (deg)	Dist (deg)	Azim (deg)	m_b	Type*
86/003	01-03 14:58:41	61.90	30.60	9.19	74.46	2.5	X
86/007	01-07 14:14:28	58.34	6.43	3.53	229.41	2.2	X
86/009	01-09 09:18:43	54.70	19.50	7.37	141.43	2.7	?
86/017	01-17 14:11:01	58.34	6.43	3.53	229.41	2.3	X
86/019	01-19 04:59:22	65.00	12.13	4.27	3.35	3.0	E
86/020	01-20 23:38:28	50.19	12.37	10.56	177.10	4.9	?
86/021	01-21 08:55:40	55.30	13.60	5.55	167.78	2.5	?
86/031	01-31 12:10:15	59.30	28.10	8.38	92.62	3.2	X
86/035	02-04 12:14:59	59.50	26.50	7.54	92.90	2.8	X
86/035	02-04 12:58:59	59.40	24.60	6.64	95.91	2.5	X
86/035	02-04 14:22:57	59.30	24.40	6.57	97.00	2.6	X
86/036	02-05 17:53:16	62.81	4.86	3.77	306.15	4.7	E
86/037	02-06 16:29:55	67.10	20.60	7.49	28.05	2.7	X
86/037	02-06 12:22:04	59.30	28.10	8.38	92.62	2.7	X
86/038	02-07 14:06:11	***	***	3.80	210.00	1.6	?
86/038	02-07 11:00:01	64.70	30.70	9.58	57.40	3.1	X
86/038	02-07 14:05:22	***	***	3.80	210.33	2.8	?
86/041	02-10 12:41:46	59.40	28.50	8.54	91.57	2.5	X
86/045	02-14 14:13:19	58.34	6.43	3.53	229.41	2.4	X
86/045	02-14 17:54:04	58.34	6.43	3.53	229.41	2.3	X
86/045	02-14 12:10:21	59.40	28.50	8.54	91.57	2.7	X
86/045	02-14 16:44:08	67.10	20.60	7.49	28.05	2.6	X
86/049	02-18 10:46:16	59.30	27.20	7.94	93.57	2.6	X
86/049	02-18 12:45:50	64.70	30.70	9.58	57.40	2.6	X
86/057	02-26 02:11:44	62.76	5.29	3.58	307.05	2.5	E
86/062	03-03 07:26:06	43.70	31.40	20.76	136.13	4.4	E
86/064	03-05 14:16:31	66.30	21.70	7.15	34.70	-	?
86/064	03-05 12:13:19	59.50	26.50	7.54	92.90	2.6	X
86/064	03-05 13:02:05	60.63	2.58	4.38	272.47	2.1	E
86/067	03-08 16:21:17	61.67	2.58	4.41	286.06	2.4	E
86/069	03-10 12:02:09	59.30	28.10	8.38	92.62	2.6	X
86/069	03-10 04:20:04	62.81	4.91	3.75	306.32	2.5	E
86/070	03-11 12:02:28	59.30	28.10	8.38	92.62	2.6	X
86/071	03-12 11:07:21	59.50	26.50	7.54	92.90	2.5	X
86/071	03-12 12:01:38	59.40	28.50	8.54	91.57	2.5	X
86/078	03-19 12:06:40	59.40	28.50	8.54	91.57	2.6	X
86/089	03-30 03:22:37	61.66	4.53	3.50	288.29	2.2	E
86/091	04-01 09:56:53	56.42	12.10	4.33	175.89	3.6	E
86/094	04-04 22:42:30	71.08	8.35	10.42	354.27	4.6	E
86/097	04-07 00:34:37	61.84	4.88	3.38	291.88	2.3	E
86/108	04-18 00:44:13	59.22	1.42	5.28	257.72	2.4	E
86/114	04-24 09:53:12	***	***	1.50	200.00	-	?
86/133	05-13 09:23:44	***	***	4.30	115.00	4.5	?
86/154	06-03 14:30:04	61.46	4.08	3.67	284.54	2.8	E
86/155	06-04 09:06:31	61.50	30.40	9.11	77.00	3.3	X
86/163	06-12 09:30:55	61.50	30.40	9.11	77.00	3.1	X

Yr/DoY	Mo-Dy-Time	Lat (deg)	Lon (deg)	Dist (deg)	Azim (deg)	m_b	Type*
86/166	06-15 15:01:07	61.67	3.85	3.82	287.44	3.0	E
86/168	06-17 12:12:07	59.40	28.50	8.54	91.57	2.6	X
86/169	06-18 11:05:08	59.40	28.50	8.54	91.57	2.5	X
86/170	06-19 03:55:08	59.31	6.54	2.88	242.39	2.4	X
86/171	06-20 22:07:53	61.47	3.92	3.75	284.53	2.0	?
86/177	06-26 04:06:21	61.88	5.10	3.29	293.05	2.4	E
86/178	06-27 03:49:46	59.28	6.76	2.80	240.66	2.5	E
86/185	07-04 11:13:27	59.30	28.10	8.38	92.62	2.6	X
86/195	07-14 13:50:32	58.35	13.82	2.65	153.21	4.0	E
86/195	07-14 14:30:27	61.10	29.90	8.90	79.67	2.9	X
86/195	07-14 15:02:19	69.30	34.40	12.76	38.43	2.9	X
86/222	08-10 05:01:04	59.99	5.34	3.15	258.96	1.7	E
86/228	08-16 04:24:36	62.82	4.98	3.73	306.70	2.5	E
86/244	09-01 22:11:26	60.82	2.93	4.20	274.85	3.5	E
86/273	09-30 20:02:47	60.79	4.23	3.57	273.99	2.4	E
86/283	10-10 19:56:31	61.97	2.33	4.58	289.58	2.3	E
86/299	10-26 11:45:06	61.46	3.29	4.05	283.83	2.6	E
86/299	10-26 11:57:03	61.72	3.27	4.10	287.43	2.6	E
86/302	10-29 21:05:01	60.81	3.04	4.15	274.68	2.4	E
86/327	11-23 03:30:32	73.74	9.08	13.03	356.94	4.7	E
86/346	12-12 16:33:30	72.96	4.80	12.49	350.85	4.7	E

*** location based on frequency-wavenumber analysis only

* X = explosion, x = presumed explosion
E = earthquake, e = presumed earthquake
? = unknown source type
u = presumed underwater explosion

3.2. SPECTRAL STUDY OF REGIONAL EARTHQUAKES AND CHEMICAL EXPLOSIONS RECORDED AT THE NORESS ARRAY

3.2.1. Introduction

The success of a Comprehensive or Low-Yield Test Ban Treaty which includes the provision for seismic monitoring stations within the Soviet Union will depend on our ability to distinguish low-yield or decoupled nuclear explosions from both chemical mining explosions and small shallow earthquakes at regional distances. This is a subset of the general discrimination problem, complicated by the fact that regional seismic phases are of high frequency and thus are affected by small scale changes in the path.

The regional discrimination problem has been approached from both "model-based" and "case-based" viewpoints by several researchers in the past with limited success, although the "case-based" approach to event identification has not yet been thoroughly explored. Examples of the model-based approach are the use of conventional discriminants such as those described by Pomeroy *et al.* (1982). To this day, no single model-based discriminant has been found which works in all areas. For example, we found that many chemical explosions in Scandinavia and the western Soviet Union generate seismic waves which are higher in frequency than earthquakes of similar magnitude. This is exactly the opposite of what has been found in California by Aviles and Lee (1986). Here is where the case-based approach lends itself to application, since the discriminant applies only to the case under study.

The "case-based" approach relies on knowledge acquired from the observation of many events from a particular region. The subsequent identification of a new event is made on the basis of repeatable waveform and spectral characteristics. In many cases these characteristics are imposed by the propagation path and are unrelated to any known physical source model. As a result, one problem with the case-based approach is that it is empirical and may not lead to a better physical understanding of the problem. A solution to the discrimination problem may be a hybrid of both approaches, combining the pattern recognition ability of the human analyst with parameters based on physical models for each source type. This is the approach we take in this study.

The goal of this project was to examine the signal characteristics of chemical explosions and earthquakes recorded by the NORESS array in order to develop a methodology for conducting seismic event characterization on an automated or semiautomated basis. The philosophy which has guided the study is based on a three-step approach to the problem.

The first step is to select a database of regional events which have already been identified by local seismologists (in Scandinavia) as earthquakes or chemical explosions, and to include in this database a small number of unidentified events.

The second step is to extract a large number of signal parameters from the dataset to see if there are any observable differences between the explosions and the earthquakes. These signal parameters range from those commonly used in

model-based studies, such as the ratio of L_g to P_n amplitude, to more abstract signal parameters less directly related to the physics of the situation than to the experience gained in looking at a large suite of events. Such a parameter is spectral complexity, which we found to be a distinguishing characteristic of explosions in this region. This second step is highly iterative, that is, a process is applied to the dataset and subsequent visual interpretation by the researcher is necessary to identify characteristic features of the signal.

The third step is to quantify the identifying characteristics and apply them once again to the entire dataset. Final interpretation may rest on an examination of all the parameters in a multidimensional analysis. This process will point to outliers in the results, and these events may then be re-examined to gain insight into the nature of the failure of the method.

To accomplish this goal, a spectral analysis was made of P_n, S_n, and L_g waves from 95 events recorded at NORESS during the period 1985-1987. Magnitudes of the events ranged from 1.4 to 4.7, and the epicentral distances were less than 1000 km for most events. Magnitudes were obtained in most cases from local bulletins. These are usually based on coda duration. Events chosen from the PDE listings have magnitudes reported as m_b. Thus, there is some inherent mixing of magnitude scales. The data set includes earthquakes both on land and offshore, and chemical explosions from mines located in southern Norway, Sweden, and the western Soviet Union. In several cases, a number of events were recorded from the same mine or earthquake source region. Repeatable waveform characteristics could be observed in such cases. However, for some mines, clear differences were observed in the spectra of different events. Considering that the path effect for these events is very nearly the same if not equal, this implies that source differences can be observed with regional data.

Regional phases were characterized by a variety of spectral parameters which measure high frequency content, spectral bandwidth, spectral ratios, and spectral complexity. Preliminary results indicate that the P_n/S_n and P_n/L_g ratios provide some discrimination capability between earthquakes and explosions recorded in this region, although there is significant overlap between the two populations. Mine blasts are best identified on the basis of their monochromatic frequency content, or their spectral complexity as measured by the variance of the cepstrum of P_n and S_n. This complexity is assumed to occur due to multiple delayed firing of the explosion sources. When combined with the amplitude ratios, the cepstral variance successfully separated approximately 90% of the explosions and earthquakes. Anomalous events can usually be identified upon reanalysis, or explained by low signal-to-noise ratio (SNR).

Single-array estimates of Q and corner frequency were made for all phases by a linearized least-squares inversion. Several models with varying falloff and frequency dependence were tested. The best fit to all the data was obtained for an ω^{-2} model with an $f^{0.5}$ frequency dependence. The inversion for corner frequency as a parameter which is independent of Q appeared to make the regression unstable in cases where the spectra are flat, or for events with low SNR. The variance in Q estimates was generally higher for the explosions than for the earthquakes due to the complexity of their spectra. Consequently, the regression results were generally unsatisfactory due to the inadequacy of the simple asymptotic source model in representing complex explosion spectra. Q values using only cases which resulted

in stable convergence cluster at a value of about 500 for all phases. There are a number of events for which Q estimates are considerably higher. Q estimates of 1000 for P_n, S_n and L_g were not uncommon. These values are consistently higher than those found in a similar attenuation study by Sereno *et al.* (1987) using a different parameterization which inverts for the frequency dependence and seismic moment. The frequency dependence of Q found in both studies is consistent.

A detailed discussion of the spectral and polarization analyses of these events will appear in a separate report to be issued this summer.

3.2.2. The Data Set and Data Processing

Figure 1 shows an epicenter map of the events analyzed in this report. The data set includes 95 events recorded by the 25-element NORESS array in southern Norway. Events with local magnitudes of about 1.5 or greater were selected from the two-year period 1985-1987. Selection of the events was made by examining the local network bulletins of the Bergen Seismological Observatory and the University of Helsinki Institute of Seismology. Additional events were selected from the U. S. Geological Survey's Preliminary Determination of Epicenters (PDE). A listing of all events is found in Table I. These events are currently available on disk as a research database at the Center for Seismic Studies. The locations listed in Table I are taken either from the local bulletins or from the PDE listing. Chemical explosions were recorded from mines in Sweden, Southern Norway and the western Soviet Union. In several cases a number of events were recorded from the same mine (eq. TI, E7, E8). Earthquakes were located in the Shetland Islands, the western coast of Norway, and several isolated events in the Norwegian Sea, Greenland Sea and Europe. Events 10-16 and event 74 have been tentatively identified as underwater explosions off the southwest coast of Norway. They occur in a seismically inactive region within a single 2-hour period.

For each event, time windows surrounding P_n, S_n, and L_g waves, as well as the noise, were chosen interactively on a Sun Microsystems 3/50 workstation. The onset time and length of the window were picked from seismograms filtered in two octave bands (3-6 and 6-12 Hz) on the basis of the visible duration of the phase. This procedure minimizes contamination of the desired phase by subsequent phases, as sometimes occurs when phase velocity windows are used. The average spectrum for each phase was computed as the mean of all the recording elements, in the manner of a periodogram (Oppenheim and Schafer, 1975). This procedure reduces the spectral variance without the reduction of high-frequency amplitudes which occurs during beamforming. Peak frequencies of P_n, S_n and L_g were picked from the smoothed spectra in a frequency band with a SNR > 4. This constraint was relaxed for spectra with a total bandwidth of less than 5 Hz. Spectral ratios of P_n/S_n and P_n/L_g were computed by averaging the spectral amplitudes in the optimum signal band.

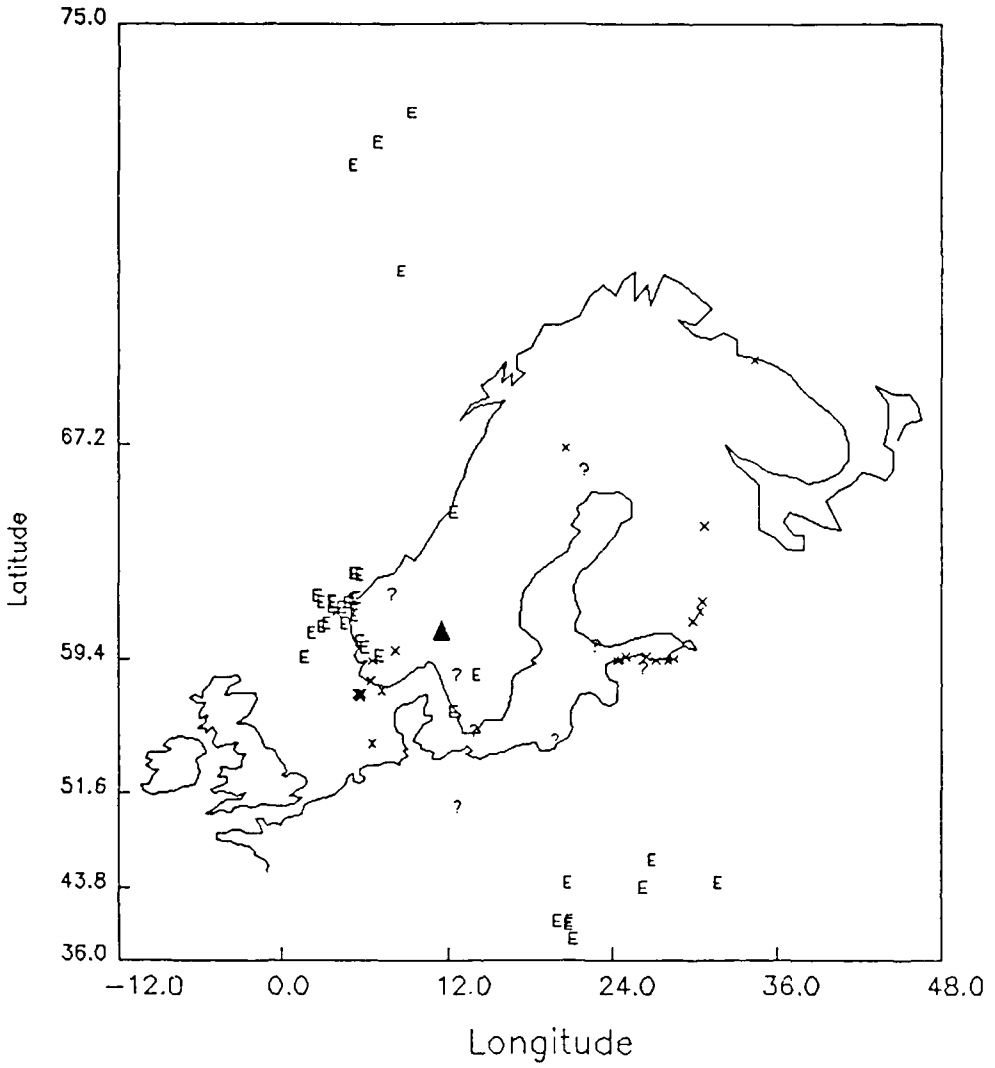

Figure 1. Epicenter map of the events used in this study. The triangle indicates the site of the NORESS array. An "E" designates an earthquake, an "X" an explosion, and a "?" designates an unidentified event.

Table I

No.	Yr/DoY	Mo-Dy Time	Lat (deg)	Lon (deg)	Dist (deg)	Azim (deg)	m_b	Type
1	85/106	12-99 12:46:45	39.79	20.56	21.70	348.00	-	E
2	85/213	08-01 11:17:35	45.82	26.65	17.35	142.46	4.7	E
3	85/298	10-25 12:03:47	59.30	28.10	8.38	92.62	2.3	X-E7
4	85/300	10-27 04:36:43	61.12	4.92	3.24	279.62	2.8	E
5	85/312	11-08 14:18:54	58.34	6.43	3.53	229.41	2.4	X-TI
6	85/313	11-09 14:42:46	57.80	7.20	3.68	218.91	2.1	?
7	85/313	11-09 18:20:48	62.00	7.70	2.23	306.08	2.0	?
8	85/317	11-13 16:32:10	58.30	6.40	3.57	229.13	1.8	X-TI
9	85/317	11-13 12:07:48	59.30	28.10	8.38	92.62	2.3	X-E7
10	85/324	11-20 22:10:44	57.61	5.67	4.34	226.41	2.3	u
11	85/324	11-20 22:24:38	57.66	5.72	4.28	226.58	2.2	u
12	85/324	11-20 22:57:10	57.64	5.62	4.33	226.94	2.3	u
13	85/324	11-20 23:10:47	57.66	5.35	4.42	228.51	2.3	u
14	85/324	11-20 23:17:28	57.69	5.49	4.34	228.06	2.3	u
15	85/324	11-20 23:23:10	57.50	5.62	4.44	225.73	2.2	u
16	85/324	11-20 23:28:23	57.58	5.49	4.42	227.09	2.2	u
17	85/325	11-21 14:18:13	59.80	8.20	1.90	241.88	1.4	X
18	85/325	11-21 14:48:07	54.80	6.50	6.52	206.51	2.8	X
19	85/325	11-21 09:16:30	58.37	12.36	2.41	169.70	-	?
20	85/327	11-23 13:06:18	59.50	25.00	6.81	94.59	2.1	X-E3
21	85/331	11-27 04:53:32	59.73	5.71	3.06	253.31	2.8	E
22	85/344	12-10 12:05:39	59.40	28.50	8.54	91.57	2.2	X-E8
23	85/357	12-23 02:35:08	60.38	1.90	4.75	269.87	2.3	E
24	85/358	12-24 12:37:57	59.80	22.50	5.51	95.02	1.9	?
25	85/359	12-25 13:19:01	58.70	26.00	7.55	99.30	2.6	X
26	85/361	12-27 12:16:08	59.40	28.50	8.54	91.57	2.4	X-E8
27	85/365	12-31 06:57:17	73.31	6.62	12.71	353.57	4.8	E
28	86/003	01-03 14:58:41	61.90	30.60	9.19	74.46	2.5	X-V7
29	86/007	01-07 14:14:28	58.34	6.43	3.53	229.41	2.2	X-TI
30	86/009	01-09 09:18:43	54.70	19.50	7.37	141.43	2.7	?
31	86/017	01-17 14:11:01	58.34	6.43	3.53	229.41	2.3	X-TI
32	86/019	01-19 04:59:22	65.00	12.13	4.27	3.35	3.0	E
33	86/020	01-20 23:38:28	50.19	12.37	10.56	177.10	4.9	E
34	86/021	01-21 08:55:40	55.30	13.60	5.55	167.78	2.5	?
35	86/031	01-31 12:10:15	59.30	28.10	8.38	92.62	3.2	X-E7
36	86/035	02-04 12:14:59	59.50	26.50	7.54	92.90	2.8	X-E9
37	86/035	02-04 12:58:59	59.40	24.60	6.64	95.91	2.5	X-E2
38	86/035	02-04 14:22:57	59.30	24.40	6.57	97.00	2.6	X-E1
39	86/036	02-05 17:53:16	62.81	4.86	3.77	306.15	4.7	E
40	86/037	02-06 16:29:55	67.10	20.60	7.49	28.05	2.7	X-R1
41	86/037	02-06 12:22:04	59.30	28.10	8.38	92.62	2.7	X-E7
42	86/038	02-07 11:00:01	64.70	30.70	9.58	57.40	3.1	X-V1
43	86/041	02-10 12:41:46	59.40	28.50	8.54	91.57	2.5	X -E8
44	86/045	02-14 14:13:19	58.34	6.43	3.53	229.41	2.4	X-TI
45	86/045	02-14 17:54:04	58.34	6.43	3.53	229.41	2.3	X-TI
46	86/045	02-14 12:10:21	59.40	28.50	8.54	91.57	2.7	X-E8

X = explosion
E = earthquake
? = unknown source type
u = presumed underwater explosion

Table I - (Continued)

No.	Yr/DoY	Mo-Dy Time	Lat (deg)	Lon (deg)	Dist (deg)	Azim (deg)	m_b	Type
47	86/045	02-14 16:44:08	67.10	20.60	7.49	28.05	2.6	X-R1
48	86/049	02-18 10:46:16	59.30	27.20	7.94	93.57	2.6	X-E4
49	86/049	02-18 12:45:50	64.70	30.70	9.58	57.40	2.6	X-V1
50	86/057	02-26 02:11:44	62.76	5.29	3.58	307.05	2.5	E
51	86/062	03-03 07:26:06	43.70	31.40	20.76	136.13	4.4	E
52	86/064	03-05 14:16:31	66.30	21.70	7.15	34.70	-	?
53	86/064	03-05 12:13:19	59.50	26.50	7.54	92.90	2.6	X-E9
54	86/064	03-05 13:02:05	60.63	2.58	4.38	272.47	2.1	E
55	86/067	03-08 16:21:17	61.67	2.58	4.41	286.06	2.4	E
56	86/069	03-10 12:02:09	59.30	28.10	8.38	92.62	2.6	X-E7
57	86/069	03-10 04:20:04	62.81	4.91	3.75	306.32	2.5	E
58	86/070	03-11 12:02:28	59.30	28.10	8.38	92.62	2.6	X-E7
59	86/071	03-12 11:07:21	59.50	26.50	7.54	92.90	2.5	X-E9
60	86/071	03-12 12:01:38	59.40	28.50	8.54	91.57	2.5	X-E8
61	86/078	03-19 12:06:40	59.40	28.50	8.54	91.57	2.6	X-E8
62	86/089	03-30 03:22:37	61.66	4.53	3.50	288.29	2.2	E
63	86/091	04-01 09:56:53	56.42	12.10	4.33	175.89	3.6	E
64	86/094	04-04 22:42:30	71.08	8.35	10.42	354.27	4.6	E
65	86/097	04-07 00:34:37	61.84	4.88	3.38	291.88	2.3	E
66	86/108	04-18 00:44:13	59.22	1.42	5.28	257.72	2.4	E
67	86/154	06-03 14:30:04	61.46	4.08	3.67	284.54	2.8	E
68	86/155	06-04 09:06:31	61.50	30.40	9.11	77.00	3.3	X-V3
69	86/163	06-12 09:30:55	61.50	30.40	9.11	77.00	3.1	X-V3
70	86/166	06-15 15:01:07	61.67	3.85	3.82	287.44	3.0	E
71	86/168	06-17 12:12:07	59.40	28.50	8.54	91.57	2.6	X-E8
72	86/169	06-18 11:05:08	59.40	28.50	8.54	91.57	2.5	X-E8
73	86/170	06-19 03:55:08	59.31	6.54	2.88	242.39	2.4	X-BLA
74	86/171	06-20 22:07:53	61.47	3.92	3.75	284.53	2.0	u
75	86/177	06-26 04:06:21	61.88	5.10	3.29	293.05	2.4	E
76	86/178	06-27 03:49:46	59.28	6.76	2.80	240.66	2.5	E
77	86/185	07-04 11:13:27	59.30	28.10	8.38	92.62	2.6	X-E7
78	86/189	12-99 16:15:04	37.80	20.87	23.70	348.60	-	E
79	86/195	07-14 13:50:32	58.35	13.82	2.65	153.21	4.0	E
80	86/195	07-14 14:30:27	61.10	29.90	8.90	79.67	2.9	X-V8
81	86/195	07-14 15:02:19	69.30	34.40	12.76	38.43	2.9	X-K9
82	86/222	08-10 05:01:04	59.99	5.34	3.15	258.96	1.7	E
83	86/228	08-16 04:24:36	62.82	4.98	3.73	306.70	2.5	E
84	86/244	09-01 22:11:26	60.82	2.93	4.20	274.85	3.5	E
85	86/273	09-30 20:02:47	60.79	4.23	3.57	273.99	2.4	E
86	86/283	10-10 19:56:31	61.97	2.33	4.58	289.58	2.3	E
87	86/299	10-26 11:45:06	61.46	3.29	4.05	283.83	2.6	E
88	86/299	10-26 11:57:03	61.72	3.27	4.10	287.43	2.6	E
89	86/327	11-23 03:30:32	73.74	9.08	13.03	356.94	4.7	E
90	86/342	12-99 14:44:27	43.29	25.99	19.50	348.00	-	E
91	86/346	12-12 16:33:30	72.96	4.80	12.49	350.85	4.7	E
92	86/351	12-99 21:18:32	39.81	19.72	21.60	349.00	-	E
93	86/352	12-99 17:16:16	43.28	26.01	19.50	338.50	-	E
94	87/067	12-99 17:42:21	39.48	20.52	22.00	348.20	-	E
95	87/109	12-99 03:55:06	43.69	20.44	17.90	345.70	-	E

X = explosion
E = earthquake
? = unknown source type
u = presumed underwater explosion

The third moment of frequency (TMF) was computed using the equation (Weichert, 1971)

$$TMF = \frac{\int_{2}^{20} Hz\ f^3\ V(f)\ df}{\int_{2}^{20} Hz\ V(f)\ df} \qquad (1)$$

to obtain a measure of the relative high-frequency content of the signal.

As a measure of spectral complexity, the cepstrum of each phase was computed for all events. A zero-phase deconvolution of the noise was made by subtracting the log-amplitude of the noise. The deconvolved log-spectra were detrended and demeaned to remove the differential effects of attenuation and high-frequency falloff. The degree of the spectral complexity was measured by the variance of the cepstrum in a quefrency range from 0.1 to 0.5 sec. This range was chosen to exclude signals below 2 Hz which are generally well below the level of microseismic noise in this region.

The data in the optimum signal band were then fit by a simple asymptotic source model of the form

$$V(f) = I_V(f)\ \frac{f_0\ f}{1 + (f/f_c)^N}\ e^{-\pi f \Delta / Q_o f^{\eta} U} \qquad (2)$$

where f is the frequency in Hz, f_0 is a scaling constant, $I_V(f)$ is the velocity response of the seismometer and recorder, f_c is the source corner frequency, N is a constant which controls the high frequency decay of the source, Δ is the epicentral distance, Q_o is the value of Q at 1 Hz, η is a constant which controls the frequency dependence of Q, and U is the phase velocity. Estimated parameters in the regression were Q_0, f_c and f_0. The regression was repeated for values of N = -2,-3 and η = 0.0, 0.2, 0.5, 0.7.

3.2.3. Propagation Characteristics

There were five groups of events for which all three phases, and four or more events were recorded from the same region. These groups contain repeated events identified as blasts from two mines in the western Soviet Union (E7 and E8), a molybdenum mine in southern Norway (Titania), earthquakes to the northwest of the array, and a sequence of probable underwater explosions off the southwestern coast of Norway.

Repeatable waveform characteristics are often diagnostic of events from a particular location. These include monochromatic P_n, S_n, and L_g waves from some mines. An example of this is shown in *Figure 2*. However, waveform characteristics are variable even for events from the same location and do not appear to be a completely reliable means of identifying events by region.

One of the first observations which came from the spectral analysis was the relative simplicity of earthquake spectra and the complexity of explosion spectra. To illustrate this, we chose two events which are close to one another so that path effects will be nearly the same. This is illustrated in *Figure 3* where the P_n, S_n and L_g spectra of a chemical explosion at the BLA Mine (event 73) and a nearby earthquake (event 82) are compared. Note that the earthquake spectrum is relatively simple and varies smoothly across the entire band. The spectrum of the BLA explosion is more complex in appearance and exhibits spectral nulls near 5 and 10 Hz.

The variation in spectral character among repeated events from the five groups provides an important insight into wave propagation in this region. For example, the small group of events identified as underwater explosions are nearly identical; however, blasts recorded from the Titania mine at approximately the same distance and azimuth show notable differences in their spectra (*Figure 4*). Explosions from the E7 and E8 mines are only 30 km apart but show discernible variations in the pattern of spectral scalloping between the two mines and among repeated events from the same mine (*Figure 5*). In contrast, the spectra of earthquakes to the northwest of NORESS span a much greater distance range but are very similar (*Figure 6*). This implies that the spectra of mine explosions exhibit real source differences, most probably due to differences in the spatial configuration and timing of the charges. This is an important observation, especially in the case where an attempt is made to discriminate between earthquakes and explosions recorded from different source regions.

Spectral characteristics which appear to be strongly path-related are the peak frequency and the high-frequency content. *Figure 7a* is a plot of peak frequency versus distance for all events which shows a decrease in peak frequency with distance. The plot of TMF (*Figure 7b*) versus distance also illustrates the attenuation of high frequencies at greater distances. However, the TMF for the Titania mine blasts and nearby earthquakes shows that high frequencies are propagated from both sources, and that any discrimination based simply on the high-frequence enrichment of explosions relative to earthquakes would fail.

3.2.4. *Q* Estimates and Corner Frequencies

Q and corner frequency estimates for all the events were made by fitting the average velocity spectra of P_n, S_n and L_g to the source model given in (2). The complexity of the explosion spectra generally led to poor convergence and large least-squares error. The earthquake spectra yielded more stable results. The $\omega^{-\gamma}$ model with a frequency dependence of $f^{0.5}$ was found to give the best fit of all the data. *Q* estimates and corner frequencies for the best fitting model are plotted in *Figure 8*. Above 2 Hz, *Q* values are about 500, independent of corner frequency, and appear reliable. Anomalously high *Q* values are associated with corner

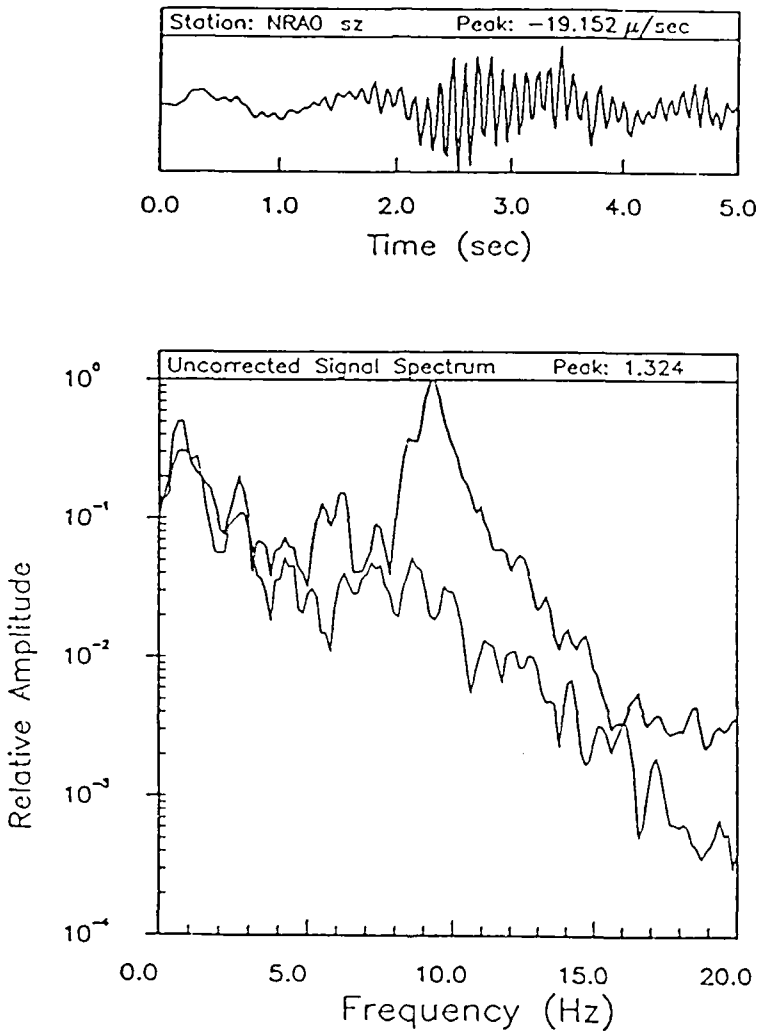

Figure 2. An example of a unique waveform feature recorded at the NORESS array. The recording is that of a P_n wave from a mine in northern Sweden near the city of Nattavaara. The spectrum of this signal is also shown, as is the spectrum of the noise immediately preceding the signal. Note the nearly monochromatic frequency content of the signal. The peak in the spectrum is at 10 Hz.

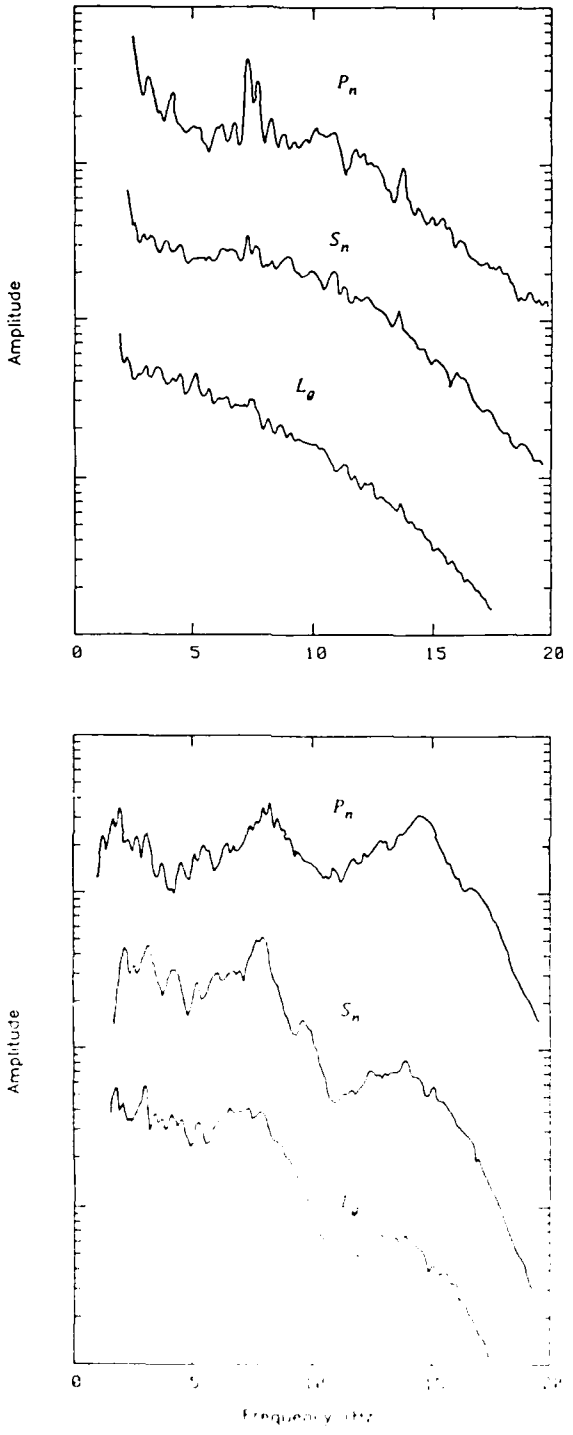

Figure 3. A comparison of typical P_n, S_n, and L_g spectra from an earthquake (top) and a nearby explosion (bottom). The earthquake occurred off the southwest coast of Norway, and the explosion was at the BLA mine.

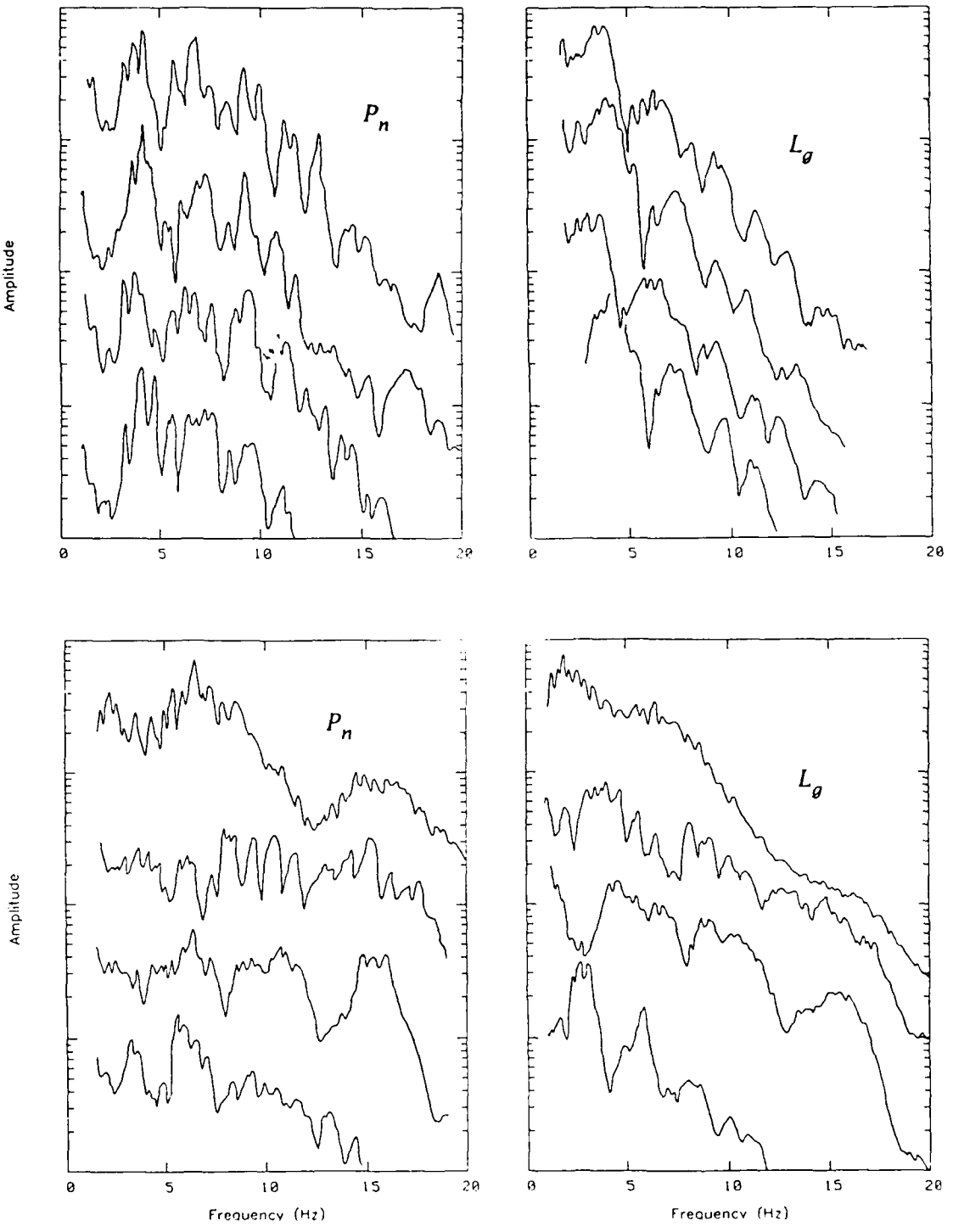

Figure 4. (top) P_n and L_g spectra for four presumed underwater explosions off the southern coast of Norway. Note the similarity in spectral shape for the four events. (bottom) P_n and L_g spectra for four explosions at the Titania Mine in southern Norway. Note the large differences in spectral shape for these events. Since these events are from the same mine, the differences in the observed spectra are likely due to varying explosion source configurations.

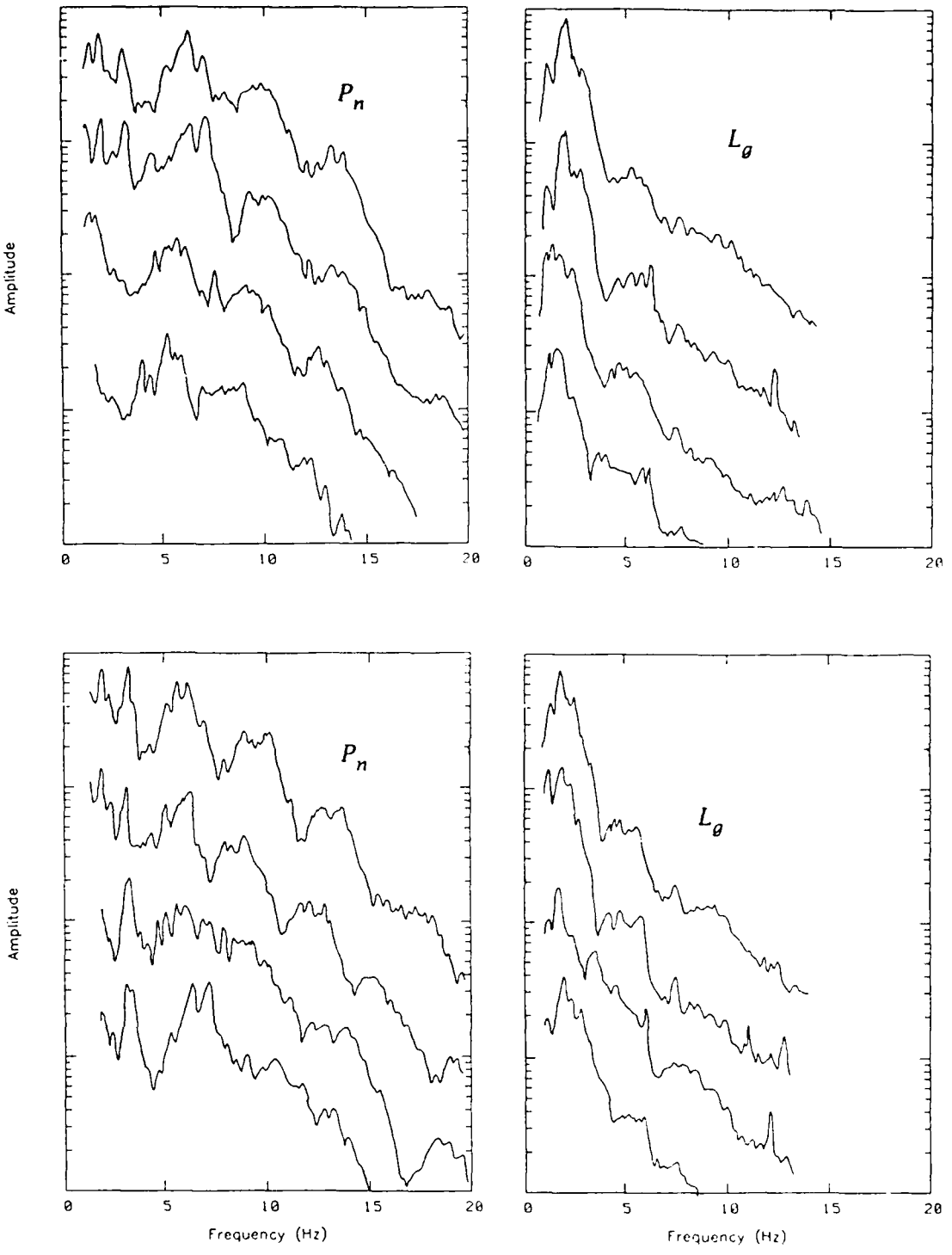

Figure 5. P_n and L_g spectra for four explosions at mine E7 (top) and E8 (bottom). Both mines are southwest of Leningrad.

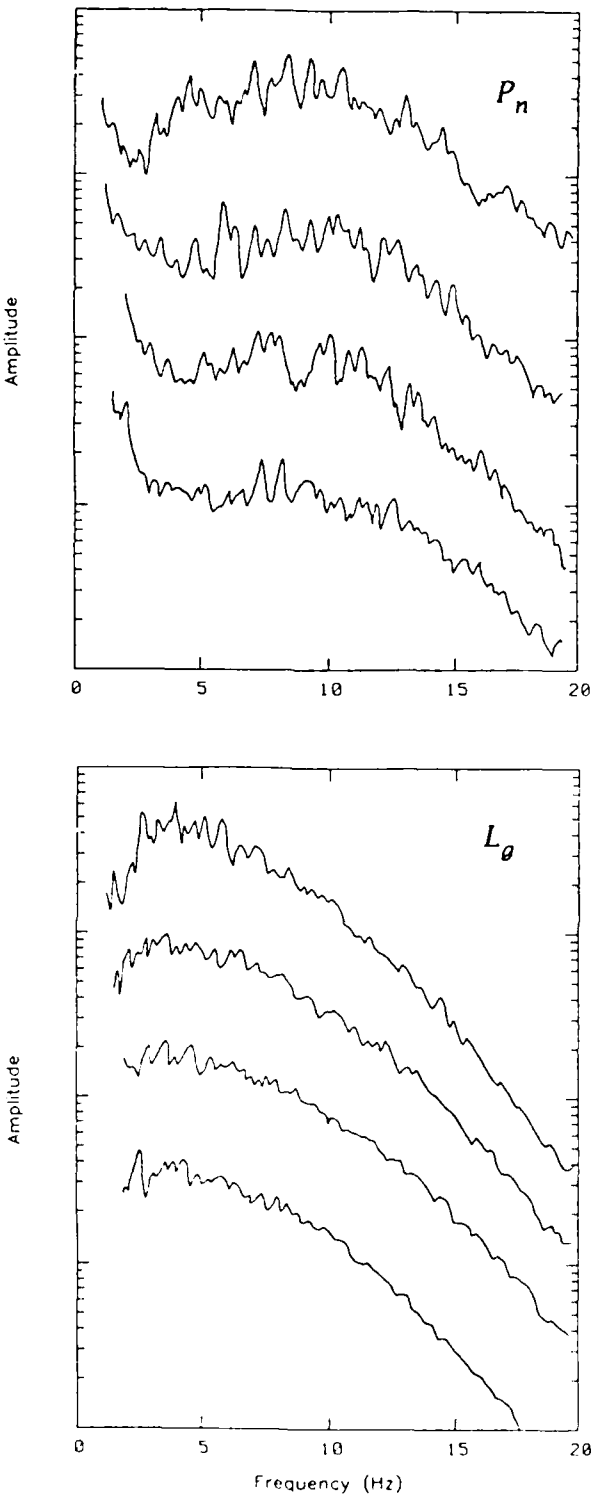

Figure 6. P_n and L_g spectra from four earthquakes off the west coast of Norway. Note the simplicity and similarity of the spectra for these four events, even though they are not located at the same source area.

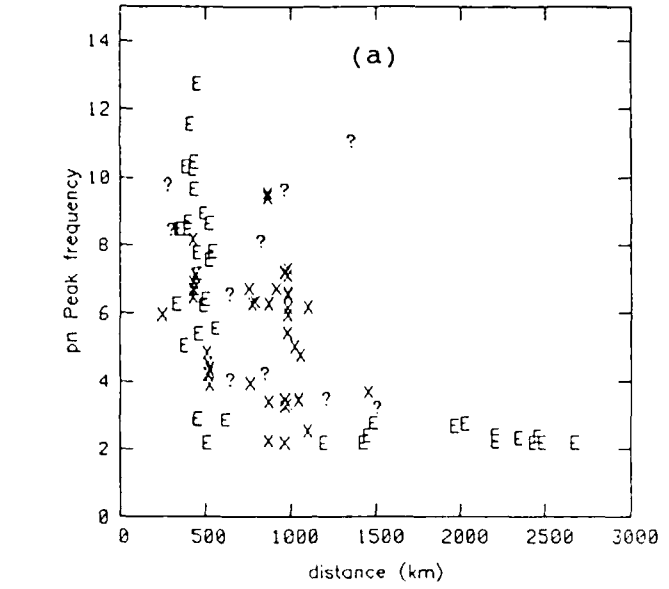

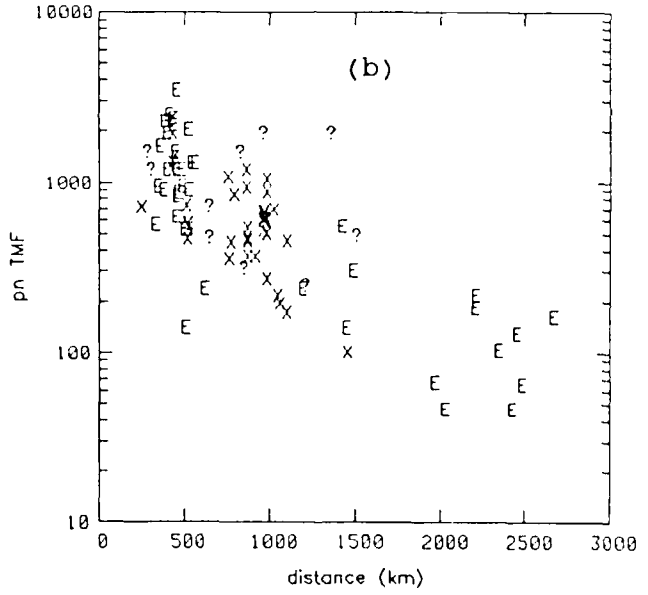

Figure 7. Peak frequency (a) and TMF (b) of P_n waves versus distance for our dataset. An "E" indicates earthquakes, an "X" explosions, and "?" are unidentified events.

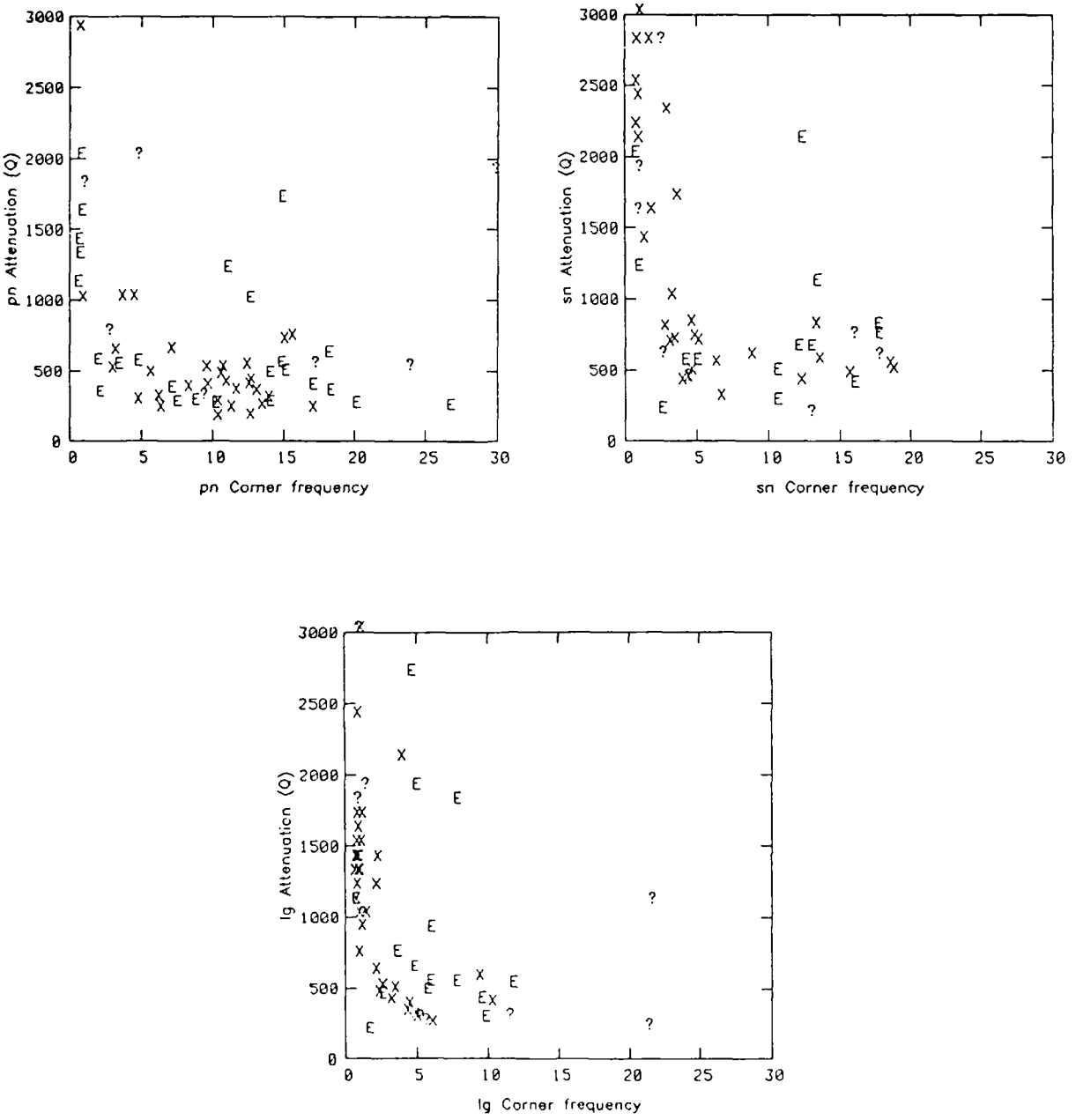

Figure 8. P_n, S_n, and L_g Q values versus their corresponding corner frequencies. "E" indicates earthquake, "X" explosion, and "?" an unidentified event. This figure illustrates the tradeoffs between Q and corner frequency, where low corner frequencies resulted in anomalously high Q values.

frequency estimates below this point. An examination of all the instrument-corrected spectra indicates that this occurs when the spectrum is virtually flat, or limited by the SNR to a narrow low frequency band, making these estimates unreliable.

Because of the inaccuracy of single-station Q estimates due to model dependence, and the inadequacy of the simple source representation to model the wide-band complexity of most spectra, Q estimates should be regarded with caution, and used only as approximate values.

3.2.5. Source Discrimination

As seen in the previous section, discrimination between earthquakes and explosion sources based on their relative high-frequency content would fail due to path effects over greater distances, if indeed such source differences existed. Likewise, path corrections based on single-array Q estimates are not encouraged by the results of the attenuation study, since the simple Q model and source representation was generally inadequate to fit all the data. However, path effects are not so severe as to completely obscure all characteristics of the source which might aid in discriminating between the two source types. Since source theory predicts the generation of more shear energy from earthquake sources compared to explosions, spectral ratios of P_n/S_n and P_n/L_g were among the spectral parameters computed for all the events. Spectral ratios were formed by averaging spectral amplitudes over the optimum signal band. A distinct improvement was seen when this procedure was compared to ratios of peak spectral amplitudes, or ratios formed in selected frequency bands. *Figure 9* shows the P_n/S_n and P_n/L_g amplitude ratios for events where all three phases were clearly recorded. These ratios provide fairly good separation between the two source types, although there are several events for which this discriminant fails. The separation between earthquake and explosion populations appears clearer from the P_n/S_n ratio. A discussion of outliers is presented in the next section.

Figures 4 and *5* illustrated the spectral complexity seen in nearly all the explosion spectra. The spectral complexity of explosion spectra in this data set could occur for a variety of reasons. For instance, chemical explosions detonated during mining activities are often composed of multiple shots such as in the practice of ripple firing. In the case of single shots, multiples due to shallow structure or topography in the source medium could account for a pattern of spectral interference. Such a spectral phenomena has been found for sources in other areas (e.g., Anderson, 1987), and for recording sites in areas of rugged topography (Bard and Tucker, 1985). The complexity seen in the spectra of underwater explosions is commonly attributed to the bubble pulse, or reverberations within the water layer. These effects are nearly always seen in marine seismic exploration data. In all these cases, the effect of the explosion source is to produce a harmonic interference pattern which is detectable by the cepstrum.

Figure 10 shows deconvolved cepstra of P_n, S_n and L_g for four of the explosion sources. *Figure 10b* is a case where the cepstra suggests a specific delay time at about 150 ms, a typical delay time in a ripple fire sequence. The cepstra of events 10-16 each indicate a clear delay time of about 300 ms (not shown). Reverberations within the water layer are typically seen at longer periods, but this delay

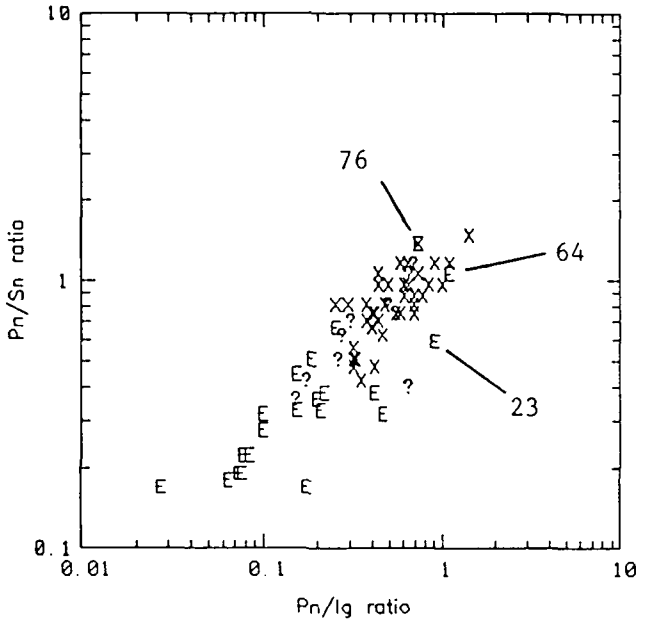

Figure 9. P_n/S_n versus P_n/L_g amplitude ratios for the dataset. These ratios provide good separation between the earthquakes and explosions, with the exception of some outliers. These outliers are discussed individually in the text.

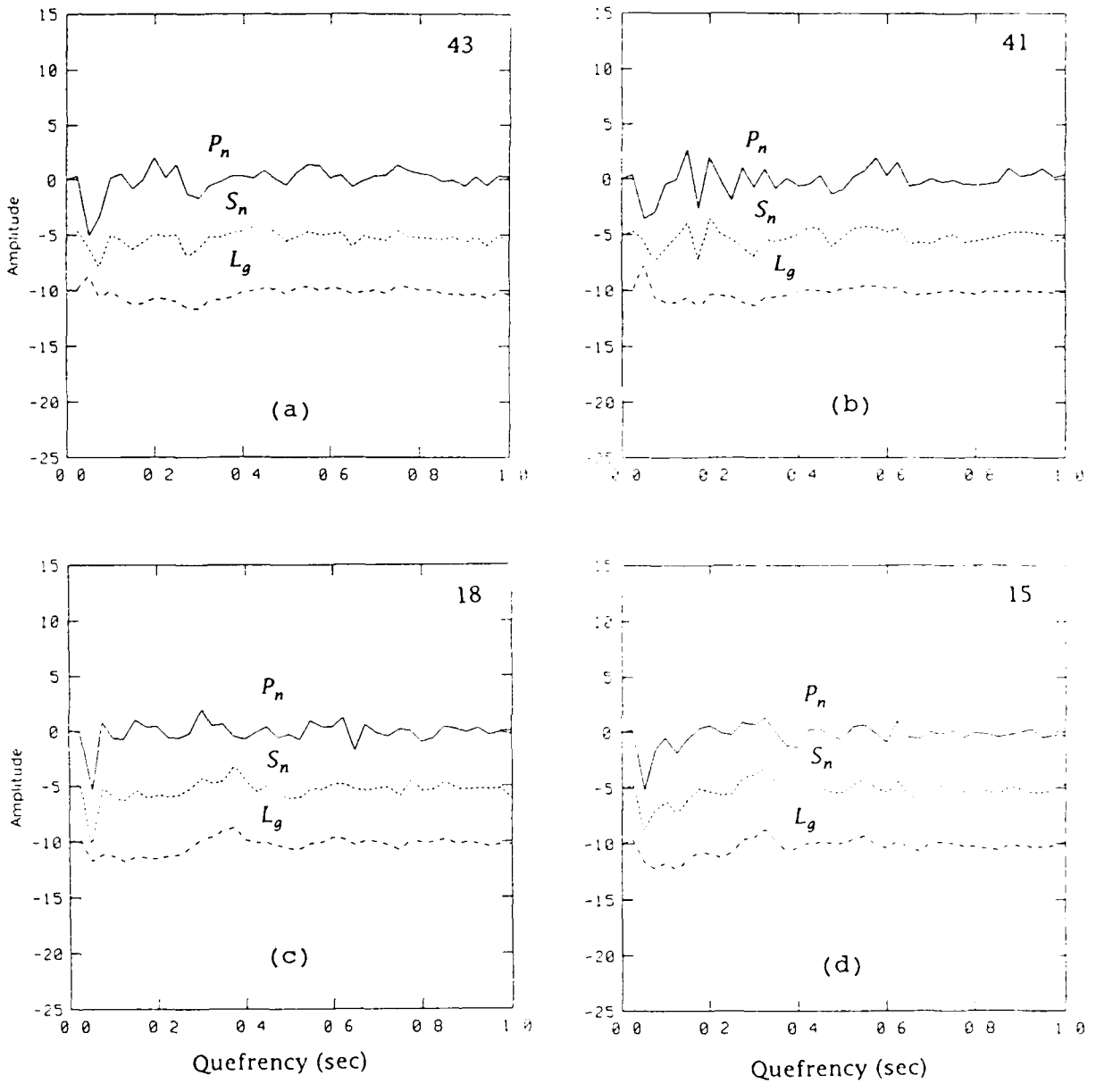

Figure 10. Deconvolved cepstra of P_n (solid lines), S_n (dotted lines), and L_g (dashed lines) waves for four explosions. The cepstral peaks are indicative of the complexity of the source.

time is within the range produced by a bubble pulse from a large underwater explosion at moderate depth. In most cases a clear delay time is not seen in the cepstrum, but the cepstrum can be used as a reliable measure of spectral complexity even when specific delay times are not indicated. The cepstra of earthquakes from different source areas are shown in *Figure 11*. The difference in the degree of complexity between the earthquake and explosion source types is illustrated by the appearance of cepstral peaks in the explosion cepstra, and the absence of such peaks in the earthquake cepstra. The P_n spectra of earthquakes shown in *Figure 6* are somewhat complex, but they do not exhibit a harmonic interference pattern seen in the explosion spectra, and as a result, peaks do not appear in the cepstra.

In order to quantify the cepstral complexity, the variance of the cepstra was computed for all phases and all events in the quefrency range 0.1 to 0.5 seconds. This range in delay times was chosen to include all frequencies in the effective signal band of the spectra. The shortest delay time corresponds to destructive interference at a frequency of one half the Nyquist, and the longest delay at a frequency of 1 Hz, just above the microseismic noise seen in most of the events. The variance of the cepstrum was found to be more diagnostic of explosions than similar parameters derived from the spectra, such as the variance of an N-point running average. *Figure 12* shows the mean P_n, S_n cepstral variance plotted against the P_n/S_n and P_n/L_g amplitude ratios. The separation between the two populations is fairly good, but with several exceptions. It is interesting to note that the cepstral variance points to only one of the same anomalous events (event 23) as the spectral ratios. Automatic identification of these events on the basis on these parameters would work reasonably well, but a more confident identification of the marginal events usually requires a closer inspection of the spectra and cepstra.

3.2.6. Discussion of Outliers

In *Figures 9* and *12*, five events were identified as examples where the cepstral variance, the P_n/S_n and P_n/L_g ratios, or both failed as discriminants between earthquakes and explosions. It is worthwhile examining each of these examples individually to see what reasons caused each of them to fail. As exceptional cases in a case-based identification scheme, the reasons for failure provide important information in the subsequent identification of new events.

In *Figures 13a* and *13b*, the P_n, S_n, and L_g cepstra are plotted for events 32 and 8. Event 32 is an earthquake recorded in northern Sweden, and event 8 is a chemical explosion from the Titania mine in southern Norway. Both events were identified correctly by their spectral amplitude ratios, but they were misidentified on the basis of mean cepstral variance. The cepstra of event 32 in *Figure 13a* exhibit a number of anomalously low cepstral amplitudes in the low quefrency range. These amplitudes are an artifact of the cepstrum near the lower limit of resolution, which resulted in a high variance. In this case the variance was not a reliable measure of complexity. However, by visual inspection, the smooth cepstra of event 32 are seen to be very similar to the cepstra of other earthquakes such as those in *Figure 11*. The cepstra of the mine explosion shown in *Figure 13b* are cases where the cepstra are only marginally adequate to identify source type. It is only the cepstrum of L_g which suggests that this is an explosion when it is compared with the L_g cepstra of other earthquakes shown in *Figure 11*. Nearly all the earthquake L_g cepstra are flat.

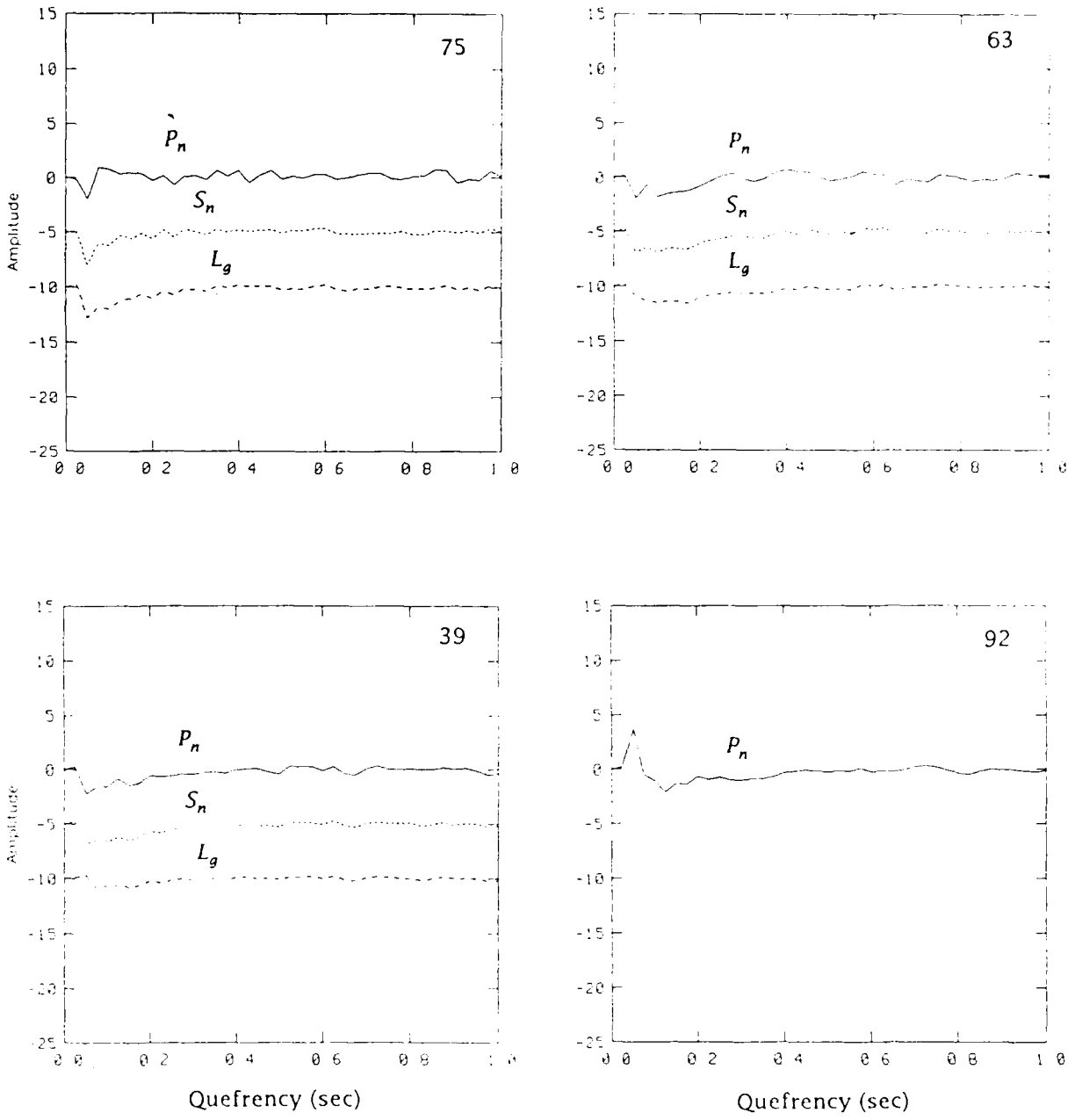

Figure 11. Deconvolved cepstra of P_n (solid lines), S_n (dotted lines), and L_g (dashed lines) waves for four earthquakes. Note the relative simplicity of the earthquake cepstra when compared with the cepstra of the explosions shown in *Figure 10.*

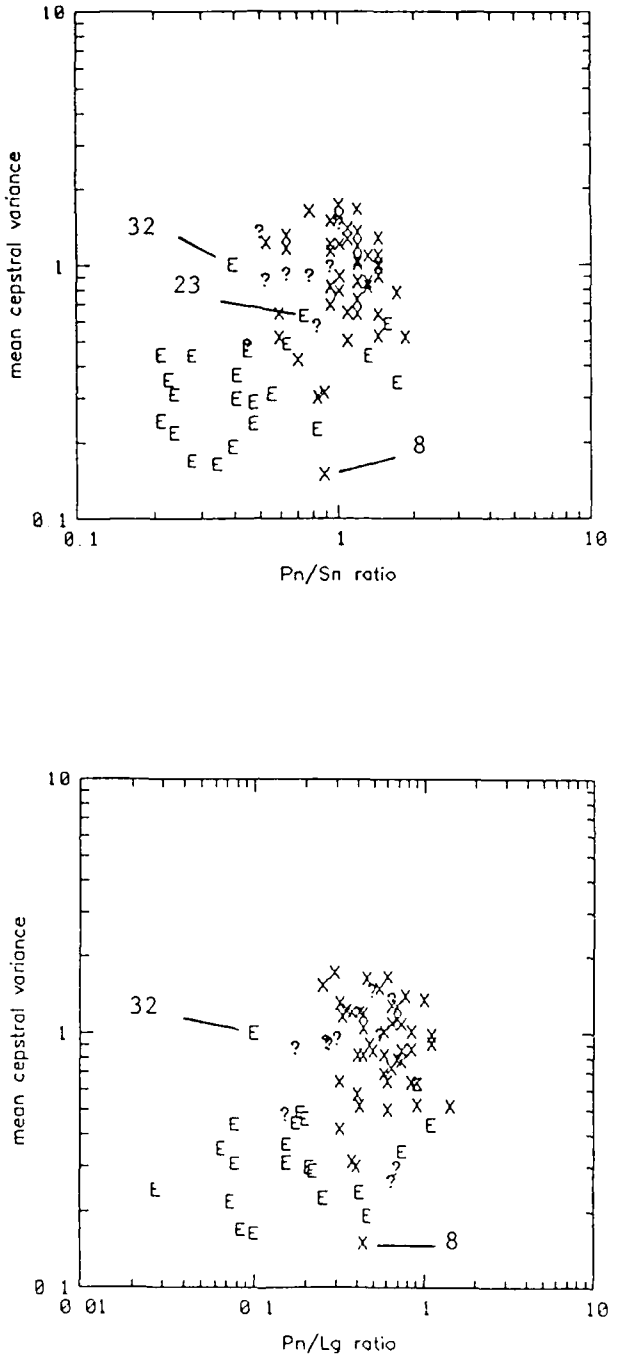

Figure 12. Mean of the P_n, S_n, and L_g cepstral variance for each event plotted as a function of P_n/S_n (top) and P_n/L_g amplitude ratios (bottom). "E" is an earthquake, "X" an explosion, and "?" is an unidentified event. Although the separation between populations is good, a number of outliers exist, and these are discussed individually in the text.

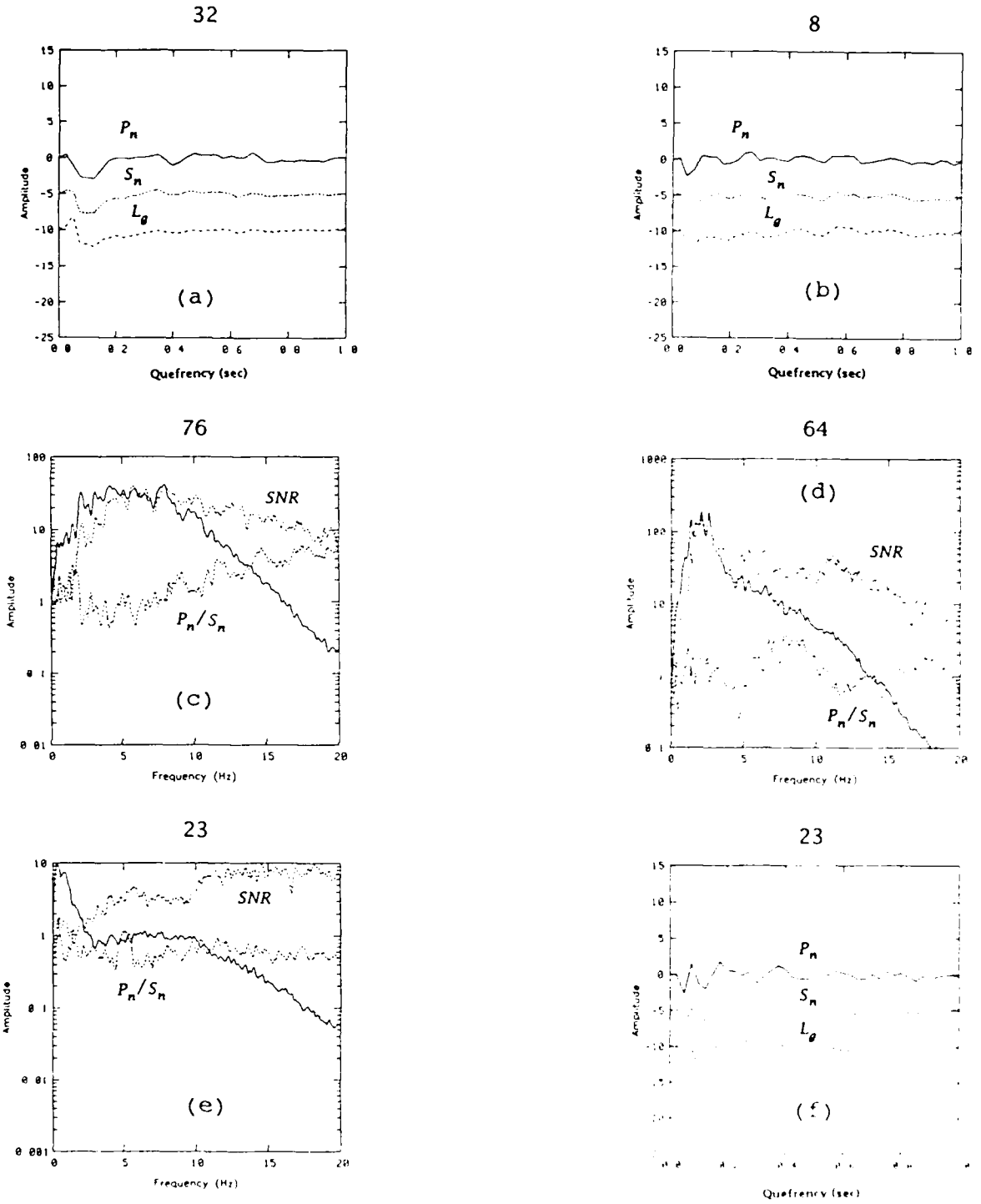

Figure 13. Cepstra (a,b,f) and spectra (solid lines in c,d,e) of outliers shown in *Figures 9* and *12*. Dotted lines in c,d,e are SNR and P_n/S_n amplitude ratios.

In *Figures 13c* and *13d*, the S_n spectra are plotted for two earthquakes (events 76 and 64) which were misidentified on the basis of their spectral amplitude ratios. The SNR and the P_n/S_n ratio are plotted in these two figures as functions of frequency. The SNR curve shows the these two events are well recorded in a band from about 1 to 20 Hz. The cepstra of both these events reflected the simple character of their spectra and they were identified as earthquakes on that basis. The spectral shape of these two events is similar to other earthquakes in this region, but the spectral ratio curve for event 76 in *Figure 13c* indicates that the P_n/S_n ratio is anomalously high when compared with earthquakes from the same source region. This is especially true in the high-frequency band from 10 to 20 Hz. Likewise, the curve for event 64 in *Figure 13d* shows a high P_n/S_n ratio, with an unexplained increase between 5 and 10 Hz. The reason for these observations is unknown.

The final example in *Figure 13* shows the P_n, S_n and L_g cepstra (13e) and the S_n spectrum (13f) for the only event (event 23) for which both discriminants clearly failed. In this case the S/N ratio was low for all phases. As a result, the amplitude ratios were close to one, and the cepstra reflect the complexity of the noise.

3.2.7. Summary

In this report, waveform and spectral characteristics were computed for a suite of 95 regional events recorded by the NORESS array in southern Norway. Early results showed that earthquakes and chemical explosions recorded at similar distances contain similar high-frequency energy. For events at greater distances, the high-frequency amplitudes appear to attenuate strongly with distance, with Q values for P_n, S_n, and L_g waves approximately 500 at 1 Hz with a frequency dependence of 0.5. The third moment of frequency (TMF) and peak frequencies both illustrate the decay of high-frequency amplitudes with distance. Because of this similarity in high-frequency content, discrimination based on the predicted high-frequency content of explosions versus earthquakes would be ineffective.

The results from the measurement of amplitude ratios and spectral complexity indicate that characterization of earthquakes and chemical explosions in this region is possible using a small set of spectral parameters, together with qualitative information gained from the observation of repeatable waveform and spectral characteristics. For events with clear P_n, S_n and L_g arrivals, the P_n/S_n and P_n/L_g ratios are consistent with the prediction of greater shear wave energy from earthquake sources. Observations of chemical explosions at several known mining sites in Norway, Sweden and the western Soviet Union indicate that a complex pattern of spectral interference, presumably due to near-source effects or multiple firing, is a repeatable spectral characteristic of mine blasts recorded in this region. This complexity appears to be absent from the earthquake spectra.

The results of the event characterization study are generally good, with exceptions which are dependent on the SNR, and to some extent on the choice of constraints and ranges which were selected for the computation of spectra ratios and cepstral variances. In addition there are several anomalous events which remain unexplained. However, the general procedure employed in this study is flexible, and appears effective in pointing to events which require further analysis, and in gaining the type of case-based knowledge required by an automated event identification system.

Paul S. Dysart
Jay J. Pulli

REFERENCES

Anderson, D., 1987. "Deconvolution of Mine-blast Ground Motion," *(abstract), Trans. Amer. Geophys. Union*, 68: 355.

Aviles, C. A. and Lee, W. H. K., 1986. "Variations in Signal Characteristics of Small Quarry Blasts and Shallow Earthquakes," *(abstract), Trans. Amer. Geophys. Union*, 67: 1093.

Bard, P. and Tucker, B. E., 1985. "Underground and Ridge Site Effects: A Comparison of Observation and Theory," *Bull. Seis. Soc. Am.*, 75: 905-922.

Oppenheim, A. V. and Schafer, R. W., 1975. "Digital Signal Processing," *Prentice-Hall, Inc., New Jersey.*

Pomeroy, P. W., Best, J. W., and McEvilly, T. V., 1982. "Test Ban Treaty Verification with Regional Data - A Review," *Bull. Seis. Soc. Am.*, 72: S89-S129.

Sereno, T. J., Bratt, S. R., and Bache, T. C., 1987. "Generalized Inversion for Attenuation and Seismic Moment," *Semi-Annual Technical Report SAIC 87/1736*, 104 pp.

Weichert, D. H., 1971. "Short-period Spectral Discriminant for Earthquake and Explosion Differentiation," *Z. Geophys.*, 37: 147-152.

4. OTHER RESEARCH

4.1. A DETERMINATION OF AZIMUTHS OF SEISMIC EVENTS USING TELESEISMIC *P* AND RAYLEIGH WAVE POLARIZATION

4.1.1. Introduction

Well-defined azimuths of arrival of *P* and Rayleigh waves can be used to assist in obtaining an initial approximation to the epicenter of an event. These azimuths of arrival may also help associate an observed phase with the correct epicenter when two or more events occur at approximately the same time.

The objective of this study is to determine if recently developed analysis methods can improve the direction-finding ability of three-component seismic stations, and to develop computer-aided methods for obtaining this information. If successful, seismic workstations at a National Data Center (or at a seismic station) could have the capability to automatically measure azimuth of arrival, or "backazimuth" as it is commonly referred to.

Results of this study show that accurate backazimuth measurements can be obtained from *P*-waves recorded at stations situated in homogeneous geology. A complex geological setting greatly reduces the accuracy. Backazimuth measurements from Rayleigh waves show more scatter, but appear to be less sensitive to local geology. The analysis method is simple and rapid in practice. It is recommended that stations in suitable geological settings should routinely report backazimuth in future international data exchange experiments.

4.1.2. Methods

Azimuthal information can be extracted from three-component data through estimates of ground-motion polarization of *P* and Rayleigh waves. A number of investigators have previously described polarization analysis methods, and some of these have been reported to the GSE. The analyses reported here build on these previous studies, and have been applied to data from three RSTN seismic stations.

The essence of the method employed in this investigation is to compute the polarization ellipse that is a best fit, in a least squares sense, to the earth particle motion measured over short-time windows in the *P* and Rayleigh wavetrains. The orientation of the principal axis of the polarization ellipse provides an unambiguous measure of the direction of arrival and angle of incidence of *P*. Similarly, the two principal axes, together with the sense of the rotational motion, provide an unambiguous measure of the direction of arrival of Rayleigh waves. The algorithm used here was developed by Jurkevics (1986a, 1986b) and shown to be very fast and effective for measuring polarization characteristics of seismic waves.

The main thrust of the investigation to be reported here was to evaluate the effectiveness of the referenced algorithm for determining the direction of arrival of

P and Rayleigh waves from *teleseisms*. Such events provide the most stressing test of the method's effectiveness, because of the unfavorable angle of incidence of *P* and the increased probability of refraction and multipathing effects on Rayleigh waves over longer paths. Waveforms of teleseismic events were obtained from the database compiled by the United States during the Group of Scientific Experts Technical Test (GSETT). This database is particularly useful for investigations such as that being reported here because it contains, in addition to digital seismic waveforms from events detected by seismic stations RSSD, RSON, and RSNY, a complete set of measured parameters on each event, including noise. The specific events selected for analysis are listed in Table I, Appendix I, which also lists the waveforms available for use.

A short description of the analysis procedure follows. Analysis was performed interactively on a Sun 3/160 workstation. Waveform segments containing the *P*-waves were 120 seconds long. The short-period waveform segments at each station were decomposed into four frequency bands: 0.5-1.0, 1.0-2.0, 2.0-4.0, and 4.0-8.0 Hz and displayed on the screen. After a visual inspection, the frequency band with the highest signal-to-noise ratio was selected. Polarization parameters were computed over a 2- to 5-second window (more accurately, over approximately six cycles in the selected pass band as described by Jurkevics (1986a, 1986b). In practice, three polarization parameters -- amplitude, rectilinearity,[1] and incidence angle -- were displayed along with the waveforms. These parameters were used to help the analyst select the portion of the signal containing the purest *P*-wave motion, at which time the azimuth was recorded. (Pure *P*-waves are characterized by high rectilinearity, whereas pure noise is characterized by minimal values.) The backazimuth of each event determined by this method is given in Table I, Appendix I, where it can be compared with the calculated azimuth to the epicenter.

Waveform segments containing the Rayleigh wavetrain were 1250 seconds long. Each of the three components of motion were decomposed into three frequency bands: 0.016-0.05, 0.03-0.1, 0.1-0.2 Hz. The best band was selected and polarization parameters were computed over an approximately 120-second window (approximately four cycles in the selected passband). For the analysis of the Rayleigh waves, the axes of the polarization ellipse were constrained to lie in the vertical and horizontal directions (horizontal azimuths unconstrained). Three polarization parameters, amplitude, planarity,[2] and Hmax/Hmin,[3] were displayed along with backazimuth and the waveforms to aid the analyst in choosing the portion of the wavetrain containing the purest Rayleigh wave motion. These parameters also enabled a separation of the Rayleigh waves from the earlier Love waves. (A pure Rayleigh wave would be indicated by high values of the three parameters.) The backazimuth at the selected time in the wavetrain was recorded, and is given in Table I, Appendix I, where it can be compared with the calculated bearing of the epicenter.

4.1.3. Results

---

[1]Rectilinearity: A measure of the length of the major axis as compared with the average of the minor axes of the polarization ellipse. (Jurkevics 1986a, 1986b)

[2]Planarity: A measure of the average length of the vertical and largest horizontal axis as compared with the smallest horizontal axis. (Jurkevics 1986a, 1986b)

[3]Hmax/Hmin: Ratio of the length of the largest to the smallest horizontal axis.

Results of the analysis of the data are summarized in the following section of this report, separately for teleseismic *P*-waves and Rayleigh waves. Rayleigh waves were not clearly visible from all the teleseismic events, and neither did all three stations record *P* from all the events.

A. Results from Teleseismic *P*-Wave Analysis

Figure 1 shows histograms of azimuth residuals from *P*-waves at each of the three stations used in this study. Table A shows the associated means, medians, and standard deviations of the residuals, determined as the backazimuth obtained by polarization analysis, minus the calculated backazimuth. As noted in *Figure 1* and Table A, azimuths measured from polarization analysis of *P* are, on the average, good estimates of the direction to the epicenter. On the other hand, individual estimates may differ significantly from the calculated azimuth of the epicenter. For *P*-waves, RSSD has the greatest dispersion in azimuth of arrival, with a standard deviation of 79°. RSON and RSNY have much smaller dispersions.

Table A. Backazimuth Residuals of Selected Events for RSNY, RSON and RSSD Derived from Polarization Analysis of Teleseismic *P*-Waves

Short-Period	Arithmetic Mean (deg.)	Standard Deviation (deg.)	Median (deg.)
All Stations (absolute values)	10.31	52.56	11.43
RSNY	-16.81	30.61	-16.51
RSON	2.03	21.78	0.10
RSSD	12.10	79.29	17.67

The arithmetic mean and the median are similar for a given station except for RSSD. This difference indicates something other than a normal distribution, and skewness in the measurements at RSSD is also clearly evident from inspection of *Figure 1*. RSON and RSNY have means and medians which do not differ greatly, consistent with a normal distribution. However, inspection of *Figure 1* suggests that the measurements at these stations could also be slightly skewed, although this appearance may be an artifact of the limited size of the data set analyzed.

Figure 1. *P*-wave azimuthal error for stations RSNY, RSON, and RSSD.

There is also an evident systematic offset in azimuths obtained from RSNY. On November 3, 1986, the instrument at RSNY was pulled out of the ground, and its orientation was measured. It was found that the horizontal instruments had been mis-oriented by 17° (counter-clockwise) with respect to the cardinal directions and is in excellent agreement with our findings of the backazimuth residual, which averaged -16.8°. RSON and RSSD have no known instrument mis-orientation but it should be noted that RSSD recordings are difficult to read accurately, because signals tend to be complicated. Thus, we conclude that, after allowing for known instrument misorientation, polarization analysis of teleseismic *P*-waves yielded accurate, unbiased estimates of the backazimuth to the epicenter of events recorded at two stations, but significantly less accurate estimates at the third (RSSD).

Seismic noise is expected to perturb measurements of backazimuth by distorting the shape of the polarization ellipse. As may be seen in *Figure 2*, however, the polarization method used in this study is remarkably robust, and the azimuthal errors are almost unaffected by noise down to signal-to-noise ratios near 1. Paradoxically, RSNY which yielded the most accurate azimuths, had the lowest signal-to-noise ratio on the average; RSSD, which yielded the least accurate azimuths, had the highest signal-to-noise ratio on the average. This result suggests that the unfavorable results at RSSD are the consequence of causes other than distortion of the waves by noise contamination.

In an attempt to further understand the results of the azimuthal measurements, the rectilinearity of the particle motion during *P* was also examined. A rectilinearity of 1.0 is indicative of pure *P*-wave motion, whereas pure noise would have a rectilinearity of zero (Jurkevics 1986a, 1986b). Results are shown in *Figure 3*. It may be seen that the most discrepant observations at RSNY and RSSD have rectilinearities of 0.8 or less, and that a large fraction have rectilinearities of 0.9 or higher. By contrast only a small fraction of measurements at RSSD are larger than 0.9. This information, together with the information on signal-to-noise ratio previously presented, constitutes strong evidence that *P*-waves received at RSSD have undergone substantial distortion along the path to the station -- presumably in the crustal portion immediately below the station. This conclusion is consistent with other studies (Taylor and Qualheim, 1983; Owens et al., 1983) which have described evidence for complicated geology at RSSD. The accurate azimuths obtained at RSNY and RSON, together with the evidence for relatively undistorted *P* wavetrains, is also consistent with studies that indicate relatively homogeneous geology at these sites.

Figure 4 shows the measured incidence angle as a function of epicentral distance (range). Data from RSNY and RSON show trends that follow the theoretically expected angles of incidence, assuming a surface velocity of 6.0km/sec. Data from RSSD does not follow this expected trend and shows no coherent relationship between range and angle of incidence -- again a consequence of distortion to the *P*-waves by complex geology.

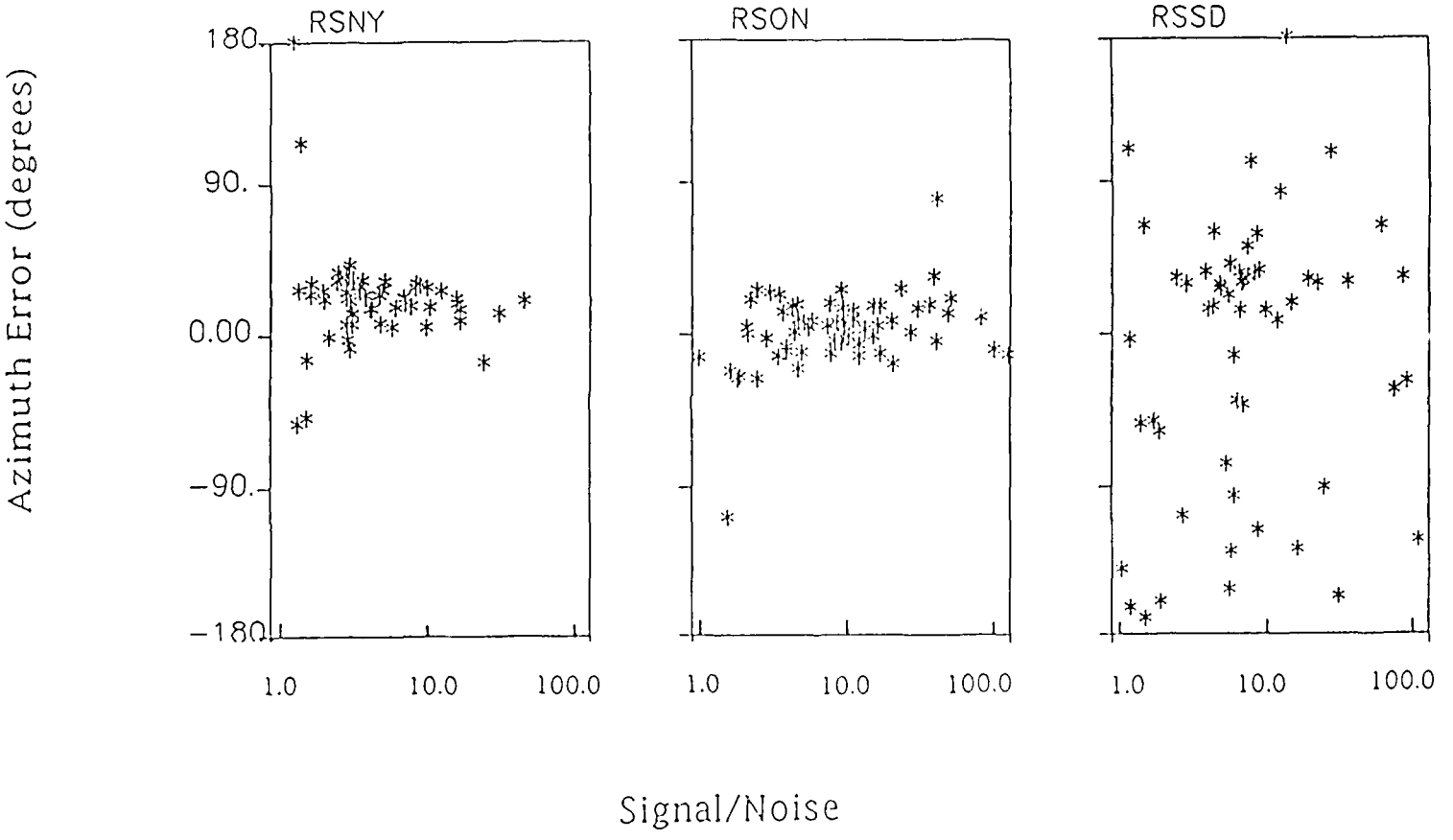

Figure 2. Azimuthal errors as a function of signal-to-noise ratio for *P*-waves recorded at stations RSNY, RSON, and RSSD.

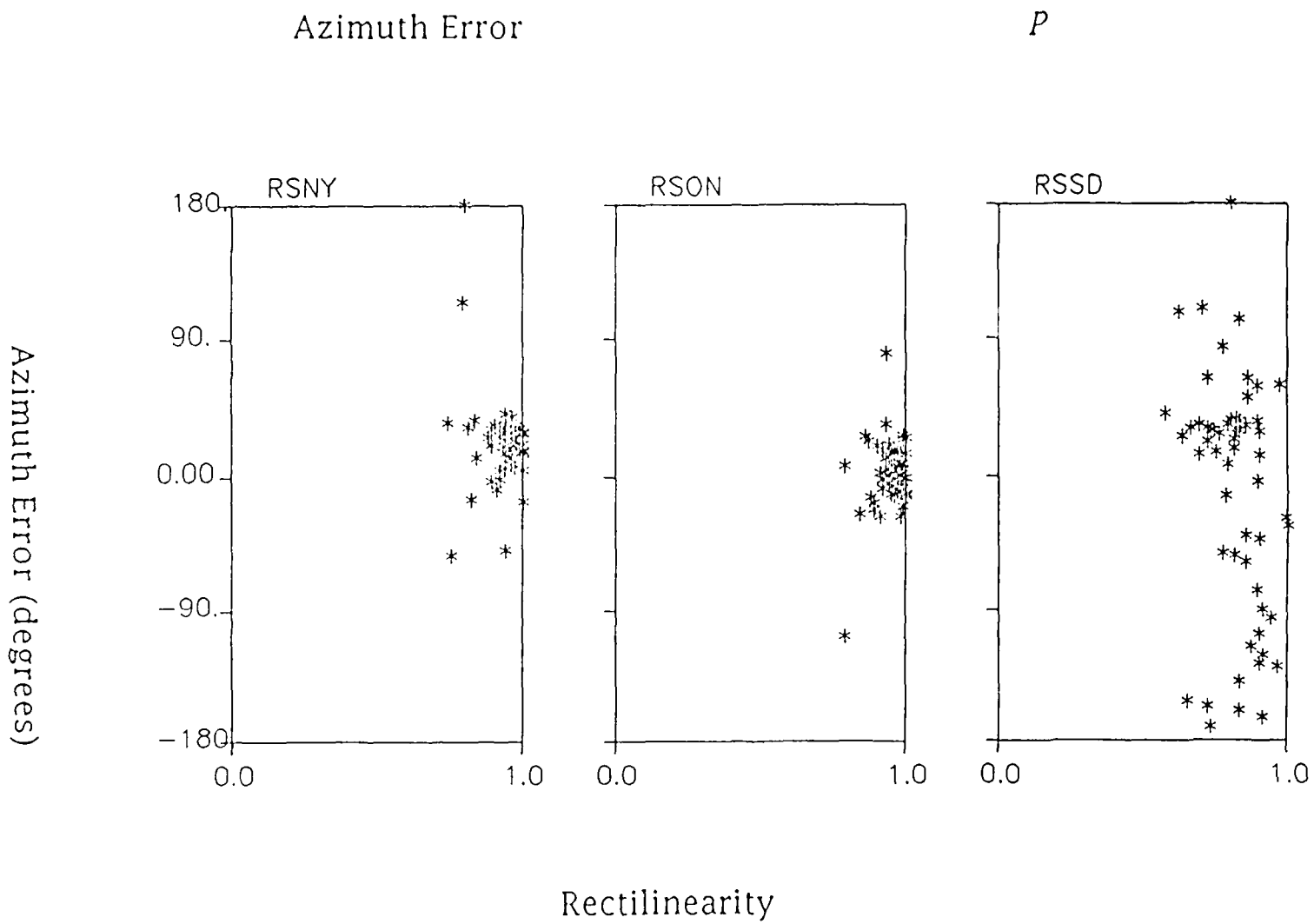

Figure 3. Rectilinearity of *P*-waves recorded at stations RSNY, RSON, and RSSD.

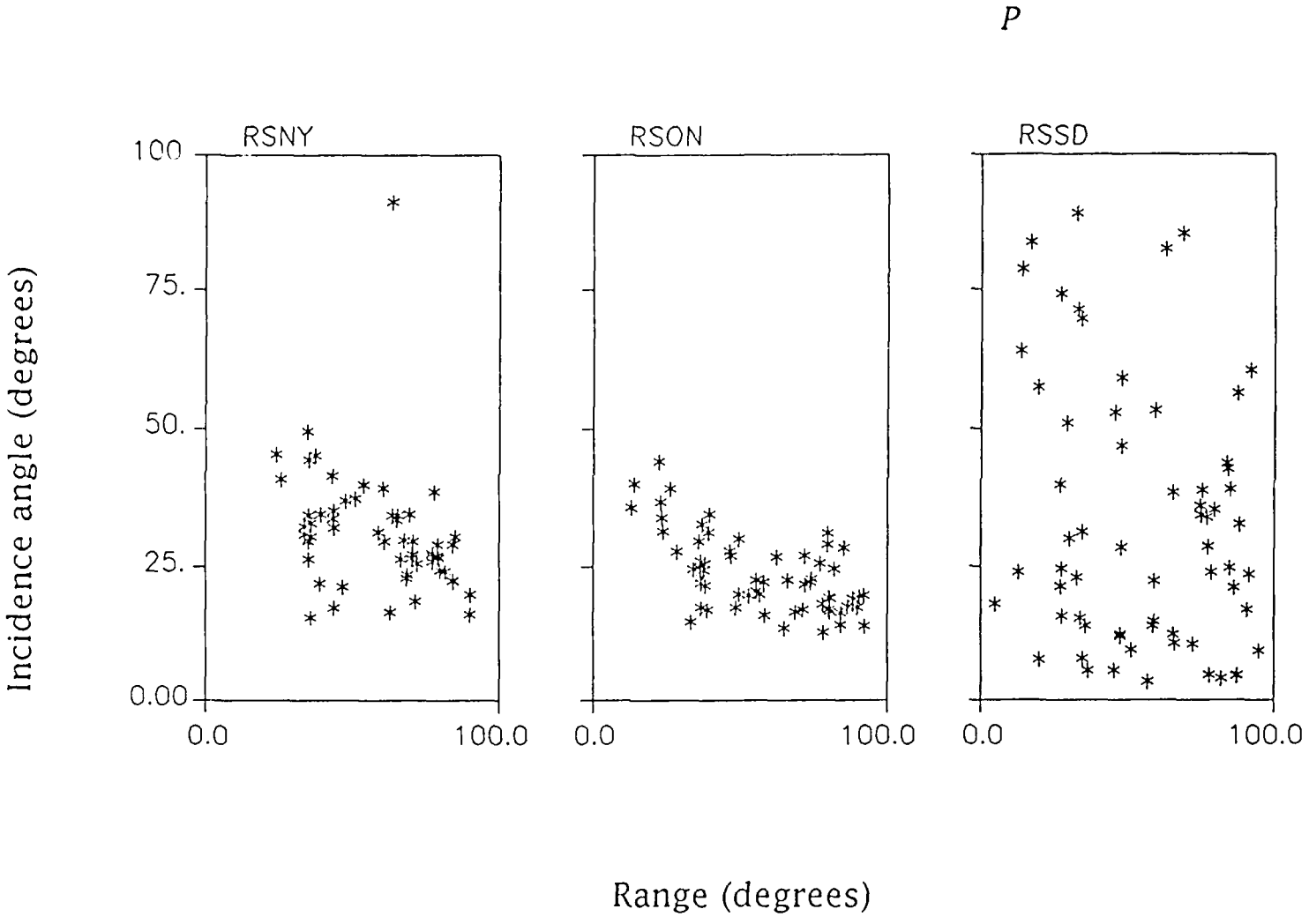

Figure 4. Range (epicentral distance) verses incidence angle for *P*-waves.

B. Results from Rayleigh Wave Analysis

Backazimuths measured from the Rayleigh waves relative to the calculated azimuth of the epicenter are shown in *Figure 5* and summarized in Table B. The arithmetic means and the medians are dissimilar for all stations, emphasizing the skewness of the histograms shown in *Figure 5*.

Table B. Azimuthal Anomalies of Selected Events for RSNY, RSON, and RSSD Derived from Polarization Analysis of Rayleigh Waves

Long-Period	Arithmetic Mean (deg.)	Standard Deviation (deg.)	Median (deg.)
All Stations (absolute values)	7.2	62.3	7.8
RSNY	-7.8	57.7	10.2
RSON	6.6	57.6	2.1
RSSD	7.2	69.8	11.1

The arithmetic means are quite low, giving the indication that, on the average, Rayleigh waves are following close to the great circle path. However, the large standard deviations would appear to preclude the use of individual measurements from Rayleigh waves as a good indication of the epicentral azimuth, although the backazimuth may provide supporting evidence for associating an observed Rayleigh wavetrain with a given epicenter.

Figure 6 examines the dependency of the accuracy of the measured backazimuths on signal-to-noise ratio. In general, signal-to-noise ratios for the Rayleigh waves were rather low. All values were less than 30 with only 3% of the ratios greater than 10. However, the results are sufficient to indicate that there is at most a slight correlation between signal-to-noise ratio and Rayleigh wave azimuth, suggesting that noise interference is not the primary cause of the observed large scatter.

As previously mentioned, a planarity (or "flatness") value of 1.0 is indicative of pure Rayleigh wave motion. *Figure 7* displays the planarity of the measurements taken at the three stations. 70% to 80% (depending on the station) of these values are 0.9 or better, indicating the purity of Rayleigh waves is generally good, according to this test. As was the case for rectilinearity of the *P*-waves, RSON has the purest signals, with RSSD having the most contamination. The planarity test establishes a necessary condition for pure Rayleigh waves, but not a sufficient condition we can not preclude the possibility that the Love waves may be in phase (or anti phase) with the Rayleigh waves, shifting the plane of apparent Rayleigh rotation out of the great-circle direction. Multipath Rayleigh arrivals could cause similar effects.

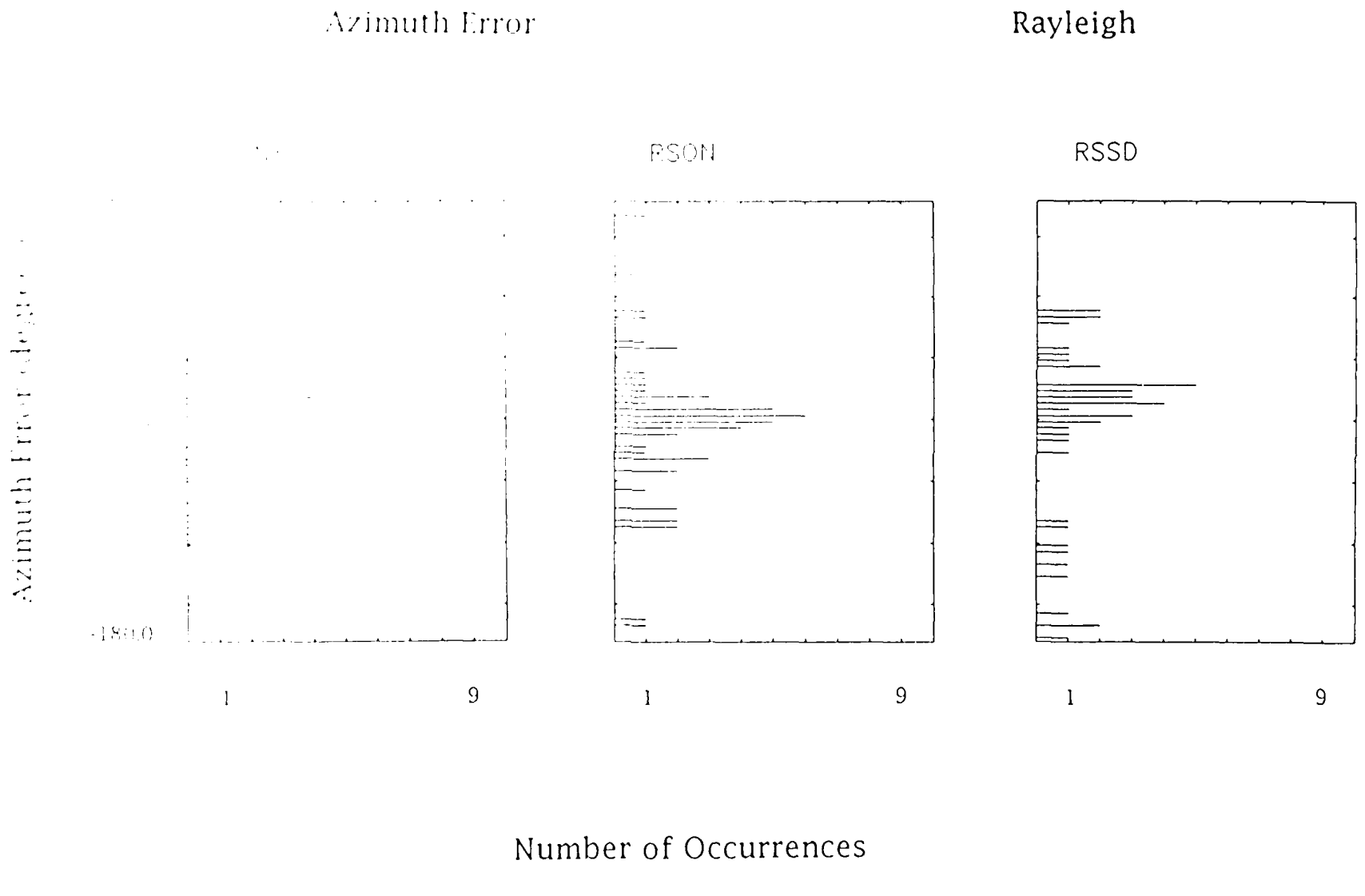

Figure 5. Rayleigh wave azimuthal error for stations RSNY, RSON, and RSSD.

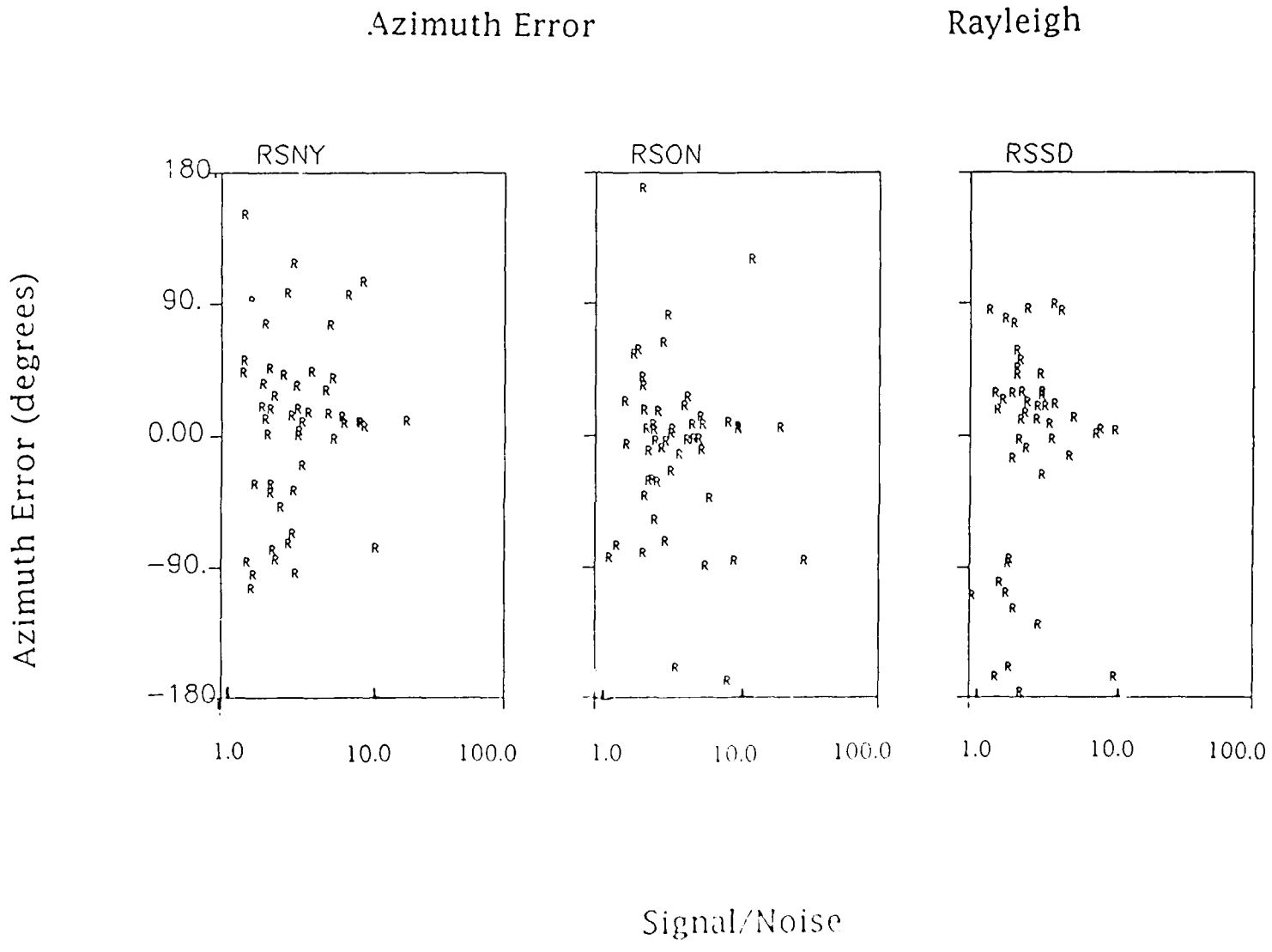

Figure 6. Azimuthal errors as a function of signal-to-noise ratio for Rayleigh waves recorded at stations RSNY, RSON, and RSSD.

Azimuth Error (degrees)

of course, but we would not expect these to result in azimuthal errors of the magnitude observed. We conclude that, although it is usually possible to select a portion of the Rayleigh wavetrain exhibiting planar elliptical motion, it is often perturbed by other wave motion -- probably Love waves in most cases. Polarization analysis, therefore, does not produce accurate backazimuth measurements based on Rayleigh waves.

4.1.4. Conclusions

This investigation has demonstrated a fast and effective method for determining the direction of arrival of *P*-waves by computer-aided polarization analysis. Such measurements, using data from "transparent" station sites, are accurate enough to assist International Data Centers in certain of their analysis functions. However, accuracies may be substantially degraded at stations where the geologic structure is complicated. Investigations similar to those reported here should be undertaken to establish the accuracies attainable at other stations. Depending on the results of such investigations, selected stations should routinely report backazimuth in future data exchange experiments like the GSE Technical Test. The measured rectilinearity appears to provide a good criterion for determining which stations produce reliable backazimuths.

Azimuths measured from determining the plane of motion at the time of arrival of Rayleigh waves were significantly less accurate than for *P*. There are indications that this results from contamination of the Rayleigh waves by Love waves. Results may be helpful in some cases in associating a Rayleigh wavetrain with the correct event, but routine reports are not recommended.

Antoinette Campanella

REFERENCES

Jurkevics, A., 1986a. "A Polarization Processing Algorithm with Applications to RSTN Data," *SAIC Quarterly Technical Reports for July-September and October-December 1985, Center for Seismic Studies Technical Report C86-05.*

Jurkevics, A., 1986b. "Polarization Analysis Using an Array of Three-Component Sensors," *SAIC Quarterly Technical Report for July-September 1986, Center for Seismic Studies Technical Report C86-07, November 1986.*

Owens, T. J., Taylor, S. R., and Zandt, G. "Crustal Structure Beneath RSTN Stations Inferred from Teleseismic *P* Waveforms: Preliminary Results at RSCP, RSSD, and RSNY," *Rep. USID-19859,* 28 pp., Lawrence Livermore Natl. Lab., Livermore, Calif., 1983b.

Taylor, S. R. and Qualheim, B. J. "RSTN Site Descriptions," *Rep. UCID-19769,* 79 pp., Lawrence Livermore Natl. Lab., Livermore, Calif., 1983.

APPENDIX I

EVENTS USED IN THE ANALYSIS

Table I. P and Rayleigh Wave Data for Selected Teleseismic Events

DATE (1984)	ORIGIN TIME	LAT. (deg.)	LONG. (deg.)	MAG. (m_b)	STATION	BACKAZIMUTH (CALC.)	MEASURED BACKAZIMUTH OF P	MEASURED BACKAZIMUTH OF RAYLEIGH
10/17	09:11:04.8	50.3N	153.5E	5.0	RSNY	330.75	315.12	288.48
					RSON	319.01	331.88	260.82
					RSSD	316.11	76.64	305.69
10/18	09:46:17.4	40.7N	42.6E	5.2	RSNY	43.65	32.63	42.96
					RSON	32.04	47.76	24.52
					RSSD	24.64	105.79	27.50
10/18	15:30:21.2	42.4N	105.7W	5.0	RSNY	275.57	267.59	263.17
10/19	22:59:57.8	16.6N	98.5W	4.9	RSNY	223.47	211.83	192.72
					RSON	188.14	192.65	219.54
					RSSD	168.61	344.12	84.56
10/20	03:21:17.4	48.5N	154.8E	5.2	RSNY	329.01	310.13	278.72
					RSON	317.00	348.25	300.28
					RSSD	313.96	48.94	72.64
10/20	17:59:11.9	24.1S	66.8W	6.1	RSNY	172.44	159.05	238.86
					RSON	155.08	177.35	237.71
					RSSD	145.35	86.51	60.76
10/20	22:19:06.1	20.4N	116.0W	4.6	RSNY	248.52	227.71	240.47
					RSON	218.16	245.11	216.93
					RSSD	206.59	195.78	118.11
10/22	07:59:35.7	20.1N	116.1W	4.5	RSNY	248.30	301.46	239.67
					RSON	218.09	196.78	212.39
					RSSD	206.56	185.26	221.23
10/23	08:04:46.1	55.7N	165.0E	4.8	RSNY	328.39	302.71	325.65
					RSON	317.69	306.40	0.37
					RSSD	316.78	285.89	294.20
10/25	06:29:57.1	73.4N	55.2E	5.4	RSNY	15.16	354.23	2.10
					RSON	10.52	25.05	12.60
					RSSD	6.61	68.92	
10/25	08:15:50.1	26.7N	110.4W	4.2	RSNY	250.28	249.21	146.16
					RSON	214.04	215.18	303.05

Table I. P and Rayleigh Wave Data for Selected Teleseismic Events -- (Continued)

DATE (1984)	ORIGIN TIME	LAT. (deg.)	LONG. (deg.)	MAG. (m_b)	STATION	BACKAZIMUTH (CALC.)	MEASURED BACKAZIMUTH OF P	OF RAYLEIGH
10/25	12:39:08.0	51.8N	175.1W	5.0	RSNY	316.46	13.24	349.66
					RSON	304.76	323.17	2.33
					RSSD	305.97	314.45	286.86
10/25	14:38:28.4	40.3N	21.9E	5.0	RSNY	55.50	28.83	14.28
					RSON	46.01	61.31	56.46
					RSSD	38.51	82.94	54.03
10/26	03:01:45.8	13.1N	90.7W	4.4	RSNY	208.74	98.27	170.28
					RSON	175.23	165.12	183.87
					RSSD	155.68	96.97	104.98
10/26	04:02:14.0	13.1N	87.0W	4.5	RSNY	202.58	174.99	
					RSON	149.40	173.93	172.89
					RSSD	149.56	70.57	121.70
10/27	01:50:10.6	50.0N	78.9E	6.1	RSNY	16.85	7.10	356.34
					RSON	4.84	0.05	0.58
					RSSD	358.11	31.01	328.99
10/27	05:59:57.1	46.9N	48.2E	4.7	RSNY	36.40	15.05	
					RSON	25.65	25.84	
10/27	06:04:57.1	46.8N	48.2E	4.4	RSNY	36.47	19.96	130.84
					RSON	25.69		355.58
					RSSD	18.65	74.61	290.94
10/27	06:55:14.7	13.5N	89.9W	4.0	RSNY	207.68	175.88	174.09
					RSON	173.92	166.71	154.13
					RSSD	154.09	311.94	264.02
10/30	03:14:00.1	33.5S	70.2W	5.4	RSNY	176.31	149.67	
					RSON	160.55	140.80	40.63
					RSSD	152.14	106.03	
10/30	14:39:48.4	39.5N	15.5E	4.7	RSNY	59.55	38.08	
					RSON	50.61	61.77	
					RSSD	42.94	143.18	
11/02	03:48:48.9	15.2N	89.9W	5.4	RSNY	208.77	183.90	133.46
					RSON	173.72	170.99	166.70
					RSSD	153.03	125.49	162.48

Table I. P and Rayleigh Wave Data for Selected Teleseismic Events -- (Continued)

DATE (1984)	ORIGIN TIME	LAT. (deg.)	LONG. (deg.)	MAG. (m_b)	STATION	BACKAZIMUTH (CALC.)	MEASURED BACKAZIMUTH OF P	MEASURED BACKAZIMUTH OF RAYLEIGH
11/02	20:45:02.4	21.7S	139.1W	5.2	RSNY	237.07	230.19	
					RSON	221.82	218.24	
					RSSD	213.88	205.69	
11/03	09:30:11.0	42.7N	108.3W	4.3	RSNY	277.63	275.87	263.04
11/04	13:14:17.2	7.1N	72.9W	5.2	RSNY	177.34	190.28	80.48
					RSON	151.22	135.13	87.89
					RSSD	134.41	31.23	137.25
11/05	05:57:56.6	14.2N	91.6W	4.4	RSNY	210.91	203.26	167.68
					RSON	176.59	186.64	150.68
					RSSD	156.62	214.11	286.59
11/08	06:33:57.4	26.1S	73.1W	5.0	RSNY	178.64	148.69	160.98
					RSON	161.23	140.58	128.09
					RSSD	151.55	119.80	141.36
11/08	13:01:55.5	52.4N	171.2W	5.3	RSNY	315.39	314.29	3.81
					RSON	303.73	320.26	316.33
					RSSD	305.69	78.26	276.76
11/08	13:57:52.5	23.9S	64.6W	4.5	RSNY	170.28	151.37	265.36
					RSON	153.07	151.07	129.74
					RSSD	143.42	111.91	251.72
11/08	14:17:47.2	31.3S	68.0W	5.6	RSNY	174.25	151.07	
					RSON	158.17	136.29	
					RSSD	149.52	124.01	
11/10	08:40:28.7	61.7N	27.3W	4.6	RSON	46.76	64.87	38.05
					RSSD	39.67	86.31	37.05
11/14	10:55:30.0	55.8N	160.4E	4.7	RSON	319.88	309.28	
					RSSD	318.47	290.37	
11/16	08:56:04.8	21.3S	66.7W	4.8	RSNY	172.03	154.63	
					RSON	154.15	155.45	
					RSSD	143.96	118.03	

Table I. P and Rayleigh Wave Data for Selected Teleseismic Events -- (Continued)

DATE (1984)	ORIGIN TIME	LAT (deg)	LONG (deg)	MAG (m_b)	STATION	BACKAZIMUTH (CALC.)	MEASURED BACKAZIMUTH OF P	MEASURED BACKAZIMUTH OF RAYLEIGH
11/17	09:03:20.8	63.4N	152.5W	4.6	RSNY	322.55	307.65	172.28
					RSON	315.11	324.47	145.83
					RSSD	322.40	309.45	
11/18	23:00:01.7	8.8N	73.3W	5.0	RSNY	177.92	153.61	61.01
					RSON	151.01	139.48	69.43
					RSSD	133.63	124.25	316.62
11/19	00:44:27.2	58.8N	157.0W	4.8	RSNY	317.58	318.12	61.81
					RSON	307.83	311.97	22.64
					RSSD	313.82	87.94	285.70
11/19	04:10:38.3	51.4N	179.0E	5.6	RSNY	318.70	338.40	355.94
					RSON	307.05	295.85	252.04
					RSSD	307.30	304.39	250.115
11/19	12:06:29.1	51.8N	175.1W	5.6	RSNY	316.46	322.79	305.68
					RSON	304.76	307.25	24.96
					RSSD	305.97	107.81	285.57
11/22	13:52:53.9	68.4N	140.8E	5.1	RSNY	346.30	330.05	59.08
					RSON	338.29	355.98	298.75
					RSSD	336.77	312.47	61.20
11/23	09:45:24.7	38.1N	106.3E	4.8	RSNY	359.34		38.38
					RSON	344.38	15.29	56.48
					RSSD	336.54	282.04	312.82
11/23	18:08:26.2	37.6N	118.3W	5.3	RSNY	273.49		350.02
					RSON	242.24	233.37	327.72
11/23	18:40:12.3	8.1S	76.0W	5.9	RSNY	181.83	162.68	266.42
					RSON	159.85	159.86	328.16
					RSSD	146.74	128.26	339.96
11/24	05:50:07.8	56.2N	96.9E	4.4	RSON	353.84	18.77	357.63
					RSSD	348.28	100.11	303.07
11/25	01:22:53.2	55.7N	161.5E	4.7	RSON	319.28	307.13	0.34
					RSSD	317.98	293.02	276.85

Table I. *P* and Rayleigh Wave Data for Selected Teleseismic Events -- (Continued)

DATE (1984)	ORIGIN TIME	LAT. (deg.)	LONG. (deg.)	MAG. (m_b)	STATION	BACKAZIMUTH (CALC.)	MEASURED BACKAZIMUTH OF *P*	OF RAYLEIGH
11/26	01:12:31.4	20.4N	116.3W	5.0	RSNY	248.82	237.98	241.13
					RSON	218.60	222.68	214.70
					RSSD	207.20	102.07	121.51
11/26	16:21:56.7	38.3N	118.5W	4.7	RSNY	274.77		276.95
					RSON	243.89	235.85	234.28
11/28	11:22:10.3	24.0S	66.9W	4.9	RSNY	172.53	152.24	258.08
					RSON	155.14	162.45	315.15
					RSSD	145.38	121.45	345.99
11/29	19:12:18.4	35.4S	71.1W	5.6	RSNY	177.16	154.11	142.42
					RSON	161.74	160.00	191.53
					RSSD	153.58	100.16	134.70
12/02	03:19:06.0	50.1N	79.2E	5.2	RSNY	16.63	4.43	299.02
					RSON	4.63	10.56	8.22
					RSSD	85.74	35.58	316.92
12/02	06:09:40.4	20.1N	116.0W	5.9	RSNY	248.20	244.84	242.29
					RSON	217.94	226.90	213.14
					RSSD	206.36	188.69	205.46
12/02	08:35:41.7	63.4N	150.3W	4.9	RSNY	322.22	146.59	
					RSON	314.96	67.76	
					RSSD	322.81	107.73	
12/03	04:08:26.7	44.2N	148.2E	6.5	RSNY	330.68	317.37	
					RSON	317.98	334.99	301.47
					RSSD	313.71	80.00	301.86
12/04	07:43:09.0	22.7N	143.2E	5.9	RSNY	324.34		306.36
					RSON	309.38	325.85	333.40
					RSSD	301.71	125.71	294.24
12/05	04:26:58.8	38.1S	73.9W	5.1	RSNY	179.50	144.93	87.97
					RSON	164.54	194.20	195.09
					RSSD	156.69	126.18	129.91
12/06	17:28:59.1	21.8S	139.1W	5.3	RSNY	237.01	225.22	
					RSON	221.77	228.14	
					RSSD	213.84	205.03	

Table I. *P* and Rayleigh Wave Data for Selected Teleseismic Events -- (Continued)

DATE (1984)	ORIGIN TIME	LAT. (deg.)	LONG. (deg.)	MAG. (m_b)	STATION	BACKAZIMUTH (CALC.)	MEASURED BACKAZIMUTH OF *P*	MEASURED BACKAZIMUTH OF RAYLEIGH
12/07	10:19:11.0	1.2S	14.8W	5.6	RSNY	113.11	91.83	97.82
					RSON	99.40	92.51	92.08
					RSSD	91.39	109.47	350.40
12/09	08:03:19.9	32.3N	116.5W	3.6	RSON	230.81	228.74	
12/09	14:45:31.9	7.0N	73.0W	4.4	RSNY	177.51	150.96	
					RSON	151.39	141.72	
					RSSD	134.60	36.91	
12/09	19:39:59.8	37.3N	116.4W	5.4	RSNY	271.76	272.19	262.73
					RSON	238.70	226.72	240.89
12/09	22:41:11.9	14.4N	92.4W	4.3	RSNY	212.34	181.66	212.39
					RSON	177.88	162.76	
					RSSD	157.93	122.17	324.64
12/10	03:32:00.9	20.4N	115.9W	4.9	RSNY	248.42	256.10	239.66
					RSON	218.01	215.53	213.37
					RSSD	206.39	179.83	202.78
12/10	10:21:58.1	14.7S	75.5W	5.4	RSNY	181.09	159.23	161.58
					RSON	160.91	131.67	166.88
					RSSD	149.15	124.25	176.29
12/11	23:22:23.0	22.5S	68.8W	6.0	RSNY	174.26	148.92	147.54
					RSON	156.43	81.14	151.87
					RSSD	146.33	117.89	131.87
12/13	08:10:07.3	16.0N	97.0W	4.8	RSNY	220.73	205.41	145.08
					RSON	185.54	172.72	173.23
					RSSD	165.83	334.56	87.25
12/14	00:34:01.3	32.9S	68.0W	4.5	RSNY	174.39	138.15	
					RSON	158.61	140.39	
					RSSD	150.20	127.50	
12/14	07:58:48.6	16.7S	72.3W	4.0	RSNY	177.56	148.11	
					RSON	158.18	154.65	166.60
					RSSD	146.92	311.59	130.22
12/14	12:40:45.2	50.8N	129.5W	3.9	RSNY	299.91		204.59
					RSON	283.91	280.73	198.83

4.2. NOTE ON m_b BIAS AT SELECTED SOVIET SEISMIC STATIONS

4.2.1. Introduction

In a previous report (Ryall, 1986), magnitude m_b was determined for five earthquakes on 25 and 27 May 1980, from recordings at eight Soviet seismic stations on a profile from eastern Kazakh to eastern Siberia. The magnitude residual for a station (SEM) at Semipalatinsk, about 100 km from the Soviet eastern Kazakh test range, was found to be about +0.10 relative to network-averaged m_b values listed in the *Bulletin of the International Seismological Centre*. This value is similar to m_b residuals of +0.06 reported by Priestley *et al.* (1987) for digital stations being operated in east Kazakh under the auspices of the Soviet Academy of Sciences and the Natural Resources Defense Council, and +0.07 inferred from work of Vanek *et al.* (1978, 1980) for the SEM station.

My previous analysis also included an estimate of the m_b bias for a temporary station (OB2NV) on the Climax granitic stock, site of the 1966 Piledriver explosion, at the Nevada Test Site. This analysis, based on amplitudes and periods listed by Der *et al.* (1978), gave an m_b bias of -0.10 relative to magnitudes listed in the ISC *Bulletin*, and comparison of this value with that for SEM gave a total bias of +0.20 m_b for the SEM station relative to the NTS granite site. However, Priestley *et al.* (1987) reported a bias of -0.28 m_b for the OB2NV station, leading to a total Kazakh-NTS bias of 0.34 m_b.

In order to check on the possibility that my original value of the OB2NV-ISC bias was miscalculated, the data listed by Der *et al.* were re-examined by T.W. McElfresh of Teledyne-Geotech, and both McElfresh and I checked the various computer tables and algorithms used to computer m_b values for the 1978 study. The OB2NV-ISC m_b bias did require a change, but it was not in a direction that would give better agreement with Priestley *et al.* The results of this re-analysis are described in the following section.

4.2.2. Analysis and Results

In checking the procedures used in the study by Der *et al.*, McElfresh found that the amplitudes listed in that report were not corrected for instrument response, only for a calibration factor corresponding to the response at 1 Hz. However, we both checked the various computer tables (Gutenberg-Richter Q values and instrument response curves) and confirmed that the m_b values in the Der *et al.* report were correctly determined.

The OB2NV bias relative to the ISC *Bulletin* was redetermined in two ways, both based on an expanded table of magnitudes listed by Der *et al.* (1980):

- For 14 events with m_b 5.8 or greater the OB2-ISC bias was -0.015 $\pm$0.45. The reason for restricting the sample to this magnitude range was that the events I measured on the SEM recordings had m_b 5.8-6.3, and 150-kt shots have m_b 5.8 or greater.

- For 128 events for which the ISC m_b was determined by averaging 25 or more estimates from individual stations the bias was -0.048 ±0.39. The reason for restricting this sample to events with a large number of magnitude measurements was to avoid the effect of missing data on ISC m_b values defined by only a few measurements. As a result of this restriction, about half the tabulated values in the 1980 report were not used in this analysis.

4.2.3. Discussion

The revised values of -0.02 to -0.05 for the m_b bias between OB2NV and the network-averaged ISC magnitudes reduce my earlier estimate of the propagation bias between NTS and eastern Kazakh. The new value is the original bias of +0.10 for SEM, minus the value for NTS, giving an SEM-OB2NV m_b bias of 0.12-0.15. This is considerably less than the Kazakh-NTS bias (0.34) cited by Priestley *et al.* This is curious, since their value for the Kazakh stations is almost the same as my value for the SEM station, and we both used the data tabulated by Der *et al.* to calculate the bias for OB2NV.

Several caveats should be noted in regard to this analysis. First, the SEM-OB2NV bias of 0.12-0.15 represents only the effect due to attenuation in the crust and upper mantle beneath the respective seismic stations. It does not reflect possible differences in coupling of explosion energy into seismic waves at the two test sites, or focusing and defocusing of seismic waves due to structural complexity in the immediate vicinity of a given explosion. Second, m_b values for the SEM station may contain a systematic offset because the response of the Soviet SKM seismic system differed from that used in the investigation by Der *et al.* If this effect were large, however, one would not expect agreement between the SEM-ISC station bias of my study and the Kazakh-NEIS value found by Priestley *et al.* using data from a system similar to the one used by Der *et al.* Third, as pointed out by R.R. Blandford (written communication), the eastern Kazakh explosions tend to have relatively greater high-frequency content than the earthquakes used to compute the bias for both SEM and OB2NV and this possible effect is not taken into account in the present analysis. Blandford suggests that restricting the analysis to small earthquakes might be a better test of the high-frequency propagation differences between the two sites, but such events tend to have network-averaged m_b values that are biased high because of incomplete detection.

Finally, we note that Der *et al.* (1982) found m_b bias values of 0.12±0.12 and 0.16±0.07 between the OB2NV station and eastern North American stations at Houlton, Maine (HNME), and Red Lake, Ontario (RKON), respectively. The Houlton site was selected as a geologic analog to the eastern Kazakh test range, which is characterized by sedimentary deposits of principally Carboniferous age, with moderate folding, faulting and intrusion. The Houlton area has thick eugeosynclinal deposits of Silurian-Ordovician age overlying a Precambrian Grenville basement (Dainty *et al.*, 1966). The Red Lake site is on the Canadian shield, and is not considered to be geologically analogous to the eastern Kazakh region. It is interesting that, for signal frequencies close to 1.0 Hz, the m_b bias range determined for station SEM relative to OB2NV is exactly the range of bias values for HNME and RKON relative to OB2NV. Altogether, Der *et al.* (1980) found a range of -0.06 to +0.02 m_b for three Nevada sites (SZNV, OB3NV, GQNV) and -0.05 to +0.16 for three eastern U.S. sites (IFME,

HNME, RKON) -- all sites on granite or other [illegible] to OB2NV. The largest difference between the [illegible] 0.21 m_b (RKON-SZNV), and the difference between [illegible] (+0.08) and the mean Nevada value [illegible] was [illegible] of 0.34 m_b cited by Priestley *et al* as the [illegible] Nevada Test Site is almost twice as large as [illegible] sites in the eastern U.S. and Nevada.

REFERENCES

Dainty, A. M., Keen, C. E., Keen, M. [illegible] cal Evidence on Crust and [illegible] Canada, *Am. Geophys. Un. Geophys.* [illegible]

Der, Z. A., Dawkins, M. S., McElfresh, T. W. [illegible] 1978, "A Comparison of Teleseismic *P* Wave [illegible] Selected Basin and Range Sites and [illegible] Volume 2," *Teledyne-Geotech Rept.*, SDAC-TR-[illegible]

Der, Z. A., McElfresh, T. W., Mrazek, C. E., Kazarc [illegible] and Sproules, H. M., 1980, "Results of the NTS Experiment [illegible] *Geotech Rept.*, SDAC-TR-78-4, 221 pp.

Der, Z. A., McElfresh, T. W., and Anne O'Donnell, [illegible] Regional Variations and Frequency Dependence of Attenuation [illegible] tle Under the United States in the 0.5-4 Hz Band," *Geophys.* [illegible] 100.

Priestley, K. F., Chavez, D. E., and Brune, J. N. (1987), "A Direct [illegible] Between Eastern Kazakh and Nevada," *EOS, Trans. Am. Geophys.* [illegible] 362.

Ryall, A. S., 1986, "Preliminary Study of m_b Bias at Selected Soviet Seismic [illegible] *Center for Seismic Studies, Rept.*, C86-04, 35 pp.

Vanek, J. and 32 other authors, 1978, "Station Corrections for Longitudinal Waves in the Unified Magnitude System of the Eurasian Continent," *Akad. Nauk SSSR, Izv. Earth Phys.*, 14; *Am. Geophys. Un.*, 169-178.

Vanek, J., Kondorskaya, N. V., Federova, I. V., and Khristoskov, L., 1980, Optimization of Amplitude Curves for Longitudinal Seismic Waves for Purposes of Development of a Uniform Magnitude System for Seismic Observations on the Eurasian Continent," *Doklady Akad. Nauk SSSR*, 250, 834-838, transl. by Scripta Publ. Co.

4.3 STATUS OF NRDC AND OTHER WAVEFORM DATABASES

4.3.1 Introduction

[illegible] facilitate the work of other [illegible] research program, with the [illegible] aseis. The Center [illegible] databases. Some of these [illegible] the contents are fixed, [illegible] cases as new data of the

4.3.2 Status of Primary Databases

[illegible] through the *INGRES* rela- [illegible] 58 Mbytes of disk [illegible] status of the primary data- [illegible] databases that the term [illegible] a particular source, [illegible] another agency. [illegible] waveform segments for GDSN, WAKE, SAFRICA, HDWWSSN, NORSAR, ASPA, NRDC, IRSM, RSTNATLN [illegible] continuous and

Table 1. Status of Primary Center Databases

	[illegible]	No. Types	Mbytes (disk)
Parameter Data			
	[illegible]	0	53.044
	[illegible]	0	19.760
	[illegible]	0	173.500
	[illegible]	0	21.524
Waveforms complete			
[illegible]	[illegible]	1083	250.282
[illegible]	[illegible]	3397	172.592
	[illegible]	0	71.228
WWSSN	Sep. 5, 1985 to current	138	4.676
[illegible]	Mar. 14, 1985 to current	1	0.712
NRDC Phase 1	Jul. 15, 1986 to Nov. 15, 1986	0	0
NRDC Phase 2	Mar. 19, 1987 to Apr. 25, 1987	7	0.580
HDWWSSN	Sep. 13, 1965 to Dec. 27, 1981	4	1.752

AD-A185 959 TECHNICAL REPORT FOR THE PERIOD 1 APRIL-30 JUN 1987(U) 2/2
SCIENCE APPLICATIONS INTERNATIONAL CORP ARLINGTON VA
CENTER F.. R BAUMSTARK ET AL. AUG 87 SAIC-87/1131
UNCLASSIFIED MDA903-84-C-0021 F/G 8/11 NL

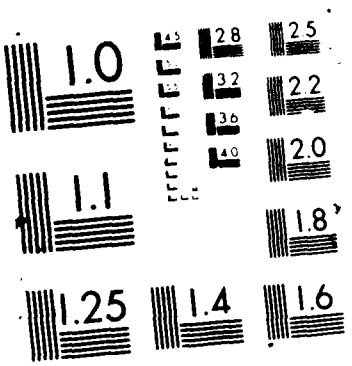
1.0
1.1
1.25
1.4
1.6
1.8
2.0
2.2
2.5
2.8
3.2
3.6
4.0

Table I. Status of Primary Center Databases - (Continued)

Database	Coverage	No. Tapes	Mbytes (disk)
Waveforms-incomplete			
NORESS	Oct. 25, 1984 to current	380	28.528
NORESSHF	Dec. 1, 1985 to current	183	1.360
NORSAR	Nov. 6, 1976 to current	100	18.920
ASPA	Dec. 10, 1986 to Apr. 16, 1987	4	0.692
RSTNATTN	Jan. 17, 1983 to Oct. 23, 1984	1	0.768
LRSM	Feb. 2, 1962 to Sep. 9, 1966	1	0.620

4.3.3. The NRDC Database

The Center is now receiving waveform data from three seismic stations being operated in eastern Kazakh, U.S.S.R., under a cooperative agreement between the Soviet Academy of Sciences and the Natural Resources Defense Council. The first seismic station installed under this agreement began operation at Karkaralinsk (KKL) on 15 July 1986, and the others were set up at Bayanaul (BAY) and Karasu (KSU) during the summer and fall of 1986. The sites are within the Kazakh fold system, south of the west Siberian platform, and according to Berger *et al.* (1987) are all situated "in granite massifs that rise several hundred meters above the surrounding steppe."

The Kazakh experiment is being conducted in two phases. In the first phase, from July through December 1986, the stations were equipped with Geotech S-13 short-period and Kinemetrics S-1 intermediate-period seismometers, and Terra Tech model 302 digital event recorders, sampling at 100 Hz. The tape cassettes produced by these recorders were copied onto IBM/PC floppy disks and the latter were transported by members of the field team to the University of Nevada-Reno, where the data were copied to 9-track tapes and sent to the Center. The first tapes were received from the Nevada group in April, 1987, and the Center now has the complete Phase I data set. However, the data format is complex, with data start times not corresponding to the beginning of one-second data blocks and headers multiplexed with the digitized waveforms, and some of the signals appear to be affected by digitization problems; in addition, channels corresponding to different instrument components sometimes all have the same signal. An effort amounting to several man-months has been expended by the Center software and database staff in attempting to identify and correct the cause of the data problems and obtain accurate calibration information from the University of Nevada, without complete success. As a result, higher priority is now being directed to the Phase II data.

The Phase II data, received from the University of California-San Diego, is better organized and documented than the Phase I data, and the processing and preliminary analysis of this data are proceeding relatively smoothly. The stations are now equipped with Teledyne-Geotech S-750 broadband seismometers emplaced in boreholes, with high- and low-gain output signals sampled at 250 Hz, plus a surface vault containing S-13 short-period and S-1 intermediate-band seismometers, also recording at two gain levels. According to Eissler *et al.* (1987), the S-1 seismometers may eventually be replaced with Streckeisen VBB instruments. The

MA-II data acquisition system was fabricated at UCSD by the U.S. team, and utilizes a DEC LSI-11/73 processor. In the course of processing the data, we have identified a number of problems with the Phase II operation. For example, the downhole package appears to be misoriented by 90° at the KKL site, the Z- and EW-channels appear to be swapped at KSU, magnetic declination appears not to have been taken into account in installing the horizontal components, and the uphole instruments at KSU are affected by high noise levels. These problems have been communicated to the San Diego group, and we are currently working with members of that group to correct the problems and construct an accurate set of calibration curves for the instruments.

At the time of this writing, waveforms from one or more of the Kazakh stations have been installed in the Center **nrdcw** database for 169 events. Analysis of these events, by F. Ryall of ENSCO, has so far produced **arrival** files for 35 of the events. The station locations, together with channel designations used by the Center and the corresponding instruments, are listed in Table II, below. Table III is a list of the events for which we have data so far. Locations of these events were either taken from the NEIS Preliminary Determination of Epicenters listings, or estimated by Center and ENSCO analysts. In the latter case, locations were determined using the Center's automatic association and epicenter determination program, or estimated from distance and azimuth calculations based on measurements of regional seismic phases for one or two stations. For unassociated waveform segments the table gives a dummy location -- latitude 90.00°, longitude 0.00°. In the data analyzed to date, there is little overlap in the coverage provided by the different stations. Events for the May 15-18 period have data for both the KKL and BAY stations, but other events in the list have data only for a single station. For further information on this database the reader should consult the database documentation on the *hugo* computer (file **/usr/css/tables/css_dbs/.files/../nrdcw**).

Table II. Information on Phase II Data Channels

Station	Channel	Lat. N	Long. E	Elev. m	Inst. Type	Gain
Karkaralinsk	NRKKA	49.33	75.38	934	S-750	High
Karkaralinsk	NRKKF	49.33	75.38	934	S-750	Low
Karkaralinsk	NRKKB	49.33	75.38	1000	GS-13	High
Karkaralinsk	NRKKC	49.33	75.38	1000	GS-13	Low
Karkaralinsk	NRKKD	49.33	75.38	1000	S-1	High
Karkaralinsk	NRKKE	49.33	75.38	1000	S-1	Low
Bayonaul	NRBAA	50.82	75.55	501	S-750	High
Bayonaul	NRBAF	50.82	75.55	501	S-750	Low
Bayonaul	NRBAB	50.82	75.55	600	GS-13	High
Bayonaul	NRBAC	50.82	75.55	600	GS-13	Low
Bayonaul	NRBAE	50.82	75.55	600	S-1	Low
Karasu	NRKSA	49.98	81.10	320	S-750	High
Karasu	NRKSB	49.98	81.10	420	GS-13	High
Karasu	NRKSC	49.98	81.10	420	GS-13	Low
Karasu	NRKSD	49.98	81.10	420	S-1	High
Karasu	NRKSE	49.98	81.10	420	S-1	Low

Table III. Events with NRDC Data

Date	Time, GMT	Lat. Deg. N	Long. Deg. E	m_b
Mar. 19, 1987	14:32:19.0	23.67	64.66	5.1
Mar. 20, 1987	08:07:41.2	49.50	72.90	-1.0
Mar. 20, 1987	09:00:30.5	48.40	73.00	-1.0
Mar. 20, 1987	10:51:40.2	49.90	75.00	-1.0
Mar. 20, 1987	11:06:38.2	49.50	75.80	-1.0
Mar. 20, 1987	13:03:02.5	7.42	123.62	4.3
Mar. 21, 1987	10:10:08.1	49.50	75.80	-1.0
Mar. 21, 1987	10:41:36.2	52.01	-177.44	6.0
Mar. 21, 1987	12:48:24.1	49.60	73.40	-1.0
Mar. 21, 1987	14:46:37.9	36.53	70.96	4.8
Mar. 21, 1987	17:52:15.0	90.00	0.00	-1.0
Mar. 24, 1987	09:27:55.0	51.33	75.38	-1.0
Mar. 24, 1987	12:49:46.4	37.37	137.80	5.7
Mar. 24, 1987	21:38:11.5	22.20	143.76	4.9
Apr. 09, 1987	00:48:54.9	1.20	128.46	5.4
Apr. 09, 1987	07:25:35.9	35.37	86.92	4.9
Apr. 09, 1987	07:57:16.3	90.00	0.00	-1.0
Apr. 09, 1987	09:27:54.7	51.40	75.50	-1.0
Apr. 09, 1987	20:01:17.6	35.59	80.47	4.9
Apr. 10, 1987	06:43:23.7	37.13	57.68	4.9
Apr. 10, 1987	09:35:07.7	51.30	75.30	-1.0
Apr. 10, 1987	09:52:30.9	49.50	75.76	-1.0
Apr. 10, 1987	10:21:28.8	90.00	0.00	-1.0
Apr. 10, 1987	10:59:41.4	36.04	139.57	5.0
Apr. 11, 1987	18:13:25.6	23.98	122.08	5.6
Apr. 11, 1987	19:02:06.2	1.03	128.44	5.2
Apr. 11, 1987	23:50:30.2	31.52	56.01	5.0
Apr. 12, 1987	02:47:18.3	35.43	23.42	5.1
Apr. 12, 1987	19:29:56.2	4.93	94.15	4.5
Apr. 13, 1987	06:47:56.3	47.60	76.95	-1.0
Apr. 13, 1987	08:06:39.9	-37.44	78.19	5.3
Apr. 13, 1987	08:24:48.8	90.00	0.00	-1.0
Apr. 13, 1987	10:14:04.3	50.50	72.85	-1.0
Apr. 13, 1987	11:23:19.3	90.00	0.00	-1.0
Apr. 21, 1987	14:58:19.0	36.42	71.54	4.7
Apr. 21, 1987	15:28:43.6	-22.79	170.17	6.0
Apr. 21, 1987	21:18:10.8	90.00	0.00	-1.0
Apr. 21, 1987	23:57:23.2	39.44	64.88	4.3
Apr. 22, 1987	07:46:34.8	90.00	0.00	-1.0
Apr. 22, 1987	20:13:25.2	37.08	141.39	6.1
Apr. 23, 1987	09:16:44.8	51.30	75.30	-1.0
Apr. 23, 1987	09:17:02.3	90.00	0.00	-1.0
Apr. 23, 1987	09:40:00.1	50.60	73.00	-1.0
Apr. 23, 1987	09:51:51.8	49.55	75.75	-1.0
Apr. 23, 1987	09:58:08.9	49.40	72.70	-1.0

Table III. Events with NRDC Data - (Continued)

Date	Time, GMT	Lat. Deg. N	Long. Deg. E	m_b
Apr. 23, 1987	11:12:27.3	90.00	0.00	-1.0
Apr. 23, 1987	12:10:30.3	90.00	0.00	-1.0
Apr. 23, 1987	16:39:24.1	5.87	125.87	5.4
Apr. 24, 1987	04:32:10.8	37.28	141.31	4.5
Apr. 24, 1987	05:48:32.1	49.83	75.38	-1.0
Apr. 24, 1987	09:23:34.4	50.79	73.04	-1.0
Apr. 24, 1987	09:24:23.0	50.70	73.50	-1.0
Apr. 24, 1987	09:34:01.5	47.70	78.00	-1.0
Apr. 24, 1987	09:39:02.8	90.00	0.00	-1.0
Apr. 24, 1987	10:16:27.8	90.00	0.00	-1.0
Apr. 24, 1987	10:47:18.8	90.00	0.00	-1.0
Apr. 24, 1987	10:59:20.8	90.00	0.00	-1.0
Apr. 24, 1987	12:41:03.5	-5.76	127.60	5.5
Apr. 24, 1987	22:25:29.9	36.57	70.51	4.4
Apr. 25, 1987	06:03:59.9	50.80	75.50	-1.0
Apr. 25, 1987	07:23:56.3	90.00	0.00	-1.0
Apr. 25, 1987	08:08:59.3	6.88	126.09	5.3
Apr. 25, 1987	08:25:11.9	49.50	75.80	-1.0
Apr. 25, 1987	12:16:49.3	15.90	120.33	5.4
Apr. 25, 1987	12:16:54.3	16.02	120.46	6.3
Apr. 25, 1987	19:22:10.7	2.26	99.02	5.9
Apr. 26, 1987	20:02:07.8	31.85	139.53	5.2
Apr. 27, 1987	04:38:37.5	-3.03	101.59	5.3
Apr. 27, 1987	05:21:06.2	49.38	75.65	-1.0
Apr. 27, 1987	05:23:38.7	27.86	139.74	4.7
Apr. 27, 1987	06:20:46.5	-6.03	130.51	5.1
Apr. 27, 1987	07:08:38.3	90.00	0.00	-1.0
Apr. 27, 1987	09:02:36.3	90.00	0.00	-1.0
Apr. 27, 1987	09:27:55.0	50.50	73.70	-1.0
Apr. 27, 1987	09:30:43.5	51.00	73.40	-1.0
Apr. 27, 1987	09:47:24.1	49.50	75.30	-1.0
Apr. 27, 1987	10:41:17.8	90.00	0.00	-1.0
Apr. 27, 1987	11:24:53.8	90.00	0.00	-1.0
Apr. 27, 1987	11:33:52.0	11.59	-87.19	4.7
Apr. 27, 1987	11:45:58.3	50.00	72.95	-1.0
Apr. 27, 1987	12:13:51.0	12.84	123.63	4.3
Apr. 27, 1987	16:58:57.8	37.72	142.66	5.1
Apr. 28, 1987	00:26:18.3	90.00	0.00	-1.0
Apr. 28, 1987	07:23:56.3	90.00	0.00	-1.0
Apr. 28, 1987	07:44:26.9	51.10	74.00	-1.0
Apr. 28, 1987	08:47:34.5	49.50	75.70	-1.0
Apr. 28, 1987	09:01:05.0	50.10	61.00	-1.0
Apr. 28, 1987	12:34:43.8	90.00	0.00	-1.0
Apr. 28, 1987	15:32:31.9	2.02	99.06	5.7
Apr. 28, 1987	22:44:33.6	2.01	98.94	5.0

Table III. Events with NRDC Data - (Continued)

Date	Time, GMT	Lat. Deg. N	Long. Deg. E	m_b
Apr. 29, 1987	01:45:26.0	27.40	56.07	5.9
Apr. 29, 1987	05:34:14.8	90.00	0.00	-1.0
Apr. 29, 1987	06:03:30.3	90.00	0.00	-1.0
Apr. 29, 1987	07:20:45.3	90.00	0.00	-1.0
Apr. 29, 1987	07:44:08.8	90.00	0.00	-1.0
Apr. 29, 1987	07:47:34.8	90.00	0.00	-1.0
Apr. 29, 1987	11:02:07.8	90.00	0.00	-1.0
Apr. 29, 1987	11:43:17.3	90.00	0.00	-1.0
Apr. 29, 1987	14:27:36.6	-18.93	-177.86	5.9
May 13, 1987	07:31:57.9	51.63	74.62	-1.0
May 13, 1987	07:51:29.7	90.00	0.00	-1.0
May 13, 1987	07:59:03.2	90.00	0.00	-1.0
May 13, 1987	09:03:19.0	51.60	74.84	-1.0
May 13, 1987	09:09:15.1	51.66	75.05	-1.0
May 13, 1987	09:10:19.7	90.00	0.00	-1.0
May 13, 1987	09:13:23.7	90.00	0.00	-1.0
May 13, 1987	09:25:54.1	51.56	74.75	-1.0
May 13, 1987	09:29:56.5	50.13	74.65	-1.0
May 13, 1987	09:33:23.6	50.36	73.64	-1.0
May 13, 1987	09:42:36.5	50.18	72.92	-1.0
May 13, 1987	09:56:23.2	90.00	0.00	-1.0
May 13, 1987	10:20:41.9	51.67	74.71	-1.0
May 13, 1987	12:36:07.2	90.00	0.00	-1.0
May 13, 1987	13:17:33.7	90.00	0.00	-1.0
May 13, 1987	17:52:26.2	90.00	0.00	-1.0
May 13, 1987	23:40:51.5	4.47	94.99	3.7
May 14, 1987	00:21:54.7	-6.15	147.91	4.6
May 14, 1987	00:24:56.7	34.89	140.73	4.7
May 14, 1987	02:50:25.7	90.00	0.00	-1.0
May 14, 1987	08:21:17.2	90.00	0.00	-1.0
May 14, 1987	08:43:12.7	90.00	0.00	-1.0
May 14, 1987	08:51:30.6	51.54	74.70	-1.0
May 14, 1987	09:22:21.4	49.64	73.43	-1.0
May 14, 1987	09:32:15.2	51.64	74.60	-1.0
May 14, 1987	09:36:13.1	49.91	74.34	-1.0
May 14, 1987	09:47:04.7	90.00	0.00	-1.0
May 14, 1987	09:57:58.7	90.00	0.00	-1.0
May 14, 1987	10:43:27.7	90.00	0.00	-1.0
May 14, 1987	12:02:19.6	2.83	129.06	5.7
May 14, 1987	15:31:03.6	22.48	121.40	5.1
May 14, 1987	15:57:26.9	-33.75	-72.18	5.3
May 14, 1987	16:04:26.5	-5.62	-81.39	5.6
May 14, 1987	17:52:26.2	90.00	0.00	-1.0
May 14, 1987	21:11:38.0	13.71	120.73	4.4

Table III. Events with NRDC Data - (Continued)

Date	Time, GMT	Lat. Deg. N	Long. Deg. E	m_b
May 14, 1987	22:24:00.1	40.06	40.30	4.8
May 15, 1987	06:46:58.6	51.22	73.02	-1.0
May 15, 1987	08:24:00.2	90.00	0.00	-1.0
May 15, 1987	08:44:04.1	56.40	-153.11	4.7/4.9
May 15, 1987	08:44:04.1	56.40	-153.11	4.7/4.9
May 15, 1987	09:08:34.0	51.70	75.00	-1.0
May 15, 1987	09:13:40.7	51.64	74.96	-1.0
May 15, 1987	09:33:13.5	51.62	74.90	-1.0
May 15, 1987	09:35:31.2	90.00	0.00	-1.0
May 15, 1987	09:37:06.4	51.60	74.83	-1.0
May 15, 1987	10:06:41.4	51.52	74.66	-1.0
May 15, 1987	10:28:34.0	51.45	74.53	-1.0
May 15, 1987	10:34:59.3	49.10	72.70	-1.0
May 15, 1987	10:53:25.6	46.30	75.50	-1.0
May 15, 1987	11:01:18.8	90.00	0.00	-1.0
May 15, 1987	17:52:14.3	90.00	0.00	-1.0
May 15, 1987	21:34:51.0	-24.77	-70.70	5.2
May 16, 1987	03:34:52.2	-7.46	128.11	5.3
May 16, 1987	05:22:08.7	90.00	0.00	-1.0
May 16, 1987	05:41:15.2	90.00	0.00	-1.0
May 16, 1987	05:43:30.0	51.64	74.98	-1.0
May 16, 1987	07:09:37.5	51.65	75.02	-1.0
May 16, 1987	08:38:15.2	47.80	74.40	-1.0
May 16, 1987	09:25:06.2	27.94	139.51	3.4
May 16, 1987	13:06:09.9	-6.52	105.44	5.1
May 16, 1987	13:26:01.8	90.00	0.00	-1.0
May 16, 1987	17:52:14.3	90.00	0.00	-1.0
May 16, 1987	18:21:16.0	40.39	73.46	4.1
May 17, 1987	05:12:12.0	-13.57	167.16	5.6
May 17, 1987	12:11:08.5	3.00	97.15	5.1
May 17, 1987	13:43:35.1	0.79	122.21	5.3
May 17, 1987	17:52:14.3	90.00	0.00	-1.0
May 17, 1987	18:41:19.8	90.00	0.00	-1.0
May 17, 1987	20:43:08.3	90.00	0.00	-1.0
May 18, 1987	01:53:51.0	25.26	94.18	5.6

Richard R. Baumstark
Alan S. Ryall

REFERENCES

Berger, J. and fifteen other authors, 1987. "A New U.S.-U.S.S.R. Seismological Program," *EOS, Trans. Am. Geophs. Un.*, 68: 105 and 110-111.

Eissler, H., Berger, J., and Vernon, F., 1987. "U.S.-Soviet Cooperative Array in Eastern Kazakhstan: Installation of Phase II Equipment," *EOS, Trans. Am. Geophys. Un.*, 68: 349, [abstract].

END

12-87

DTIC